Coherent Control of Neutron Interferometry

by

Dmitry A. Pushin

Submitted to the Department of Physics
in partial fulfillment of the requirements for the degree of

Doctor of Philosophy

at the

MASSACHUSETTS INSTITUTE OF TECHNOLOGY

October 2006

Author .....
Department of Physics
October 12, 2006

Certified by .....
David G. Cory
Professor
Thesis Supervisor

Certified by .....
Young S. Lee
Professor
Thesis Supervisor

Accepted by .....
Thomas J. Greytak
Professor
Associate Department Head for Education

Coherent Control of Neutron Interferometry

by

Dmitry A. Pushin

Submitted to the Department of Physics
on October 12, 2006, in partial fulfillment of the
requirements for the degree of
Doctor of Philosophy

Abstract

In this thesis, several novel techniques are proposed and demonstrated for measuring the coherent properties of materials and testing aspects of quantum information processing using a single crystal neutron interferometer. In particular we introduce methods for reciprocal space encoding of spatial information systematically in a neutron interferometer. First, a proof of principle experiment is conducted for coherent reciprocal space neutron imaging. This newly proposed technique overcomes the limitation of spacial resolution of current two dimensional neutron detectors. Second, an experiment to measure the vertical coherent length of a neutron interferometer is reported, which extends the previously achieved path separation. Third, we propose a new interferometry geometry that reduces the sensitivity of the neutron interferometer to environmental vibrational disturbances. The method is based on a quantum error compensating algorithm. Finally, a new method that is capable of measuring the autocorrelation function of a sample is proposed. This new technique can extend the capability of traditional neutron scattering experiments. All experiments are conducted at the neutron interferometry facility at the National Institute of Standards and Technology (NIST).

Thesis Supervisor: David G. Cory
Title: Professor

Thesis Supervisor: Young S. Lee
Title: Professor

Acknowledgments

First, I would like to thank my advisor, Professor David Cory, who believed in me, guided me, and supported me during my thesis work. His intuition, work ideas, and detailed knowledge provided me with an invaluable and exciting experience. Also, his ability to attract talented and interesting people to his group created a unique, inspiring, and joyful work environment.

I also wish to thank Dr. Muhammad Arif, with whom I had the privilege of working. His endless optimism, experimental experience, and the time he invested in me made my graduation possible. His management of such a talented group of scientists made my stay at NIST very interesting and educational.

Next, I would like to extend a special thanks to Professor Young Lee for being my co-advisor and advising me throughout the last three years. My gratitude also goes to Professor Sow-Hsin Chen for sharing his ideas and advice regarding my experiments.

The laboratory environments of both David Cory and Muhammad Arif have been very important as well. During my stay with their groups, I acquired not only knowledge and experience, but more importantly, friends who helped me in many aspects of my life and taught me wisdom. Each of them provided something special and unique. I'd like to give a special acknowledgement to Dr. David Jacobson for spending time on my experiments, educating me on his knowledge of interferometry, sharing his drawings and software programs, and entertaining me with countless stories about everything including Russian jokes. Michael Huber also deserves thanks for being my most reliable hardware for drawing beautiful 3-D graphics, which I have used in my presentations and this thesis. I really appreciate his collaboration with experiments and his friendship. I would also like to thank Dr. Levi for endless discussions and theoretical descriptions of my experiments, as well as for being an awesome roommate and friend. Ceci Lopez I thank as well for being a very good and honest friend. In just a few months, she introduced me to more friends than I would have met in a lifetime. Her character not only aided me socially, but also helped with my thesis and forced me to graduate. I'd also like to thank: Dan Greenbaum and Sekhar

Ramanathan for their help, support, and encouragement in work; Liang Yang and Sergei Dzhosyuk for everything including wide knowledge, interesting puzzles, basketball, and cooking; Pieter Mumm for his encouragement and friendship. Thanks as well to Paola Cappellaro, Anatoly Dementyev, Sergio Valenzuela, Joon Cho, Gabriela Leu, Phillip Sun, Jonathan Hodges, Michael Henry, Sid Sinha, Tatjana Atanasijevic, Martha Neviaser, Jeffrey Nico, Robert Shankle, Alan Thompson, Sam Werner, Dan Hussey, Rob Cooper, Chris O'Shaughnessy, Da Luo, Anna Micherdzinska, Nicolas Boulant, Debra Chen, Timothy Havel, Philip Lawson, Troy Borneman, Jamie Yang, and many others whom I did not mention.

The world is very small, and I found that out by reuniting with one of my oldest childhood friends, Michael Slutsky, with whom I had lost contact for many years. I would never have thought that after so many years I could reconnect with and participate in the life of such a true friend. I'd also like to express a special thanks to Maria Riefstahl. I am indebted to her for helping me and accompanying me through many long years of my studies and life; many of those happy times are thanks to her.

Thanks to MIT as well for providing me with the opportunity to meet such fantastic friends, who have always made sure that I had a broad education not only in physics, but also in life, art and nature exploration: Valeri Ivanov and Roman Barankov. Since writing the acknowledgment is not really a fair process, I can not unfortunately list everybody here. I would like to thank Tatyana Ivanova, Sasha Shirokov, Marat Rvachev, Haiyan Tang, Lexy Huber, Rachel Batista, Vladimir Luzin, Jessica Webster, Dima Abanin, Misha Brodsky, Predrag Nikolic, Peter Volkovitsky, and many others for making my life interesting and enjoyable. Special thanks to Ceci Lopez, Liang Yang, Ben Levi, Monica Bobra, Pieter Mumm, Jessica Webster, Maria Riefstahl, and Matthew Davidson for reading and proofing my thesis.

Of course I would not be at this point without my parents, Alexander Arkadievich and Tamara Petrovna, and my sister Anna. It is your help, love, and motivation which have kept me going. No words can express my gratitude to you. Thank you so much. Спасибо вам, мои дорогие родители и сестра. Also thanks to the rest of my family; you are very important to me.

To my parents.

...Но чем внимательней, твердыня Notre-Dame,
Я изучал твои чудовищные ребра,
Тем чаще думал я: «Из тяжести недоброй
И я когда-нибудь прекрасное создам...»

Осип Мандельштам

...But what is more important, Notre Dame,
Your monstrous ribs I studied from the start
And oft I thought: I too will make fine art
From sturdy heaviness through which I came...

Osip Mandelstam

Contents

List of Figures

List of Tables

Chapter 1

Introduction

1.1 Brief history of Neutron Interferomtry

The wave/particle duality of the neutron was discussed very shortly after Chadwick discovered the neutron in 1932 [1]. In 1936 Elsasser proposed that a neutron's motion is governed by quantum mechanics [2] and in the same year his statement that neutrons would be diffracted by crystalline matter was verified by Halban and Preiswerk [3], and by Mitchell and Powers [4].

The field of neutron interferometry also has a long history. The first neutron interferometer was built by Maier-Leibnitz and Springer in 1962 [5]. It consisted of a single entrance slit and a biprism for beam recombination. Figure 1-1 shows a schematic diagram of this first wave front division neutron interferometer along with a sketch of the setup [5]. Biprism interferometers suffer from small beam separations (on the order of only 60 μm). Measurements with samples placed in only one of the interfering paths are extremely difficult [6].

In 1972, Mezei published a paper [7] where he discussed a new spin-echo system. In this system, the superposition of spin-up and spin-down states provides the basis for Larmor and Ramsey type of interferometry. In such an interferometer, beam splitting is not required. Here the total energy of the neutrons in the spin up and spin down states are the same. Because neutrons with different spin states acquire different potential energies in a magnetic field (Zeeman splitting), their kinetic energies depend

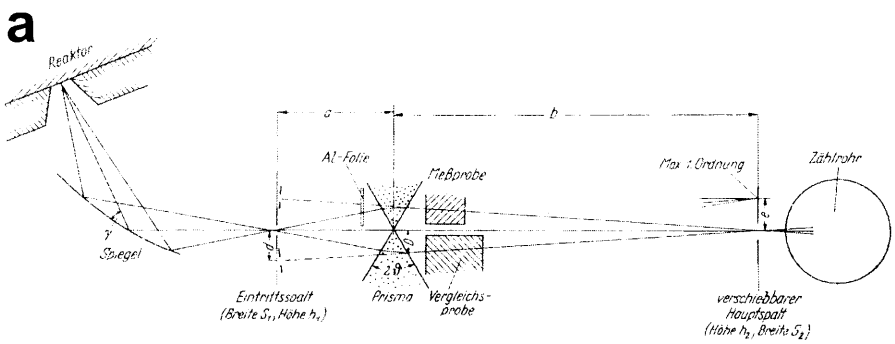

Fig. 1. Schema eines Neutroneninterferometers mit Fresnelschem Biprisma. Größenordnungsmäßig ist: Ablenkwinkel γ am Spiegel 0,1°, Abstand Eintritts-Austrittsspalt $a + b = 10$ m, größter Abstand der Strahlengänge $2D = 0{,}1$ mm. Die $\lambda/2$-Folie dient für das in Abschnitt 4 beschriebene Experiment

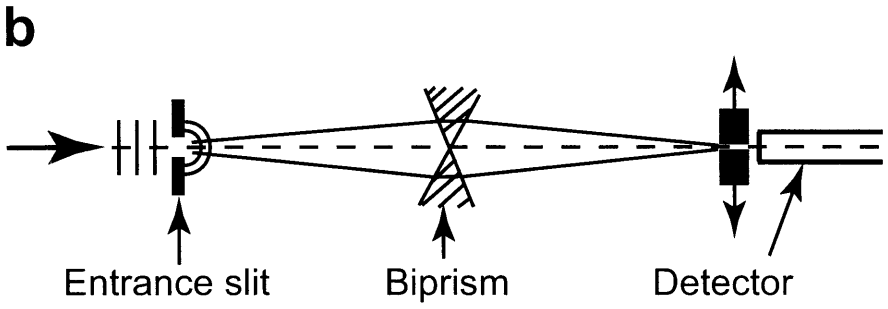

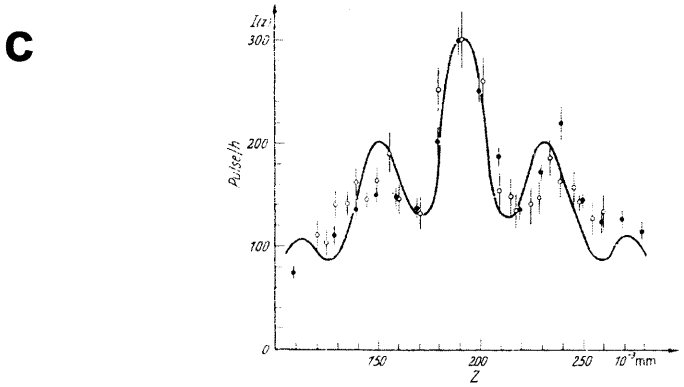

Fig. 9. Interferenzmuster. z Stellung des verschiebbaren Hauptspaltes. $I(z)$ Intensität (der Nulleffekt war bei diesen Messungen etwa 60 Pulse/Std). •, ○ Voneinander unabhängige Meßreihen, erstere ist Mittel aus mehreren Durchgängen. Ausgezogene Kurve: Mit Cornu-Spirale berechnet unter der Annahme monochromatischer Neutronen mit 4,1 Å. Über Hauptspaltbreite gemittelt; endliche Breite des Eintrittsspaltes vernachlässigt. Theoretische Kurve und Meßpunkte der beiden Serien •, ○ untereinander nur im Scheitel der Interferenzfigur aufeinander normiert

Figure 1-1: **a**: Biprism interferometer from Maier-Leibnitz and Springer paper [5]; **b**: Sketch of the biprism interferometer setup. Wave front division interferometer based on single-slit diffraction. (Beam separation of the order of 60 μm); **c**: Intensity of the neutron on the detector due to vertical scan of the S_2 slit.

on their polarization,

$$\frac{\hbar^2 k^2}{2m} = \frac{\hbar^2 k_{\pm}^2}{2m} \pm |\mu| B, \tag{1.1}$$

where μ and m are the magnetic moment and mass of the neutron, k is the wave vector

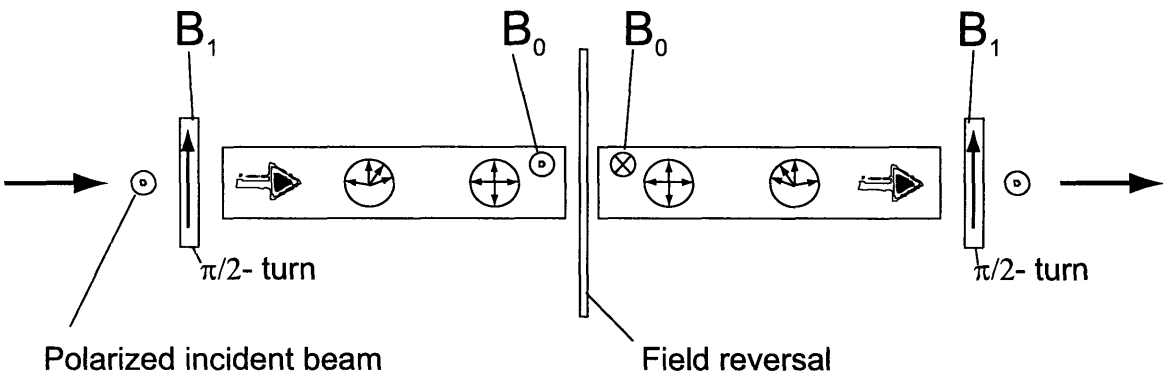

Figure 1-2: Sketch of the Larmor and Ramsey type of neutron interferometer (spin-echo interferometer [7]).

of a neutron in the field free regions, and $k_{\pm}$ are the wave vectors of a neutron in spin states parallel and anti-parallel (up and down) to the magnetic field B respectively. For a neutron traveling a distance L the phase difference $\phi(k, L)$ between the spin-up and spin-down states is

$$\phi(k, L) = 2L\Delta k \cong 2Lm|\mu|B/\hbar^2 k \tag{1.2}$$

and the degree of polarization in the incoming neutron polarization direction behind a field region of length L is

$$P_O(B, L) = \int \tilde{g}(\lambda) \cos(4\pi m|\mu|BL\lambda/\hbar^2) d\lambda, \tag{1.3}$$

where $\tilde{g}(\lambda)d\lambda = g(k)dk = (g_+(k) + g_-(k))dk$ and $g_{\pm}$ are the momentum distribution function for spin up or down states of the neutron. The coherent behavior of a neutron interferometer is clearly shown by echo formation in a spin echo interferometer. If the spread of neutron momenta $g(k)$ is large and the distance between the first $\pi/2$ coil and the field reversal coil is sufficiently long (see figure 1-2), the oscillations of neutron polarization disappear completely (1.3). However, the polarization can be partially recovered using the spin echo technique. The field reversal coil reverses the direction of the neutron spin precession. Thus BL in equation 1.3 denotes the difference between two integrated field values $BL = BL_1 - BL_2$. If the distances

of two precession regions with the same magnetic field are the same $L_1 = L_2$, then $BL_1 = BL_2$ and the initial neutron polarization can be recovered (refocused) after the second $\pi/2$ coil.

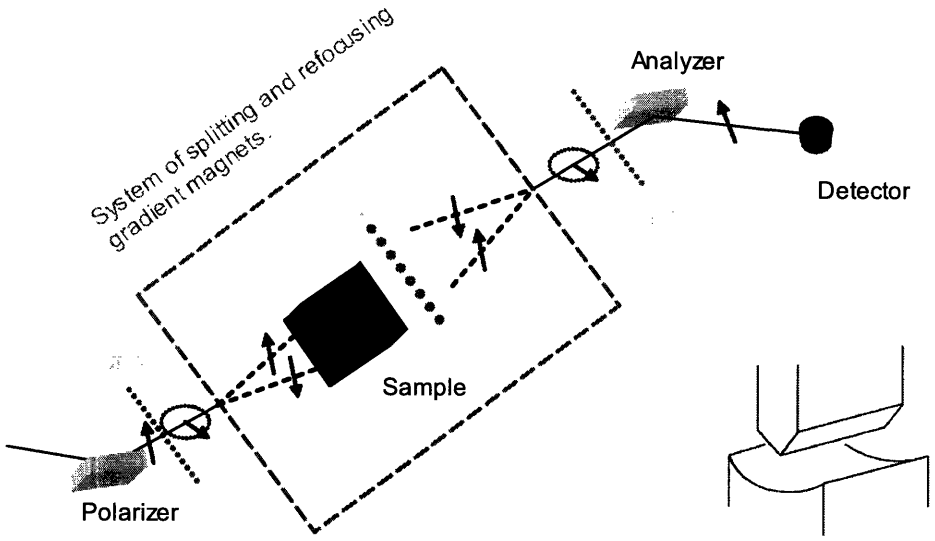

Figure 1-3: A schematic diagram of the Stern-Gerlach type neutron interferometer.

Figure 1-3 reports on another type of spin interferometer with interfering beams separated by strong magnetic field gradients produced by Stern-Gerlach magnets. A polarized beam passes through a $\pi/2$ spin-flipper and splits into spin-up and spin-down components due to the magnetic field gradient. After passing through a phase shifter and a π spin-flipper, the beams are recombined and their interference can be observed. Figure 1-4 shows the explicit neutron wave-functions at different points of the interferometer.

In 1974, the first perfect-crystal interferometer was demonstrated by Rauch, Treimer, Bauspiess and Bonse [8, 9]. Much of their experience with X-ray interferometers [10] was applied to the neutron case. Figure 1-5 shows a sketch of the perfect crystal neutron interferometer Laue-Laue-Laue-type (LLL), where a neutron scatters from each crystal blade in a Laue geometry as shown in figure 1-11. In the Laue geometry the scattered beams are on the opposite side of the blade with respect to an incoming beam and the crystal planes the neutron scatters from are perpendicular to the interferometer blade. Detailed descriptions of this type of interferometer can be found

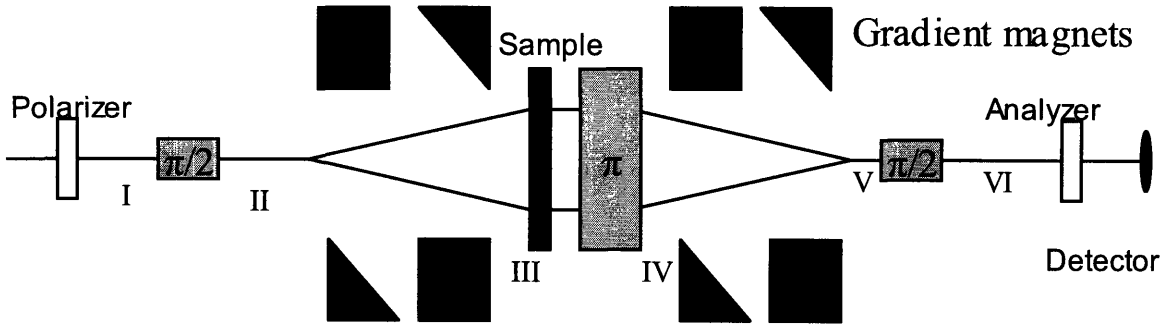

$$\text{I}\quad |\uparrow\rangle|x\rangle$$

$$\text{II}\quad \frac{1}{\sqrt{2}}\left(|\uparrow\rangle|x\rangle+|\downarrow\rangle|x\rangle\right)$$

$$\text{III}\quad \frac{1}{\sqrt{2}}\left(e^{i\sigma(x)t}|\uparrow\rangle|x\rangle+e^{i\sigma(x+\Delta x)t}|\downarrow\rangle|x+\Delta x\rangle\right)$$

$$\text{IV}\quad \frac{1}{\sqrt{2}}\left(e^{i\sigma(x)t}|\downarrow\rangle|x\rangle+e^{i\sigma(x+\Delta x)t}|\uparrow\rangle|x+\Delta x\rangle\right)$$

$$\text{V}\quad \frac{1}{\sqrt{2}}\left(e^{i\sigma(x)t}|\downarrow\rangle|x\rangle+e^{i\sigma(x+\Delta x)t}|\uparrow\rangle|x\rangle\right)$$

$$\text{VI}\quad e^{i[\sigma(x)t-\sigma(x+\Delta x)t]}|\uparrow\rangle|x\rangle$$

$$\boxed{S(q)=\int\rho(x)e^{i[\sigma(x)t-\sigma(x+\Delta x)t]}d\Omega}$$

$$\text{where}\quad \Delta x=\gamma\frac{dB}{dx}\left(\frac{L_m}{v}\right)^2$$

Figure 1-4: Explicit wave functions of the neutron in the Stern-Gerlach neutron interferometer.

in Section 1.2.

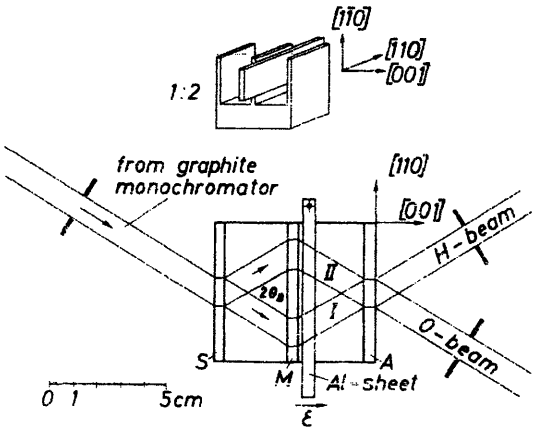

Fig. 1. Sketch of the perfect crystal neutron spectrometer.

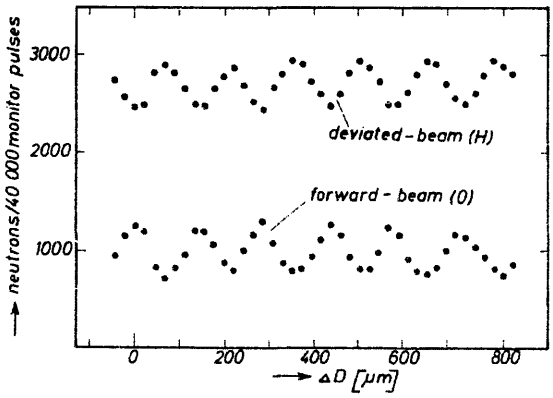

Fig. 2. Measured intensity modulation of the deviated and forward beam as a function of the different optical paths for beam I and II within an Al-sheet. (The statistical error is smaller than the size of the points.)

Figure 1-5: Sketch of the perfect crystal neutron interferometer (LLL-type) on the left and the data obtained at the O and H beam detectors vs phase flag position on the right [8]. This example shows a relatively low contrast of about 20%

There are other types of neutron interferometers that are based on single crystals,

see review by W. Graeff in reference [11]. We will mention here only a double crystal neutron interferometer, that was proposed by S. Kikuta *et al.* [12] for Laue and Bragg (scattering crystal planes are parallel to the blades of the interferometer) cases (shown on the left of figure 1-6). The LL-type is discussed by Zeilinger, Shull, Horne, and Squires in the book "Neutron Interferometry" [11] and the interference of Bragg-Bragg-case (BB) interferometer due to phase flag position is shown on the right of figure 1-6. Here the beam is split by the first crystal (reflection from the front and back of the crystal) and the two split beams recombine and interfere at the second crystal. Interference is observed at the exit of the second crystal.

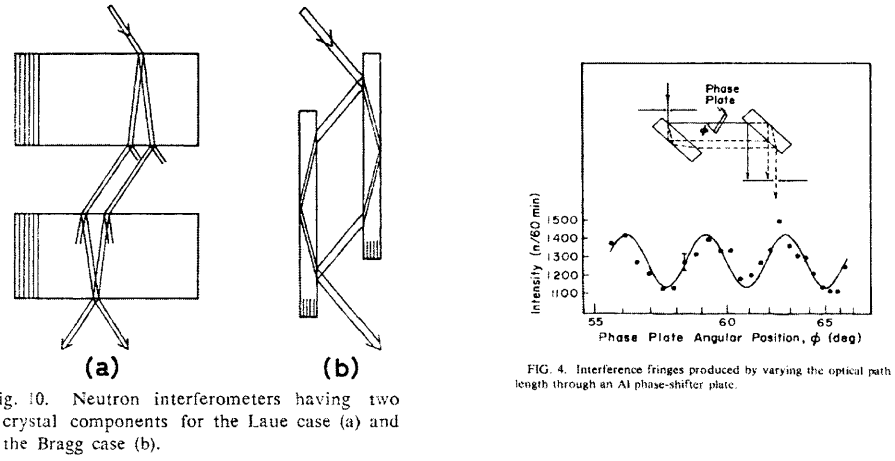

Fig. 10. Neutron interferometers having two crystal components for the Laue case (a) and the Bragg case (b).

FIG. 4. Interference fringes produced by varying the optical path length through an Al phase-shifter plate.

Figure 1-6: Sketch of the double perfect crystal neutron interferometer on the left [12] and the data obtained for the Bragg case double crystal neutron interferometer [13].

The use of diffraction grating can extend the Mach-Zehnder interferometer to the study of very slow neutrons. In 1985, Ioffe, Zabiyakin, and Drabkin presented a test of a diffraction grating neutron interferometer [14]. The diagram of the experiment is shown in figure 1-7. The incident beam here is diffracted by splitter BS_1 to the 0 and +1 orders of diffraction, then the beams are recombined on the second grating BS_2 by mirrors. The length of this interferometer is about 55 cm and the beam separation is on the order of 1 mm.

The last interferometer I will mention here is also for long wavelength neutrons. It is based on multi-layer diffraction and was tested by Funahashi *et al.* in 1996 for 12.6 $\AA$

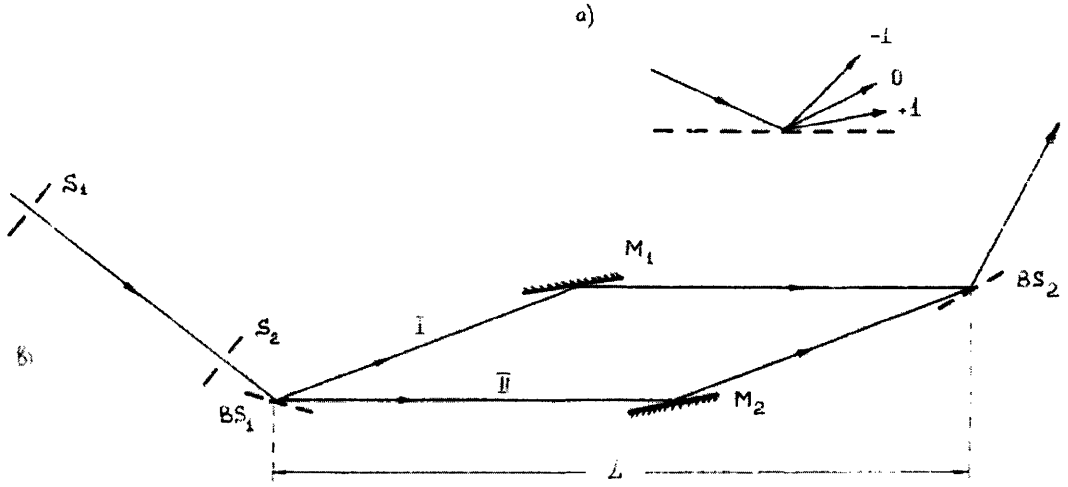

Figure 1-7: Diagram of diffraction grating neutron interferometer (b), and rule of signs for diffraction orders (a) [14].

neutrons [15]. The left graph of figure 1-8 shows the diagram of this interferometer consisting of two pairs of two multi-layer mirrors separated by a distance D.

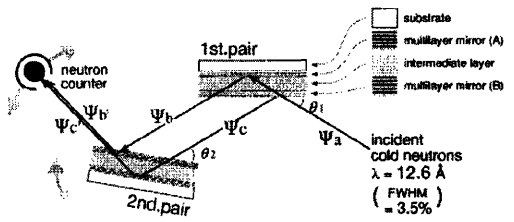

FIG. 1. Schematic diagram of the multilayer interferometer. The glancing angles off the first and the second pairs are denoted by θ_1 and θ_2, respectively.

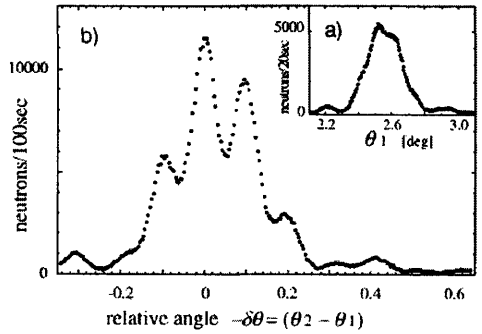

FIG. 3. Effective distance D between the two multilayer mirrors contained in a single pair is 3700 Å and the unit bilayer thickness of each multilayer mirror d is 140 Å. (a) Intensity of neutrons reflected off a single pair. (b) Interference fringes observed by changing the relative angle between the first and second pairs.

Figure 1-8: On the left: the diagram of the multi-layer neutron interferometer; on the right: rotation scan of the multi-layer mirrors [15].

The phase difference between the two neutron beam paths is

$$\Delta\Phi \approx 2\pi \frac{2D}{\lambda}\delta\theta, \tag{1.4}$$

where λ is the neutron wavelength and $\delta\theta = \theta_1 - \theta_2$ is the relative angle between the pairs of mirrors. The right graph of figure 1-8 shows the intensity scan of $\delta\theta$.

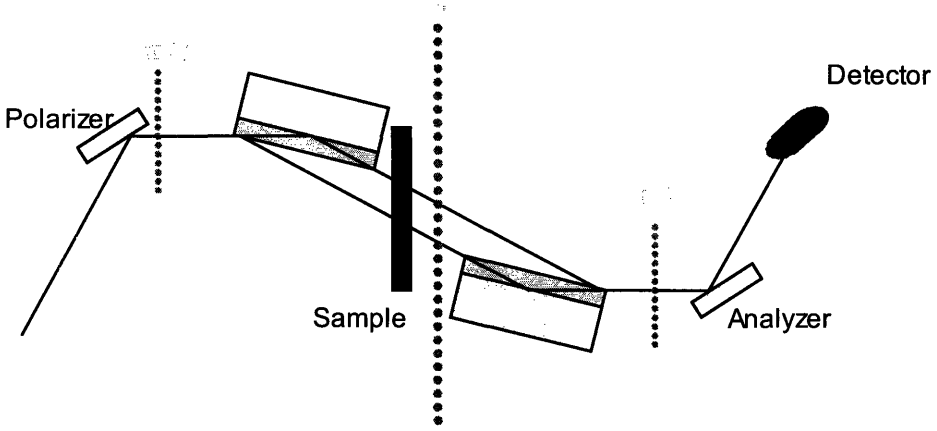

Figure 1-9: On the left: sketch of the magnetic multi-layer neutron interferometer; on the right: rotation scan of multi-layer mirrors [15].

A sketch of a similar interferometer but using magnetic multi-layer mirrors is shown in figure 1-9. Here each mirror reflects only one component of the neutron spin. This interferometer is analogous to the Stern-Gerlach interferometer without the use of gradient magnets.

Over the past 40 years there has been an evolution of neutron interferometer where both the momentum and spin can be used to demonstrate the wave-properties. For many studies a key parameter is the distance of the separation. Large, cm or larger, path separations permit convenient use of neutron interferometers for high resolution studies of materials properties and for studies of the interaction between neutron and fields. In this case we can place a sample or create the field just in one of the paths leaving the other path unchanged. The most versatile and robust neutron interferometer with a large path separation is the LLL-type. In the next section, we focus the discussion on the LLL-type single crystal interferometer which was used to perform the experiments described in this thesis.

1.2 LLL Single Crystal Neutron Interferometer

For most applications, the standard Laue-Laue-Laue (LLL) interferometer is the best configuration. This interferometer is functionally the equivalent of an optical Mach-Zehnder (MZ) interferometer (figure 1-10). The MZ interferometer has two mirrors and two beam splitters (half-mirrors). Light from a source is split by the first half-mirror and refocused on the second beam splitter by mirrors. There are two detector locations 1 and 2. When a light is incident on a surface and the material on the other side of the surface has a higher index of refraction, then the reflected light phase is shifted by π. There is no phase change because the light reflects from the surface with lower index of refraction and then the light is refracted due to the medium change. The index of refraction of a perfect mirror can be thought of as infinite, thus shifting the reflected light by π. Following the figure schematics for the "U" path and detector 1 we accumulate the following phases: reflection (π) from half-mirror, reflection (π) from mirror, transmission through the second half mirror (δ - small phase shift due to the media of the beam splitter) and optical path between the first and the second beam-splitters (Φ). For the path "D" and detector 2 we have transmission through the first half mirror (δ), reflection (π) from mirror, reflection (π) from half-mirror, and optical path between the first and the second beam-splitters which is usually the same as for the "U"-path (Φ). Than the total phase difference for different paths is zero and we would observe constructive interference. For the same paths but at detector 2 the total phase difference is π, thus we observe destructive interference. The LLL neutron interferometer is directly analog to the MZ except we do not have convenient mirrors

The atomic planes of the blade act as a diffraction grating and coherently split or reflect an incoming beam whose wavelength satisfies the Bragg condition (see figure 1-11)

$$\lambda = 2d \sin \theta_{Bragg}, \tag{1.5}$$

where d is the atomic plane spacing and θ_{Bragg} is the angle between the incoming beam and the atomic planes. The amplitudes of the transmitted and reflected beams

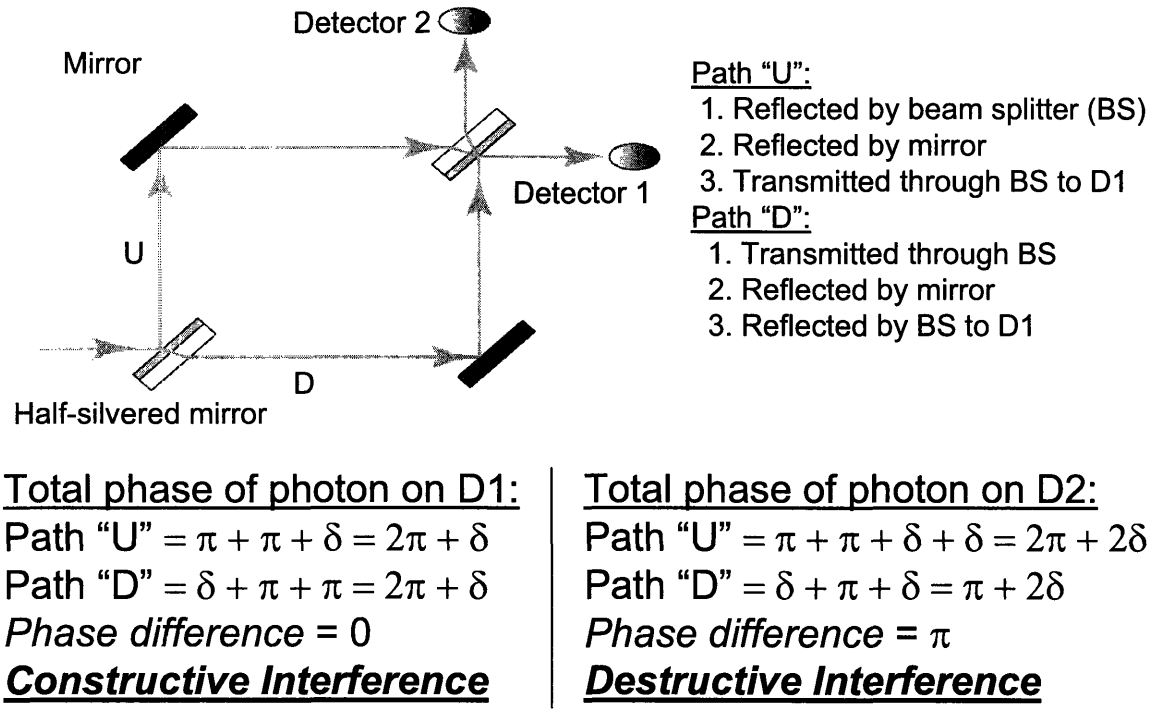

Figure 1-10: Principle of optical Mach-Zehnder interferometer.

are defined by the coefficients t and r respectively. Both r and t are complex function of $(|k-k_{Bragg}|)$, where k is the wave vector of the neutron and k_{Bragg} is the wave vector which exactly satisfies the Bragg condition. Coefficients r and t can be determined from dynamical diffraction equations for each slab and $\arg(r) = \arg(t) \pm \pi/2$. In other words, the Bragg-reflected and transmitted waves are 90° out of phase. A detailed description of the theory could be found in references [16] and [17].

The top view of the neutron interferometer is shown in figure 1-12, where explicit neutron wave-functions, at different stages of the interferometer, are also given. The amplitude of the neutron wave packet that traverses along *path I* and reaches the O-detector is rrt due to two reflections and one transmission.

Here we write the wave functions of the neutron in the two pathes as $= |\mathrm{I}\rangle$ for *path I* and $= |\mathrm{II}\rangle$ for *path II*, and treat the interference at the third blade and the detection by the O or H detectors as an projection operator. Thus the wave function

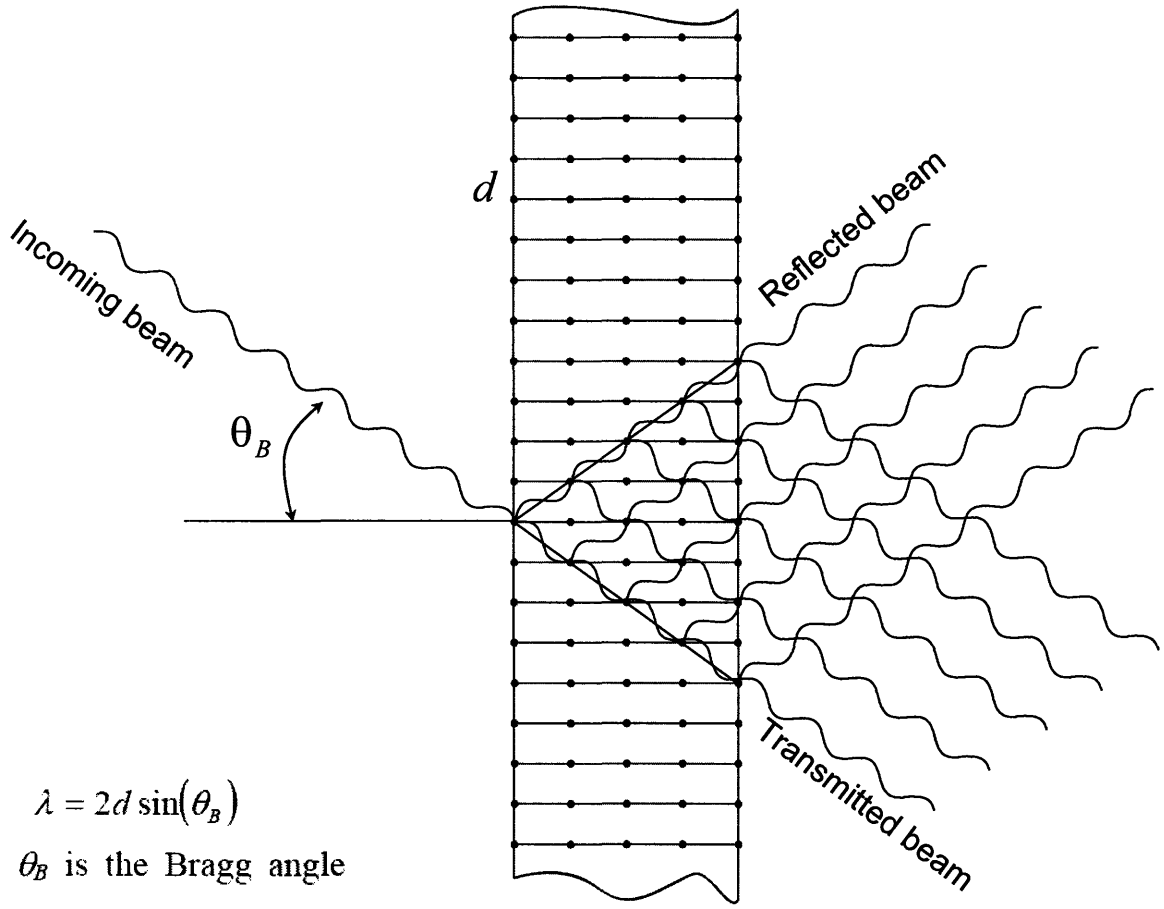

Figure 1-11: Laue geometry. A neutron beam coherently splits at each blade due to Bragg diffraction on the crystal atomic planes.

of the neutron inside the interferometer can be written as,

$$\Psi = C_1 e^{i\phi_1}|\mathrm{I}\rangle + C_2 e^{i\phi_2}|\mathrm{II}\rangle, \tag{1.6}$$

where ϕ_1 and ϕ_2 are the accumulated phases of the neutron along *path I* and *path II* correspondingly. The amplitudes are $C_1 = rt$ and $C_2 = rr$. We can rewrite this wave function substituting in the coefficients,

$$|\Psi\rangle = rte^{i\phi_1}|\mathrm{I}\rangle + rre^{i\phi_2}|\mathrm{II}\rangle. \tag{1.7}$$

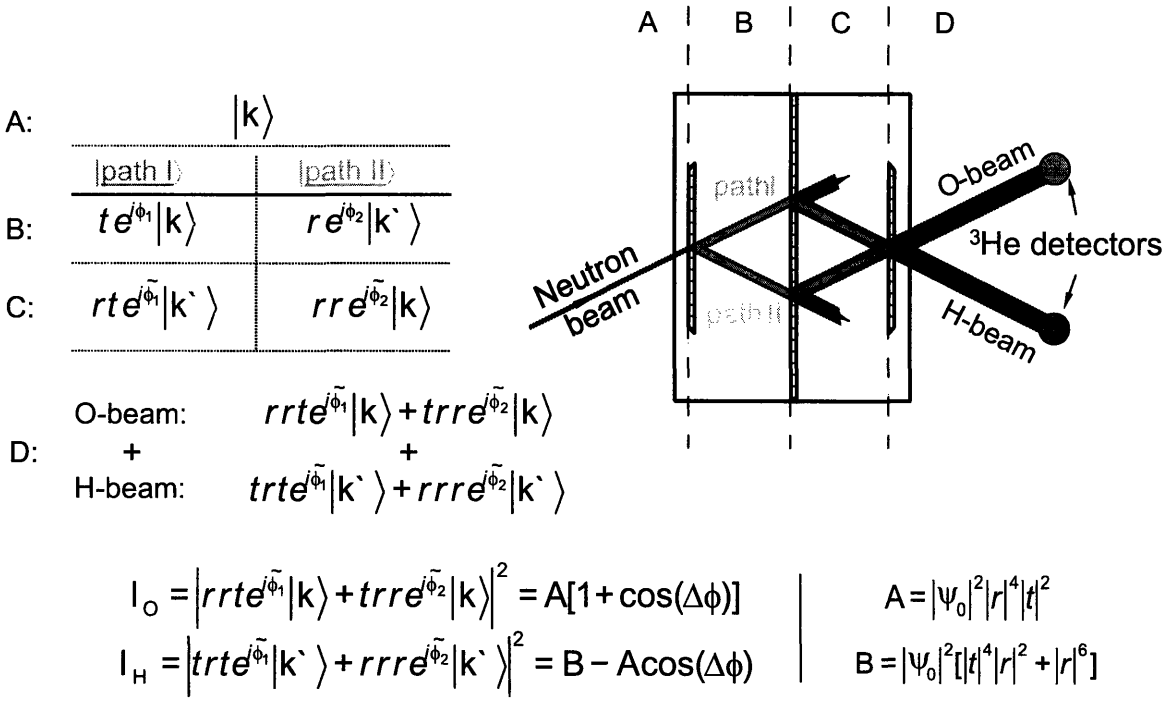

Figure 1-12: Diagram of neutron beam paths inside a single crystal interferometer.

The projection operator of the wave function onto the O-beam detector P_O is,

$$P_O = \frac{1}{2}\left(r|\mathrm{I}\rangle + t|\mathrm{II}\rangle\right)\left(r^*\langle\mathrm{I}| + t^*\langle\mathrm{II}|\right), \tag{1.8}$$

while the projection operator onto the H-beam detector P_H is

$$P_H = \frac{1}{2}\left(t|\mathrm{I}\rangle + r|\mathrm{II}\rangle\right)\left(t^*\langle\mathrm{I}| + r^*\langle\mathrm{II}|\right). \tag{1.9}$$

Therefore, the intensities on the O- and H-detectors are

$$\begin{aligned} I_O &= |\langle\Psi|P_O|\Psi\rangle| = |r|^4|t|^2\left[1+\cos\left(\phi_2-\phi_1\right)\right], \\ I_H &= |\langle\Psi|P_H|\Psi\rangle| = \left[|t|^4|r|^2 + |r|^6\right] - |r|^4|t|^2\cos\left(\phi_2-\phi_1\right). \end{aligned} \tag{1.10}$$

From these equations, we see that in the case of an ideal single crystal interferometer and a monoenergetic, non-divergent incoming beam, the contrast of the interferometer $C = \frac{\max\{I\}-\min\{I\}}{\max\{I\}+\min\{I\}}$ for the O-beam will be 100%, while for H-beam it depends on r

and t.

$$C_O = \frac{\max\{I_O\} - \min\{I_O\}}{\max\{I_O\} + \min\{I_O\}} = 1,$$
$$C_H = \frac{\max\{I_H\} - \min\{I_H\}}{\max\{I_H\} + \min\{I_H\}} = \frac{|r|^4|t|^2}{|t|^4|r|^2 + |r|^6}. \quad (1.11)$$

Of course, in the non-ideal case or when environmental disturbances are present, the contrast of the interferometer is reduced. Detailed discussions of the reduction in contrasts can be found in Chapter 5 which discusses vibrational disturbances, Chapter 4 which deals with temperature variations and the separation of beams, and Chapter 3 which describes the effects of phase gradients along the beam.

When we explore the coherence length measurement and the use of neutron interferometer for scattering in the latter chapters it will be helpful to have an operator picture of the action of the blades in a neutron interferometer. We develop this now.

1.3 Operator Picture of the Neutron Interferometer.

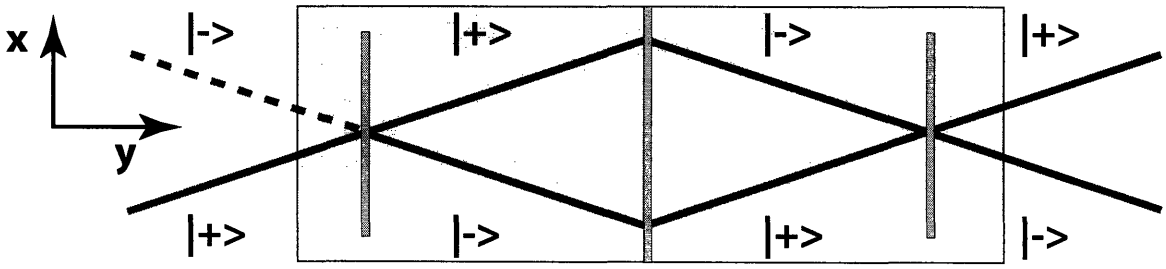

Figure 1-13: A schematic diagram of the 3-blade neutron interferometer. A neutron beam comes from the left, splits by the first blade, gets diffracted on the second blade and recombines at the third. After passing interferometer, the beam captured by O and H detectors.

Figure 1-13 presents a schematic diagram of 3-blade (LLL-type) neutron interferometer. A neutron beam coming from the left is coherently split in two paths by the first blade via Bragg scattering. These two paths are partially reflected by the second blade, recombined on the third blade, and thus interfere before reaching the O or H detectors.

We label the states according to the sign of k_x, the neutron momentum in the **x** direction (see figure 1-13). The incoming neutron is therefor in the $|+\rangle$ state. For the incoming beam

$$\rho_{in} = |+\rangle\langle+|. \tag{1.12}$$

The operator describing Bragg scattering is

$$\hat{O}_B = \begin{pmatrix} t_+ & r_- \\ r_+ & t_- \end{pmatrix}, \tag{1.13}$$

where t_+, r_- are the transmission and reflection coefficients for the neutron going "up" and t_-, r_- are the transmission and reflection coefficients for the neutron going "down". This operator has to be a unitary operator, which implies in this case that for complex r and t the relations $t = t_+ = t_-^*$, $r = r_+ = -r_-^*$ and $|r|^2 + |t|^2 = 1$ hold. Thus the blade operator is

$$\hat{O}_B = \begin{pmatrix} t & -r^* \\ r & t^* \end{pmatrix}. \tag{1.14}$$

The operator for a phase-shifter in the $|+\rangle$ beam path is described by the operator

$$\hat{\Phi} = \begin{pmatrix} e^{\imath\phi_0} & 0 \\ 0 & 1 \end{pmatrix}. \tag{1.15}$$

The operator for the central blade is more complex. If for the moment we neglect the loss of transmitted neutrons, then we can approximate the action as that of mirror. The projection of the density operator on the paths is realized through the operators

$$\hat{P}_+ = |+\rangle\langle+| = \begin{pmatrix} 1 & 0 \\ 0 & 0 \end{pmatrix} \tag{1.16}$$

and

$$\hat{P}_- = |-\rangle\langle-| = \begin{pmatrix} 0 & 0 \\ 0 & 1 \end{pmatrix}. \tag{1.17}$$

So the overall action is

$$\hat{B}_2 = [\hat{P}_+\hat{O}_{B_2}\hat{P}_- + \hat{P}_-\hat{O}_{B_2}\hat{P}_+]. \tag{1.18}$$

An ensemble of neutrons starting in the $|+\rangle$ state propagate through the interferometer to the outgoing state

$$\rho_{out} = \hat{O}_{B_3}\hat{\Phi}\hat{B}_2\hat{O}_{B_1}\rho_{in}\hat{O}^\dagger_{B_1}\hat{B}^\dagger_2\hat{\Phi}^\dagger\hat{O}^\dagger_{B_3}. \tag{1.19}$$

By treating the second blade as a mirror we have renormalized the probabilities of the neutron detection at O and H to neglect those neutrons lost by transmission. For most experiments this corresponds to the desired information. If, however, the lost neutron carries away information we must include this in the description.

1.3.1 Re-normalizing the second blade operator.

If we assume that the lost neutrons do not carry away any information from the system, then we can re-normalize the system (i.e. assume that 2^{nd} blade act as a perfect mirror). Using this assumption we can re-normalize the second blade operator as

$$\hat{B}_{2n} = \begin{pmatrix} 0 & -r^* \\ r & 0 \end{pmatrix} \Longrightarrow \begin{pmatrix} 0 & -e^{-\imath \arg(r)} \\ e^{\imath \arg(r)} & 0 \end{pmatrix}. \tag{1.20}$$

The O-detector will measure the projection of ρ_{out} on the $|+\rangle$ state.

$$I_O = Tr(\hat{P}_+\rho_{out}), \tag{1.21}$$

Using 1.20 we can find

$$\hat{A}_1 = \hat{O}_{B_3}\hat{\Phi}\hat{B}_{2n}\hat{O}_{B_1} = \begin{pmatrix} -|r|t(1+e^{\imath\phi_0}) & -|t|^2e^{\imath(\phi_0-\arg(r))} + |r|r^* \\ |t|^2e^{\imath\arg(r)} - r|r|e^{\imath\phi_0} & -|r|t^*(e^{\imath\phi_0}+1) \end{pmatrix} \tag{1.22}$$

and using 1.12 as incoming density

$$\rho_{out} = \hat{A}_1 \rho_{in} \hat{A}_1^\dagger = \begin{pmatrix} 2|rt|^2(1+\cos\phi_0) & (|r|^2 - |t|^2 e^{\imath\phi_0})(1+e^{-\imath\phi_0})tr^* \\ (|r|^2 - |t|^2 e^{-\imath\phi_0})(1+e^{\imath\phi_0})rt^* & |t|^4 + |r|^4 - 2|rt|^2\cos\phi_0 \end{pmatrix}. \quad (1.23)$$

And finally the intensities on the O- and H-detectors (using 1.21) are (as expected)

$$I_O = Tr(\hat{P}_+ \rho_{out}) = 2|rt|^2 (1+\cos\phi_0), \quad (1.24)$$

$$I_H = Tr(\hat{P}_- \rho_{out}) = (|r|^4 + |t|^4) - 2|rt|^2\cos\phi_0. \quad (1.25)$$

1.3.2 Using the superoperator and Kraus-decomposition

An approach to include the non-unitary dynamics of the second blade operator is to represent its action by means of a superoperator. The corresponding quantum operator must of course be convex-liner and completely positive, as well as trace non-increasing. Note that even though the action of the second blade is not trace-preserving, we still fulfill the above condition.

We will construct the super-operator over the Hilbert space $\{|+rangle, |-\langle\}$, where the second blade operator acts as

$$\begin{aligned} |+\rangle &\rightarrow r|-\rangle', \\ |-\rangle &\rightarrow -r^*|+\rangle'. \end{aligned} \quad (1.26)$$

The form operators of the Hilbert space are transformed by the super-operator of the second blade as

$$\$: \left\{ \begin{array}{lcl} |+\rangle\langle+| & \rightarrow & |r|^2|-\rangle'\langle-|' \\ |+\rangle\langle-| & \rightarrow & -r^2|-\rangle'\langle+|' \\ |-\rangle\langle+| & \rightarrow & -r^{*2}|+\rangle'\langle-|' \\ |-\rangle\langle-| & \rightarrow & |r|^2|+\rangle'\langle+|' \end{array} \right\}. \quad (1.27)$$

In a matrix form the super-operator is

$$\$ = \begin{pmatrix} 0 & 0 & 0 & |r|^2 \\ 0 & 0 & -r^2 & 0 \\ 0 & -r^{*2} & 0 & 0 \\ |r|^2 & 0 & 0 & 0 \end{pmatrix}. \tag{1.28}$$

We can also write it in the Pauli basis $\{\mathbf{1}, \sigma_x, \sigma_y, \sigma_z\}$ as

$$\$_P = T^\dagger \$ T = \begin{pmatrix} |r|^2 & 0 & 0 & 0 \\ 0 & -\frac{\imath}{2}(r^2 + r^{*2}) & \frac{\imath}{2}(r^2 - r^{*2}) & 0 \\ 0 & \frac{\imath}{2}(r^2 - r^{*2}) & \frac{\imath}{2}(r^2 + r^{*2}) & 0 \\ 0 & 0 & 0 & -|r|^2 \end{pmatrix}, \tag{1.29}$$

where change of basis matrix between different basis T is

$$T = \frac{1}{\sqrt{2}} \begin{pmatrix} 1 & 0 & 0 & 1 \\ 0 & 1 & \imath & 0 \\ 0 & 1 & -\imath & 0 \\ 1 & 0 & 0 & -1 \end{pmatrix}. \tag{1.30}$$

Let's represent the superoperator $\$$ as a Kraus sum. For that we write the Choi matrix:

$$\mathcal{C} = \begin{pmatrix} \$(|+\rangle\langle+|) & \$(|+\rangle\langle-|) \\ \$(|-\rangle\langle+|) & \$(|-\rangle\langle-|) \end{pmatrix} = \begin{pmatrix} 0 & 0 & 0 & 0 \\ 0 & |r|^2 & -r^2 & 0 \\ 0 & -r^{*2} & |r|^2 & 0 \\ 0 & 0 & 0 & 0 \end{pmatrix}. \tag{1.31}$$

The eigenvalues of the Choi matrix can be found from the equation:

$$\det(\mathcal{C} - \lambda \mathbf{1}) = \lambda^2((\lambda - |r|^2)^2 - |r|^4) = 0, \tag{1.32}$$

and are equal to:

$$\{\lambda_j\} = \{0, 0, 0, 2|r|^2\}. \tag{1.33}$$

The corresponding eigenvectors of the Choi matrix are:

$$\{\mathbf{e}_j\} = \left\{ \begin{pmatrix} 1 \\ 0 \\ 0 \\ 0 \end{pmatrix}, \begin{pmatrix} 0 \\ 0 \\ 0 \\ 1 \end{pmatrix}, \frac{1}{\sqrt{2}} \begin{pmatrix} 0 \\ r/r^* \\ 1 \\ 0 \end{pmatrix}, \frac{1}{\sqrt{2}} \begin{pmatrix} 0 \\ -r/r^* \\ 1 \\ 0 \end{pmatrix} \right\}. \tag{1.34}$$

The Kraus operators are then up to a global phase:

$$\{\mathcal{K}_j\} = \left\{\sqrt{\lambda_j}\mathbf{e}_j(\text{in the matrix form})\right\} = \left\{ \begin{pmatrix} 0 & 0 \\ 0 & 0 \end{pmatrix}, \begin{pmatrix} 0 & -r^* \\ r & 0 \end{pmatrix} \right\}. \tag{1.35}$$

That one of the Kraus operators is zero naturally corresponds to a loss of neutron. That the other is propotional to a perfect mirror completes the describtion. The output state of the interferometer is

$$\rho_{out} = \sum_j \hat{O}_{B_3} \hat{\Phi} \mathcal{K}_j \hat{O}_{B_1} \rho_{in} \hat{O}_{B_1}^\dagger \mathcal{K}_j^\dagger \hat{\Phi}^\dagger \hat{O}_{B_3}^\dagger, \tag{1.36}$$

or

$$\rho_{out} = \begin{pmatrix} 2|r^2 t|^2(1+\cos\phi_0) & -|r|^2(|t|^2 - |r|^2 e^{-\imath\phi_0})(1+e^{\imath\phi_0})tr^* \\ -|r|^2(|t|^2 - |r|^2 e^{\imath\phi_0})(1+e^{-\imath\phi_0})rt^* & |r|^2(|t|^4 + |r|^4 - 2|rt|^2\cos\phi_0) \end{pmatrix}. \tag{1.37}$$

Finally, the intensity at the O- and H-detectors (using 1.21) are

$$I_O = Tr(\hat{P}_+ \rho_{out}) = 2|r^2 t|^2 (1 + \cos\phi_0), \tag{1.38}$$

$$I_H = Tr(\hat{P}_- \rho_{out}) = |r|^2(|r|^4 + |t|^4) - 2|r^2 t|^2 \cos\phi_0. \tag{1.39}$$

Notice that in this description there is an apparent decrease in the neutron intensity at the detectors of $|r|^2$.

1.4 Coherent Neutron Interactions.

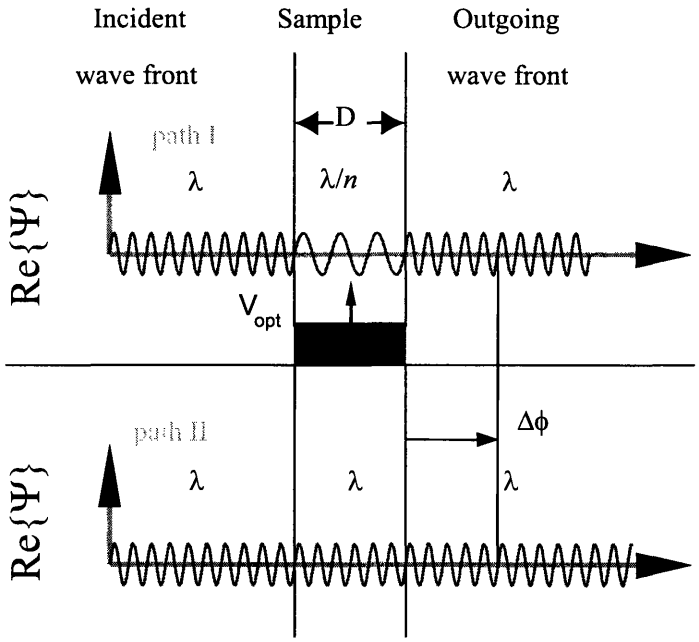

Figure 1-14: Change of the wavelength of the neutron inside the sample.

The presence of a sample inside the interferometer will change the phase of the neutron. In general, the phase of a neutron is proportional to its action S,

$$\phi = \frac{S}{\hbar}. \tag{1.40}$$

The accumulated phase of a neutron traversing path I is

$$\phi_1 = \frac{1}{\hbar}\left(S_0 + \int_{path\ I} \nabla S \cdot \mathbf{dl}\right). \tag{1.41}$$

Since the neutron momentum is given by $\hbar\mathbf{K} = \nabla S$, the above equation can also be written as

$$\phi_1 = \phi_0 + \int_{path\ I} \mathbf{K} \cdot \mathbf{dl}. \tag{1.42}$$

When a sample (or a phase flag) is present in the beam, it creates an optical potential V_o for neutrons. We introduce an index of refraction of the sample n for neutron optics. Analogous to light optics, n is proportional to the ratio of the neutron momenta inside

and outside the sample.

When a neutron scatters on the potential V_o, by the conservation of energy, the momentum of the neutron inside the potential q is,

$$q = \sqrt{\frac{2m_n(E - V_o)}{\hbar^2}}, \tag{1.43}$$

where m_n is the mass of the neutron and $E = \hbar^2 k^2 / 2m_n$ is the kinetic energy of the neutron before scattering. Therefore, the index of refraction is

$$n = q/k = \sqrt{1 - \frac{V_o}{E}}. \tag{1.44}$$

The wave function of a scattered neutron will be the sum of plane wave (incoming) and the spherical wave (due to scattering). Since the neutron wavelength in our case is much larger than the size of the nuclei, the neutron scattering amplitude is isotropic, and equals the neutron coherent scattering length b_c. Thus the potential of neutron-nucleus interaction can be written as a delta function [17],

$$V_o(\mathbf{r}) = \frac{2\pi\hbar^2}{m_n} b_c \delta(\mathbf{r}). \tag{1.45}$$

Consider now an ensemble of nuclei whose positions are given by $\mathbf{R}_i$. We can express its optical potential as a sum of interactions with each individual nucleus,

$$V_o(\mathbf{r}) = \frac{2\pi\hbar^2}{m_n} \sum_i b_c^i \delta(\mathbf{r} - \mathbf{R}_i). \tag{1.46}$$

Defining $\overline{b_c}$ as,

$$N\overline{b_c} = \sum_i b_c^i \delta(\mathbf{r} - \mathbf{R}_i), \tag{1.47}$$

we can rewrite the optical potential as,

$$V_o = \frac{2\pi\hbar^2}{m_n} N\overline{b_c}, \tag{1.48}$$

and the index of refraction as,

$$n = \sqrt{1 - \frac{4\pi N \overline{b_c}}{k^2}}, \tag{1.49}$$

where N is the number of atoms per unit volume.

The phase shift due to the sample can be now written using the refractive index of the sample (eq. (1.49)),

$$\phi_{sample} = \int_{path\ I} \mathbf{nk} \cdot \mathbf{dl}. \tag{1.50}$$

Thus the phase difference between two interferometer paths is

$$\Delta\phi = \phi_2 - \phi_1 = \int_{sample} (1-n)\mathbf{k} \cdot \mathbf{dl} \approx -Nb_c\lambda D, \tag{1.51}$$

where D is the thickness of the sample (or the length of the neutron path through the sample). Figure 1-14 gives a visual representation of the phase difference inside the interferometer due to the sample. Measuring this phase shift gives a very precise measurement of the coherent scattering length of the sample nuclei. In addition, phase shifts can also be introduced by neutron interactions with a magnetic field and gravitational field. Table 1.1 summarizes the optical potentials and phase shifts of neutrons due to the various interactions.

Using the phase flag (figure 1-15) as a phase shifter, we can measure the interference curve, which is the counting rate measured by the ^{3}He detectors as a function of the flag rotation. From these measurements, we can extract the contrast of the interferometer.

Figure 1-16 shows one of these phase scans. It is a high-contrast interference pattern obtained with a perfect silicon crystal interferometer by M. Arif and D.L. Jacobson at NIST, in 1997.

Interaction	Potential	Phase Shift	Reference
Nuclear	$\frac{2\pi\hbar^2}{m} b_c \delta(\vec{r})$	$-N b_c \lambda D$	Rauch et al. [8] (1974)
Magnetic	$-\vec{\mu} \cdot \vec{B}(\vec{r})$	$\pm \frac{\mu B m \lambda D}{2\pi\hbar^2}$	Rauch et al. [18] (1975)
Gravitation	$m\vec{g} \cdot \vec{r}$	$\frac{m_i m_g g \lambda A \sin(\alpha)}{2\pi\hbar^2}$	Collela et al. [19] (1975)
Coriolis	-$\hbar\omega \left(\vec{r} \times \vec{k}\right)$	$\frac{2m}{\hbar} \vec{\omega_e} \cdot \vec{A}$	Werner et al. [20] (1979)
Aharonov-Cashire (Schwinger)	$-\vec{\mu} \cdot \left(\vec{\nu} \times \vec{E}\right)/c$	$\pm \frac{2\mu}{\hbar c} \vec{E} \cdot \vec{D}$	Cimmino et al. [21] (1989)
Scalar Aharonov-Bohm	$-\vec{\mu} \cdot \vec{B}(t)$	$\pm \frac{\mu B T}{\hbar}$	Allman et al. [22] (1992)
Magnetic Josephson	$-\vec{\mu} \cdot \vec{B}(t)$	$\pm \omega t$	Badurec et al. [23] (1981)
Fizeau	N/A	$-N b_c \lambda D \left(\frac{w_x}{v_x - w_x}\right)$	Klein et al. [24] (1981)
Geometry (Berry)	N/A	$\Omega/2$	Wagh et al. [25] (1997)

Table 1.1: Table represents potentials and the associated phase shifts inside the interferometer for different interactions.

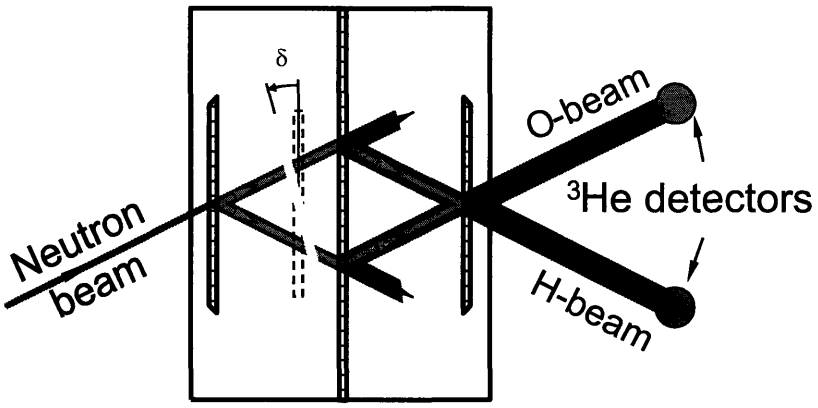

$$\Delta\phi(\delta) = -2Nb\lambda \frac{\sin^2(\theta_B)\sin(\delta)}{\cos^2(\theta_B) - \sin^2(\delta)} \approx (CONSTANT) \times \delta$$

Figure 1-15: Phase flag rotation changes the phase difference between interferometer paths.

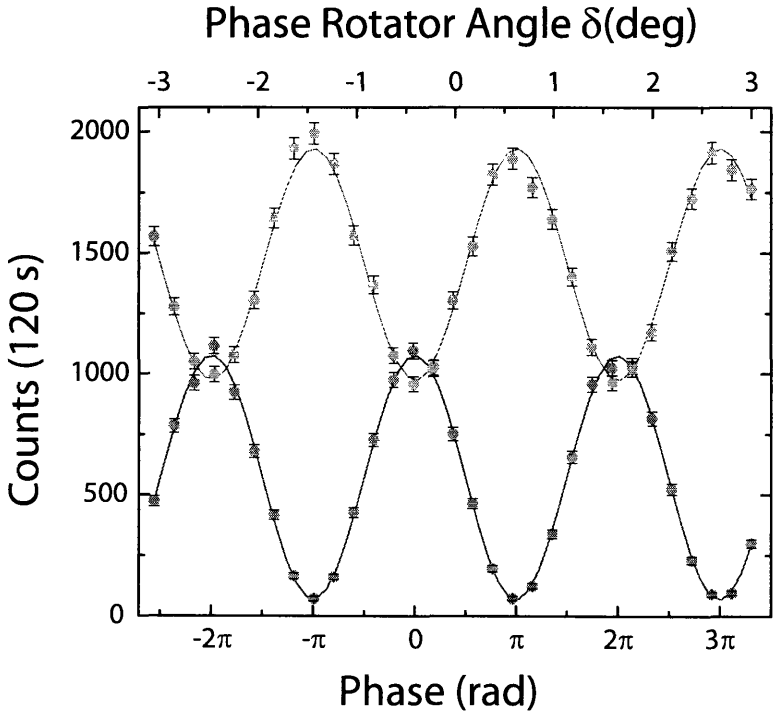

Figure 1-16: High-contrast interference pattern obtained with a perfect silicon crystal interferometer where the top curve is for H-detector and the bottom one corresponds to O-detector (courtesy of M. Arif and D.L. Jacobson, NIST, 1997 also [16]).

Chapter 2

Experimental Apparatus and Facilities

The experiments reported in this thesis were performed using the neutron interferometer setup at the Neutron Interferometry and Optics Facility (NIOF) at the National Institute of Standards and Technology (NIST) in Gaithersburg, MD. Details of the facility are described in Section 2.1. The alignment of the interferometer setup is a crytical procedure, since the interferometer is very sensitive to the wavelength and the direction of incoming neutrons. Proper alignment can dramatically increase the effective neutron flux, therefore decreasing statistical uncertainties of the measurements. Procedures and results of the interferometer alignment are presented in Section 2.2.

2.1 Neutron Interferometry and Optics Facility at the NIST Center for Neutron Research

2.1.1 The NIST Center for Neutron Research

The NIST center for Neutron Research (NIST) operates a 20 MW split-core research reactor. Fast neutrons ($\sim$1 MeV) are released from the nuclear fission of ^{235}U, and then thermalized by heavy water (D_2O) in the moderator to room temperature (300 K, 26 meV). The peak thermal neutron flux is 4×10^{14} neutrons/cm^2 at the reactor core.

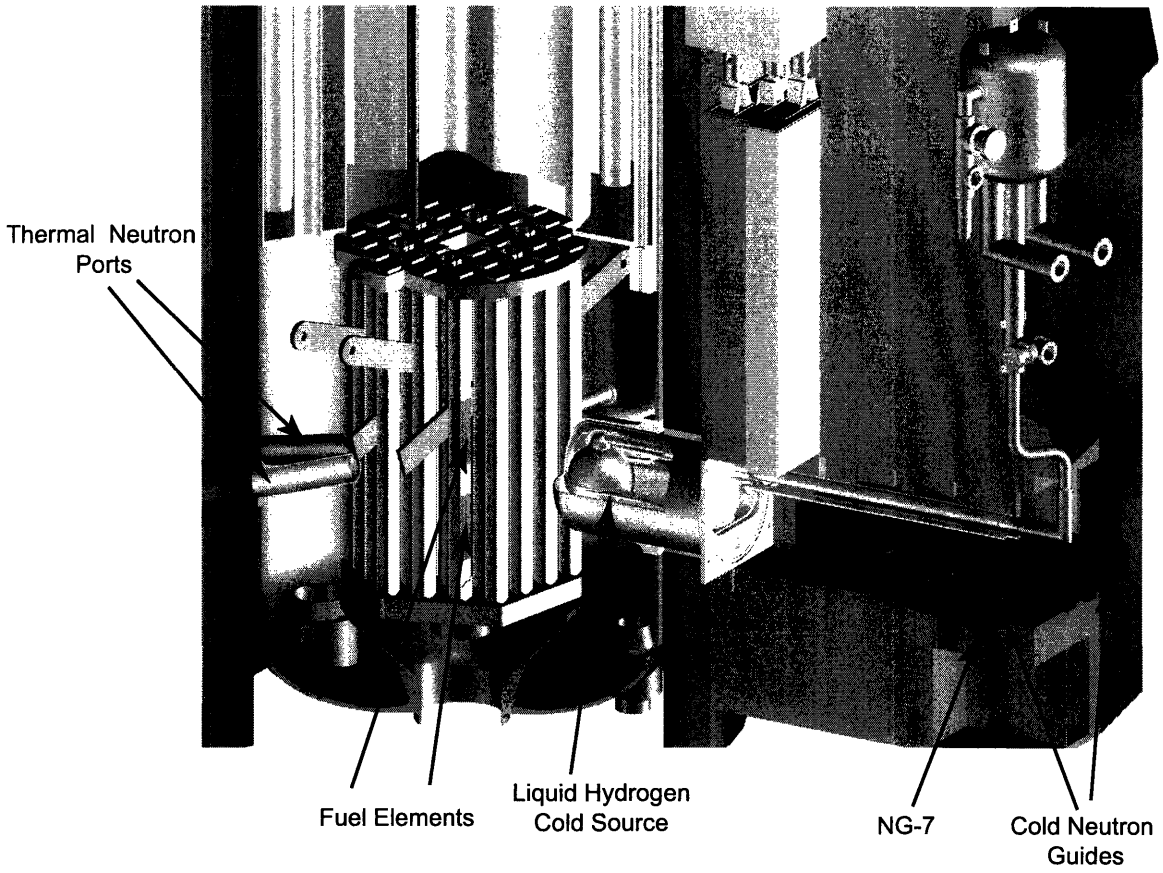

Figure 2-1: A cutaway view of the reactor core and cold source.

A cut-away view of the reactor core and cold source is shown in figure 2-1. The main advantage of the split-core reactor (fuel elements are located below and above the neutron ports) is the large reduction in gamma background without significant reduction in the neutron flux. The reactor is operated on a seven week cycle, with approximately 38 continuous days at full power (20 MW) operation followed by 11 days for refueling and maintenance.

There are eight thermal neutron ports (figure 2-2) available for development of radiation detectors, material science studies and neutron imaging [26]. Because longer wavelength ("cold", >1.8 Å and <25 meV) neutrons are better suited for the study of many condensed matter systems, a cold moderator [27] is installed next to the core. Thermal neutrons scatter with hydrogen atoms in this 20 K liquid hydrogen moderator to lower energies (see figure 2-1) and on the exit of the cold source, producing a

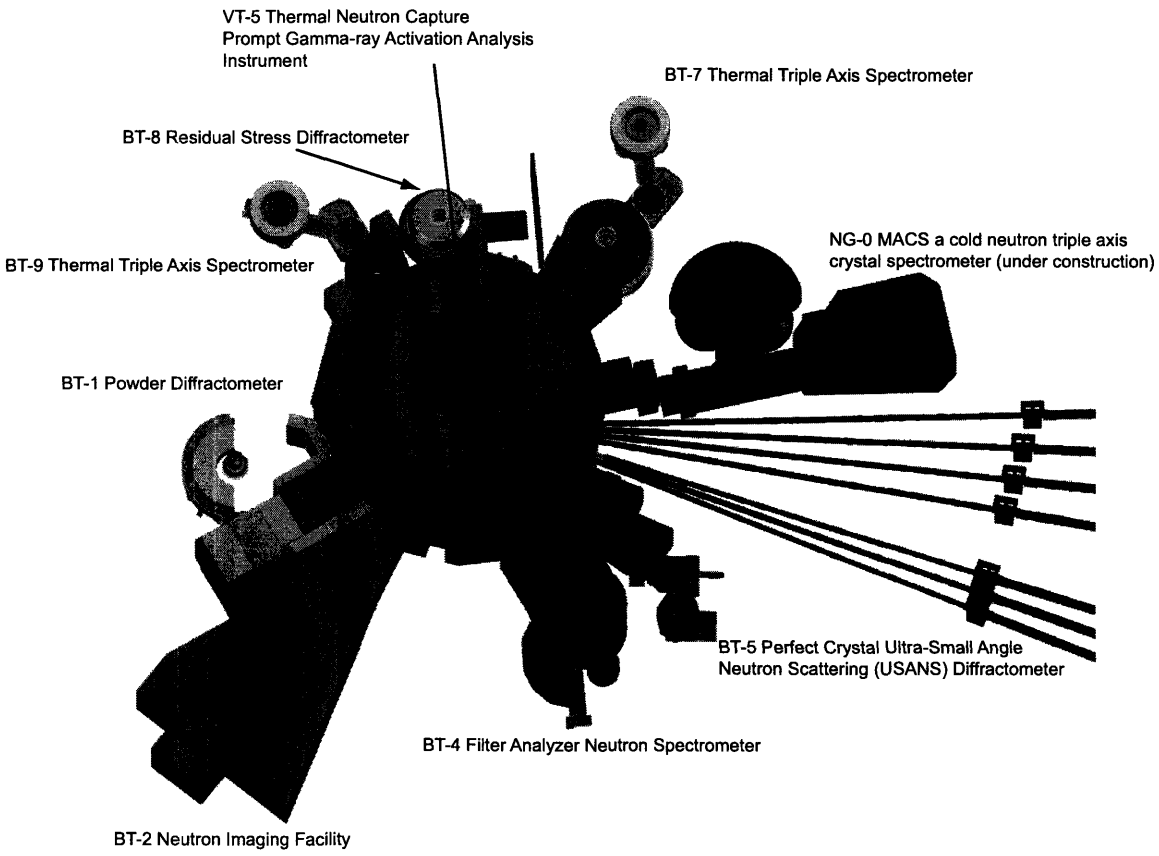

Figure 2-2: The thermal neutron instruments at the NIST Center for Neutron Research confinement building.

Maxwellian distribution with a characteristic temperature of 34 K.

Cold neutrons are transported to instruments throughout neutron guides. Figure 2-3 shows a schematic view of the NCNR guide hall. The neutron interferometer facility is located on the NG7 guide, shown in the figure as "NG-7 INT." Each neutron guide has a rectangularly shaped cross-section (15 cm tall and 6 cm wide) and is produced by gluing together 1 m long sections of ^{58}Ni coated (100 nm thick film) optically-flat borated glass plates. Nickel-58 is chosen as the coating material because it has one of the highest neutron reflective potentials

$$V = \frac{2\pi\hbar^2 Nb}{m} = 335\ neV. \tag{2.1}$$

If the perpendicular component of the neutron energy is less than the potential of

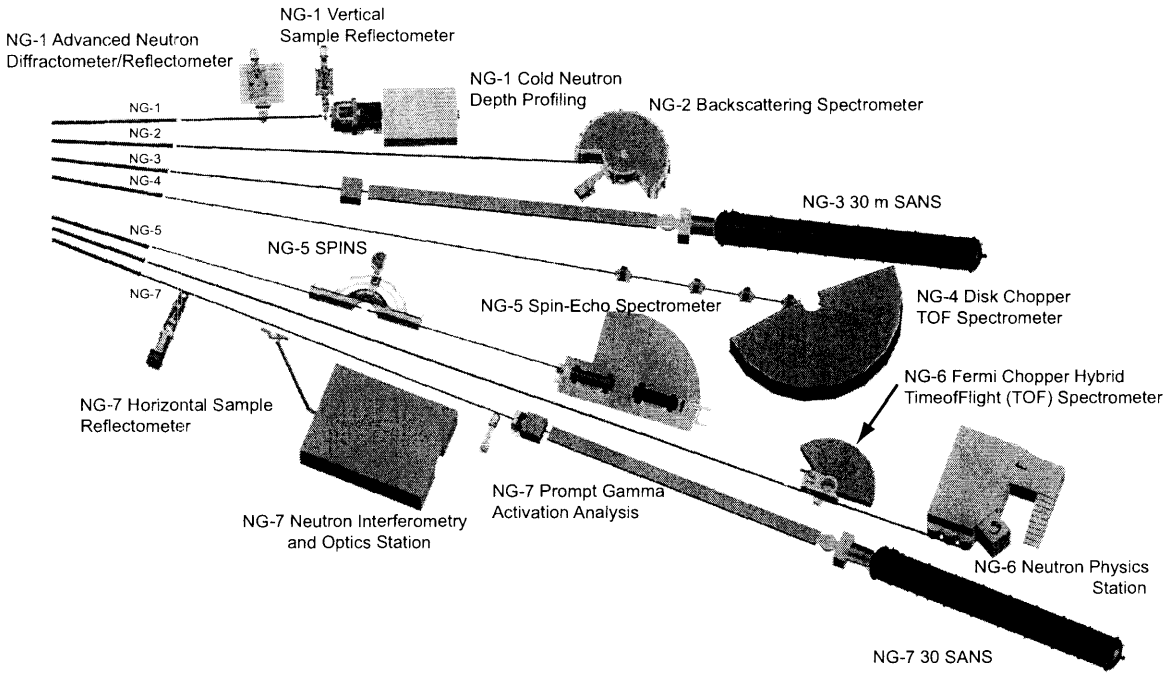

Figure 2-3: Top View of the NIST Center for Neutron Research Guide Hall.

the guide wall Eq. 2.1, then this neutron will be reflected from the wall. The critical angle of the guide is

$$\theta_{critical} \approx \lambda\sqrt{\frac{Nb}{\pi}} \approx 0.002 \text{ rad}/\mathring{A}. \tag{2.2}$$

Thus neutrons with grazing angles smaller than or equal to the critical angle will be reflected from the guide wall. To reduce the air scattering of neutrons, guides are pumped out to a few mTorr. The losses in the guides are mainly due to neutron absorption by the coating material, roughness of the guide surfaces, and guide misalignment.

2.1.2 Neutron Interferometry and Optics Facility

Figure 2-4 shows a schematic view of The Neutron Interferometry and Optics Facility (NIOF) located in the NCNR Guide Hall. NIOF is one of the world's premiere user facilities for neutron interferometry and related neutron optical measurements. The interferometer setup was designed in 1991 [28]. It is continuously being upgraded. It

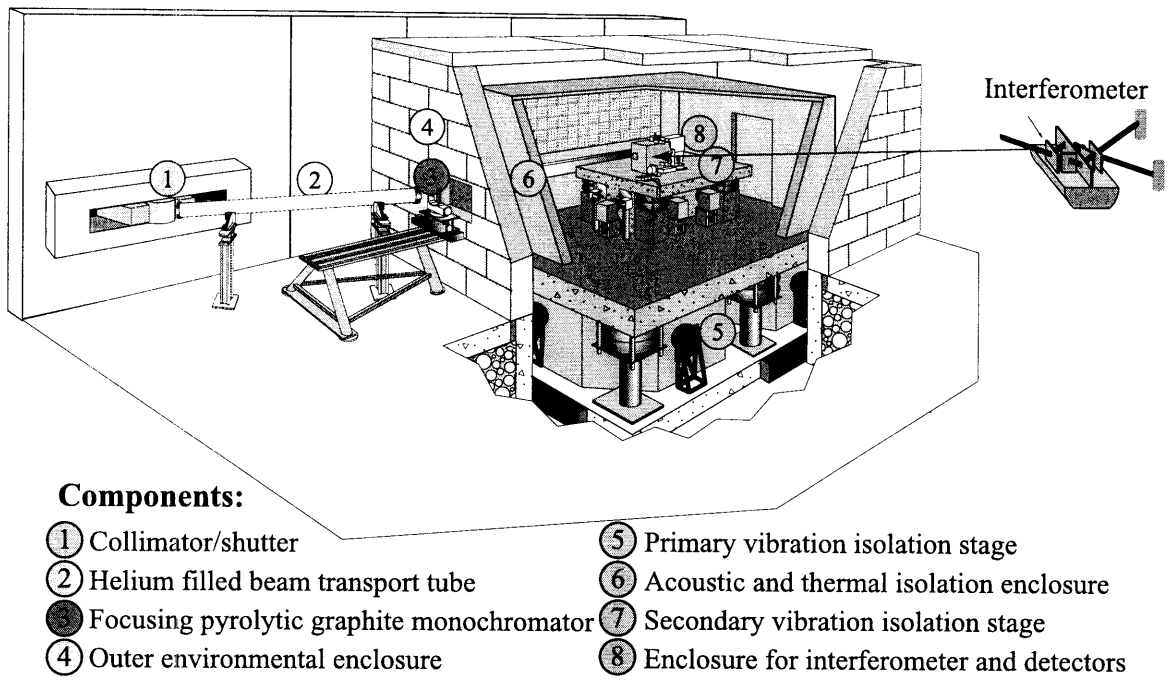

Components:

1. Collimator/shutter
2. Helium filled beam transport tube
3. Focusing pyrolytic graphite monochromator
4. Outer environmental enclosure
5. Primary vibration isolation stage
6. Acoustic and thermal isolation enclosure
7. Secondary vibration isolation stage
8. Enclosure for interferometer and detectors

Figure 2-4: Neutron Interferometry and Optics Facility.

was designed to provide a wide range of neutron energies (from 4 meV to 20 meV).

Neutrons are extracted from a dual-crystal parallel-tracking monochromator system (in figure 2-4, the first monochromator is located behind collimator/shutter (1) inside the NG-7 guide and the second focusing monochromator is indicated by (2)). Monochromators are made from pyrolytic graphite (002) (PG). The first monochromator is 7.5 cm high and 5 cm wide. The second (focusing) monochromator is 9 cm high and 5 cm wide and consists of nine (1 cm high and 5 cm wide) PG blades. By rotating each blade around the horizontal axis, we can focus the neutron beam onto the neutron interferometer and therefore increase the intensity of interferometer signals. For the range of neutron energies in use, the PG crystals are about 80% to 90% reflective.

In the area between the monochromators and the second monochromator and the interferometer enclosure, the beam passes through helium-filled transport tubes (which were recently replaced by vacuum beam transport tubes) to reduce neutron scattering and attenuation due to the air.

The neutron interferometer is very susceptible to environmental disturbances such

as temperature gradients (even small temperature gradients such as 1 mK over 10 cm distance due to the thermal expansion can shift blades with respect to each other by Å which is quite a big distance in comparison with the neutron wave length 2.71 Å and result in a big phase change) and vibrations from surrounding environment (we will discuss the effect of vibrations in the chapter 5). In order to perform high resolution measurements, special care needs to be taken to reduce (or eliminate) such environmental disturbances.

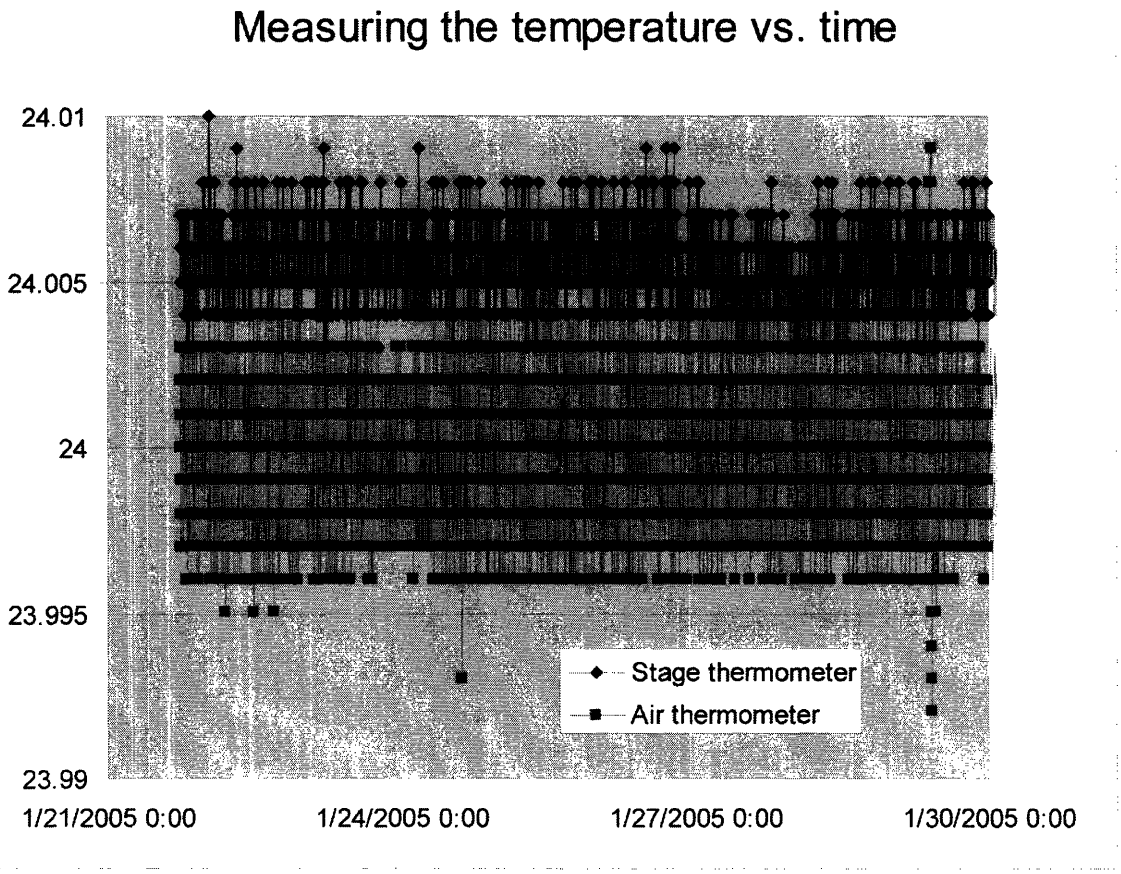

Figure 2-5: Time dependance of the temperature (in degrees of Celsius) inside the interferometer enclosure.

The perfect crystal interferometer is placed in three enclosures nested inside each other to maintain a very stable temperature and reduce temperature gradients. In figure 2-4, the three enclosures are shown as (4) - Outer environmental enclose, (6) - Acoustic and thermal isolation enclosure and (8) - Enclose for interferometer and

detectors. The outer enclosure is a large concrete block house with outer dimensions of $23 \times 17 \times 10$ feet. The acoustic and thermal isolation enclosure provides not only thermal but also acoustic isolation, and has dimensions of $15 \times 11 \times 8.5$ feet. The last enclosure for interferometer and detectors is made of aluminum and has dimensions of $2.25 \times 2.25 \times 2$ feet. To stabilize and monitor the temperature, we installed, inside aluminum box, a set of heaters and two Pt-100 thermometers. We used LakeShore 340 as a monitor and stabilizer with PID stabilization loop. The measurements of the temperature over more than a week are shown in figure 2-5, with one thermometer mounted on the stage where the interferometer is placed and the other mounted next to the interferometer crystal to monitor air temperature. Temperatures are shown in degrees of Celsius. The temperature fluctuation is approximately 5 mK.

The vibration isolation from the environment is maintained through three isolation stages. The first stage is built into guide hall. The NIOF is built on its own foundation, separate from the rest of the building and coupled to the guide hall by compliant joints. The second stage (in figure 2-4 shown as (5)) consists of a reinforced concrete slab ($5 \times 3.6 \times 1.11$ meters and about 40000 kg) mounted upon pneumatic air-springs. The system of the slab and springs works as a low-pass filter, removing or reducing high-frequency oscillations. In order to maintain the neutron interferometer at the same position with high precision, the position of the concrete slab is maintained to high precision with a set of pushers and pullers by a computer-controlled servo system. Typical stability in position is 5 μrad for rotation and a few μm for translation. The third stage (in figure 2-4 shown as (7)) is similar to the second vibration isolation stage but scaled down and positioned on top of the second. It is made of a granite table, with mass about 3000 kg, and is mounted on smaller air-springs. Because of the mass and the size difference of the concrete slab and granite table, the frequencies of oscillation is different by an order of magnitude, hence the coupled motion between two resonators is small. The third stage could be a computer-controlled by a servo system too. In our measurements, we did not used the secondary servo system. Vibrations can also come from air pressure gradients. That is why the inner and outer enclosures were designed to reduce acoustic noise. In addition, the inner

enclosure is lined with highly absorbing anechoic foam panels to reduce reverberation times.

As a result of temperature stabilization and vibration isolation, the neutron interferometer facility has exceptional phase stability and fringe visibility.

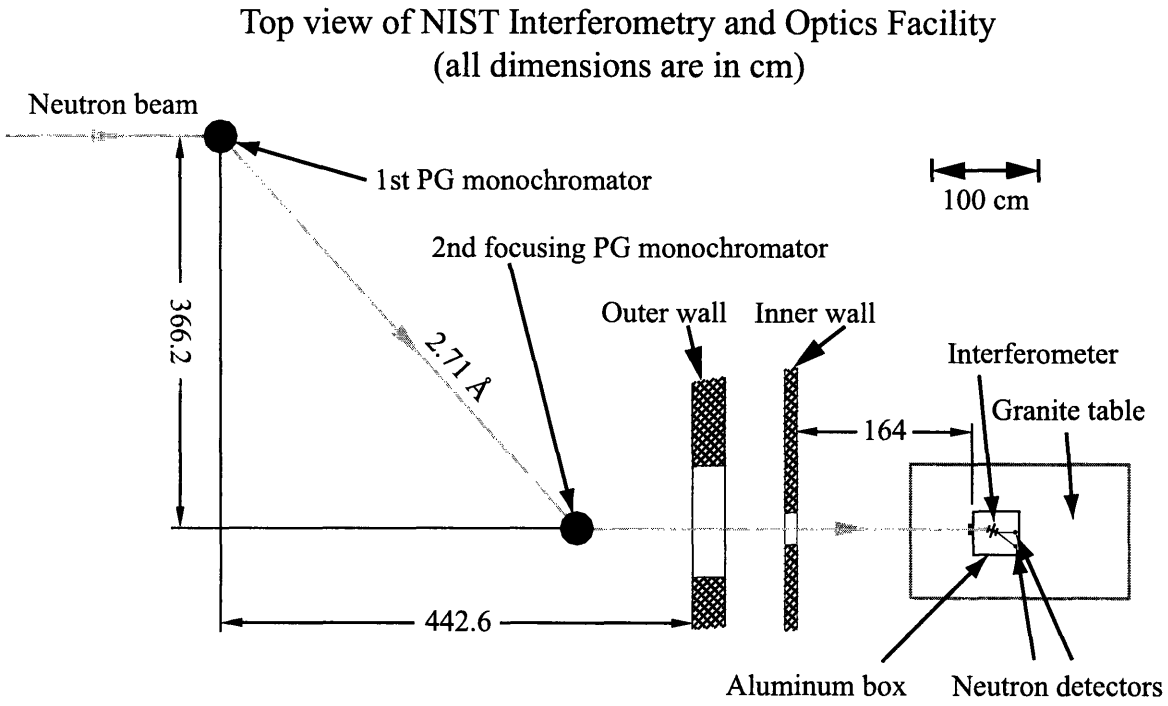

Figure 2-6: Principal diagram of the Neutron Interferometer Setup at NIST.

Figure 2-6 shows the diagram of Neutron Interferometer Setup at NIST with dimensions in cm for a wavelength of $\lambda = 2.71$ Å.

2.1.3 Neutron Detectors

In our experiments, we used three different types of detectors: ^{3}He detectors, a fission chamber, and a position sensitive detector.

^{3}He proportional detectors were located in the O and H beams behind interferometer and were used to take most of the data and for alignment. They are Reuter-Stokes detectors and have cylindrical shape with a 1/2 inch diameter. Thermal neutrons

which hit the detector interact with ^{3}He gas inside:

$$^3_2He + ^1_0n \rightarrow ^3_1H + ^1_1H + 764 \text{ keV}. \tag{2.3}$$

The energy released from the reaction is carried in the kinetic energies of the proton and triton. These atoms ionize the ^{3}He gas while traveling through the detector. Ions are pushed towards the thin anode wire at the center of the detector by an electrostatic potential (in our case 1260 V) and produce a pulse. These detectors have approximately 99% total efficiency. In order to reduce the background, these detectors are kept inside a Cd enclosure with Cd snouts for the neutron beam entrance.

To monitor the incoming neutron beam, we used a fission chamber which has a low 0.1% efficiency and operates at 500 V. This beam is too intense to use a ^{3}He detector. Note that even with double crystal monochromator the neutron interferometer accepts very few neutrons. The interior surfaces of this detector are lined with uranium oxide deposits. Neutrons interact with the ^{235}U isotope in the uranium oxide. The reaction releases 160 MeV of energy in the form of kinetic energies of fission particles, which can be detected due to the ionization of gas inside the detector.

The two dimensional position sensitive detector has about 30% efficiency and combines an in-beam ^{6}Li-ZnS scintillator, microchannel plate (MCP) image intensifier, and a mirror. The mirror reflects the light out of the neutron beam into a charge-coupled device (CCD) camera and the signal from the camera is read out to a computer. Electronic centroiding of images optimized the spatial resolution to 60 μm [29].

2.2 Alignment

In order to obtain the best alignment, we started from the first PG monochromator (neutron entrance to our setup) and continued to align the components of the interferometer setup along the neutron beam path step by step all the way to the neutron detectors (figure 2-6). After the (February 2004) alignment, we increased the

counting rates at the detectors by a factor of 2.5.

As a first step, we aligned the monochromators, neutron interferometer, shielding drums, slits, helium fly tubes and He_3 detectors optically with theodolite. Using marks on the neutron guides and the center mark of the first monochromator crystal we aligned fly tubes , shutter/slit drum, the second monochromator, interferometer crystal, and ^{3}He detectors with theodolite. For some parts of the setup (i.e. fly tubes), it was sufficient to just optically align. For others (i.e. slits, monochromators, and interferometer crystal), it was necessary to perform neutron alignments as well.

The next step was the alignment with neutrons.

2.2.1 1^{st} (PG) monochromator alignment

In order to align the first PG monochromator, we mounted the neutron fission chamber in front of the 2^{nd} focusing monochromator with a 2 cm tall and 0.6 cm wide slit and found the optimal Bragg and tilt angles for the 1^{st} PG monochromator. Figures 2-7 and 2-8 show the results of rotation and tilt scans for determining the optimal orientation of the 1^{st} monochromator.

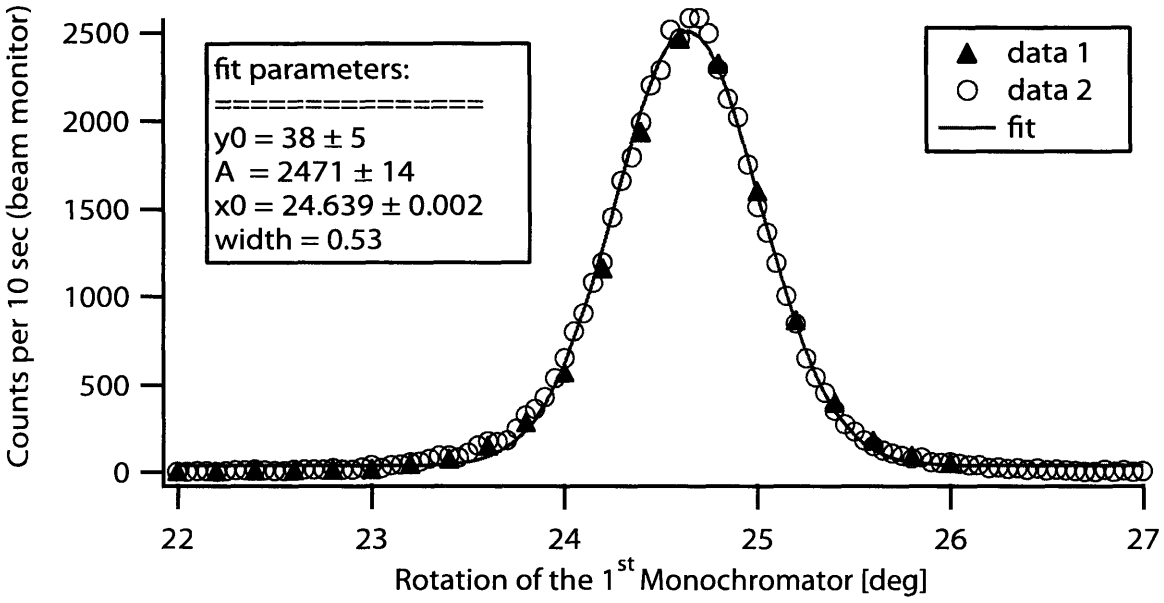

Figure 2-7: Rotation rocking curve of the 1^{st} monochromator.

After we placed the 1^{st} monochromator in the optimal position, we started to

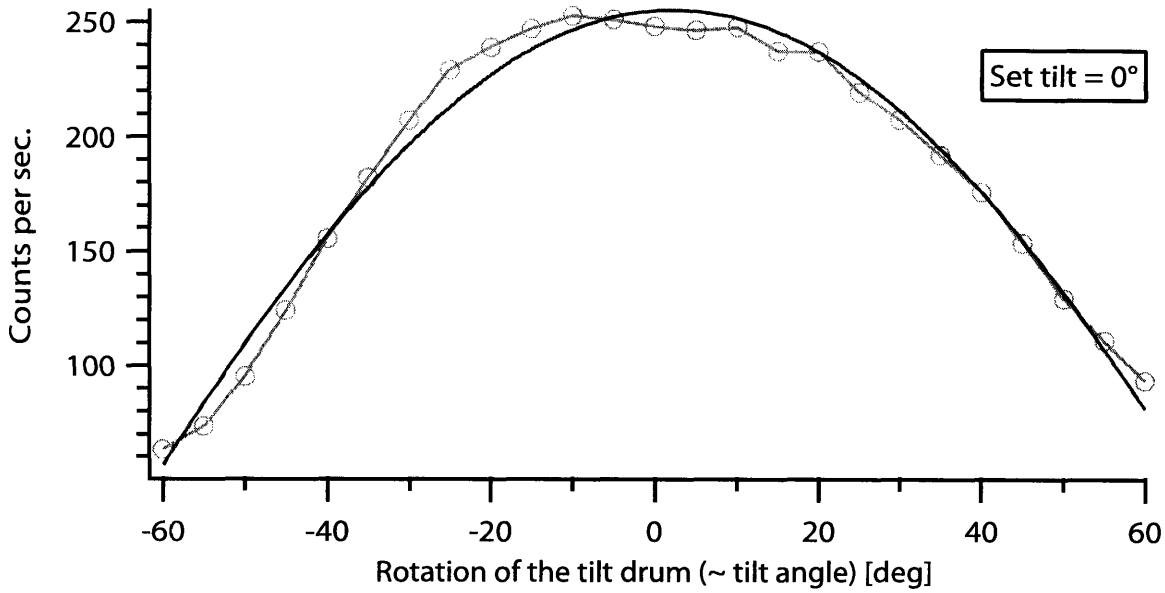

Figure 2-8: Tilt rocking curve of the 1^{st} monochromator.

align the second monochromator.

To make sure that the setup was stable, we checked the alignment of the first monochromator between measurements. Figure 2-9 shows the results of these measurements. On the right axis of the plot, the intensity of the O and H beam detectors are shown for comparison.

To align the first slit, we ran a drum translation scan (shown in figure 2-10) with the drum at the open position. The drum in the close position acted as the beam shutter for the beamline.

2.2.2 2^{nd} focusing (PG) monochromator alignment

The picture of the second monochromator is shown in figure 2-12.

The second monochromator is a focusing monochromator. It consists of 9 PG crystals. In order to align it, we covered all crystals except the middle one with a Cd-shield and repeated procedures similar to those used for aligning the 1^{st} monochromator, except that this time we placed a ^{3}He detector with a 2 mm diameter aperture in front of the interferometer. The results are shown in figures 2-11 and 2-13. From this procedure, we obtained the tilt angle of the middle crystal and the Bragg angle

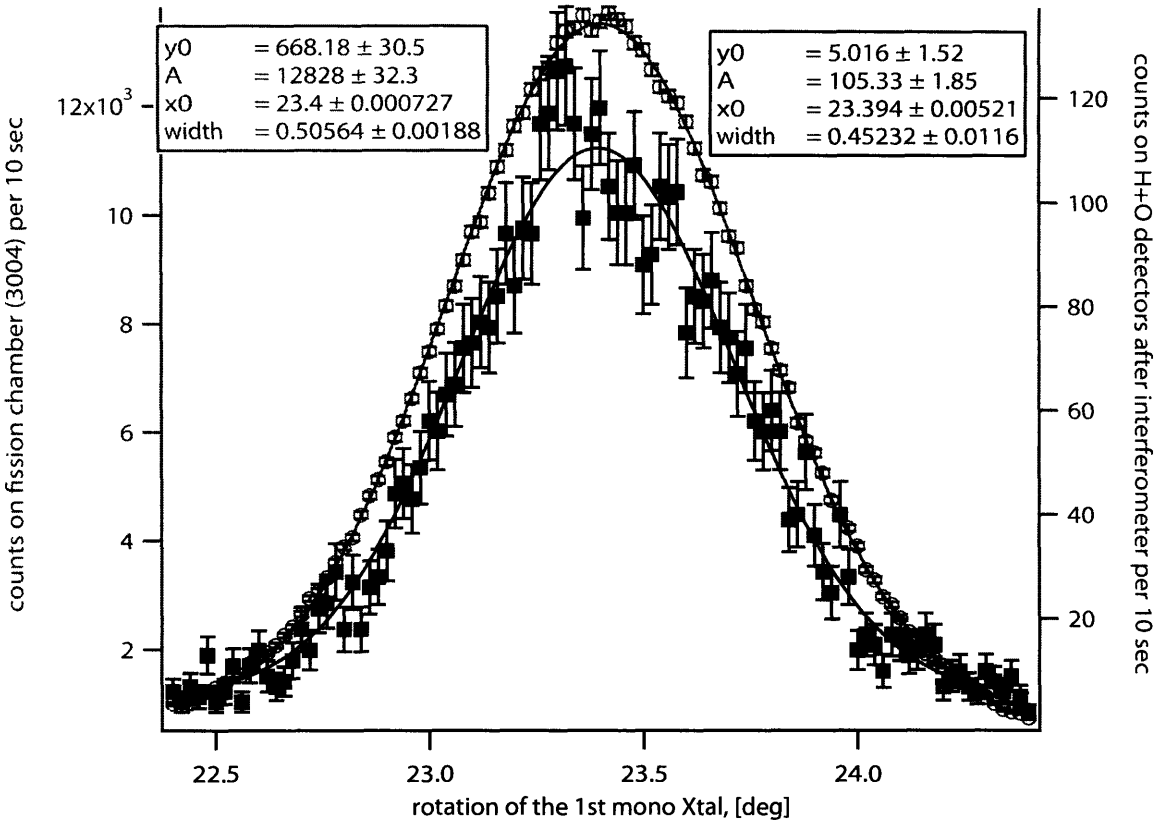

Figure 2-9: Tilt rocking curve of the 1^{st} monochromator.

for all crystals of the 2^{nd} monochromator.

The tilt angles of the remaining crystals were adjusted one by one by shielding every crystal except the one we were aligning and rocking its tilt angle to maximize the detector counting rate. Figure 2-13 shows such scans for the 5 top blades including the middle one in the upper graph and 5 bottom blades including the middle blade in the lower graph. After completing these procedures (figure 2-14), the beam was focused on the first blade of the neutron interferometer (remember that the aperture of the ^{3}He detector was only 2 mm in diameter).

2.2.3 Alignment of the single crystal interferometer

Figure 2-15 shows a picture of several (LLL) perfect crystal interferometers available at NIST. The big crystal in the middle is the one used in our experiments. Each interferometer is a single piece comprised of several prefect crystal blades and a thick

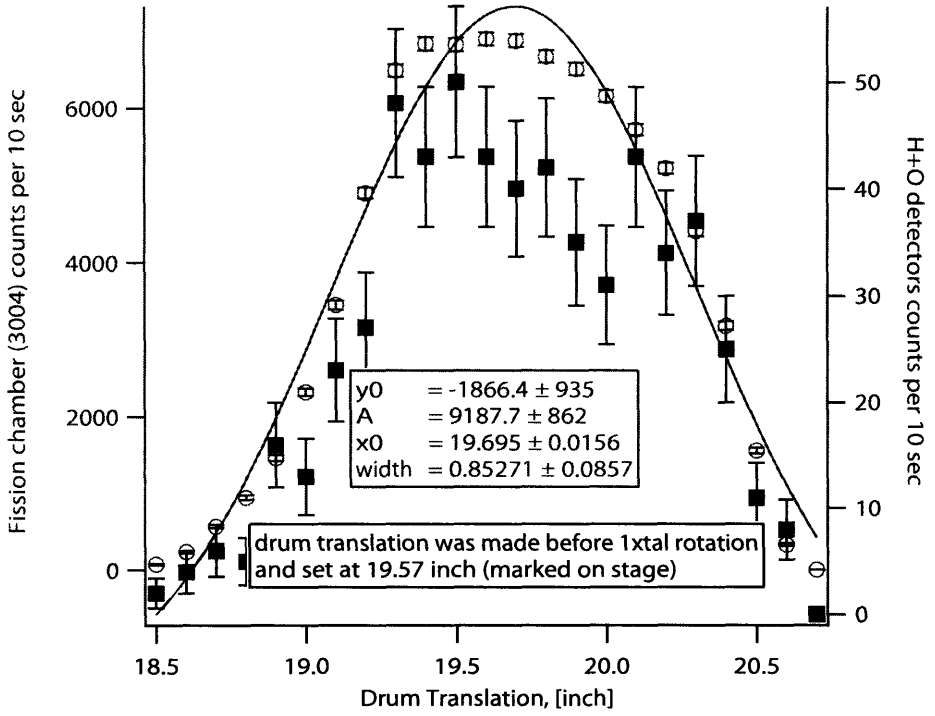

Figure 2-10: Drum translation of the 1^{st} monochromator, which worked as both the beam shutter and the entrance slit.

base machined out of single crystal Si-ingot.

After the beam was focused, we aligned the neutron interferometer crystal. We tightly collimated the beam and put a 12 mm×3 mm slit on the interferometer front crystal. We then set a ^{3}He detector in the direct beam behind of the interferometer crystal and scanned interferometer crystal vertically and horizontally. The results are shown in figures 2-16 and 2-17.

After setting the interferometer in the optimal position, we changed the entrance slit to 2 mm×8 mm and performed a rotation scan (rocking curve) to determine the Bragg angle of the neutron interferometer crystal (see figure 2-18).

After the interferometer crystal was aligned, we could find the best contrast position. Figure 2-19 shows the contrast scan of the empty interferometer. By shifting the interferometer vertically and horizontally, and measuring contrast in each location, we could find the best contrast position. In the case of 2 mm×8 mm slit we were able to achieve 84% contrast.

Figures 2-20 and 2-21 show color plots of contrast and phase shift respectively at

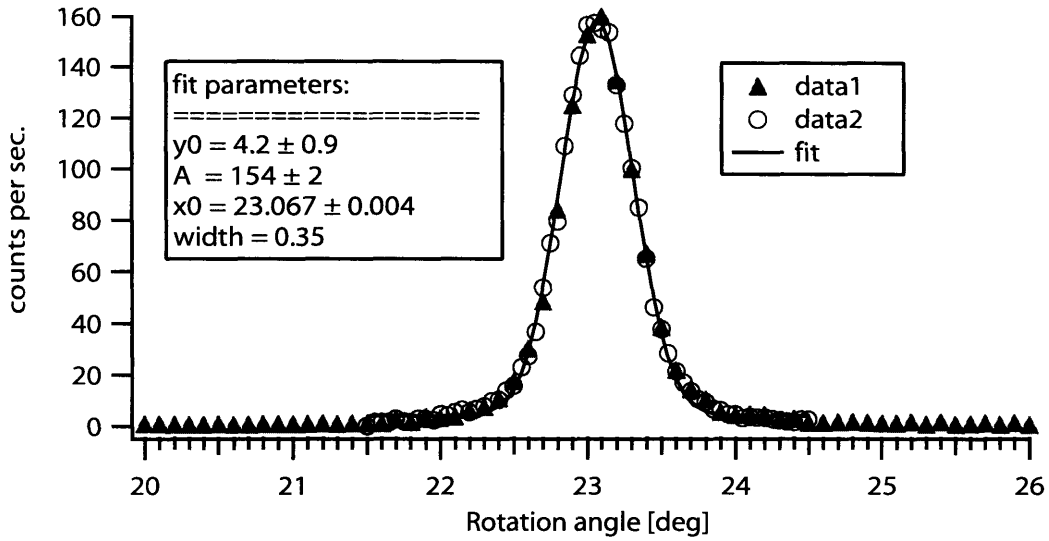

Figure 2-11: Rotation rocking curve of the 2^{nd} monochromator.

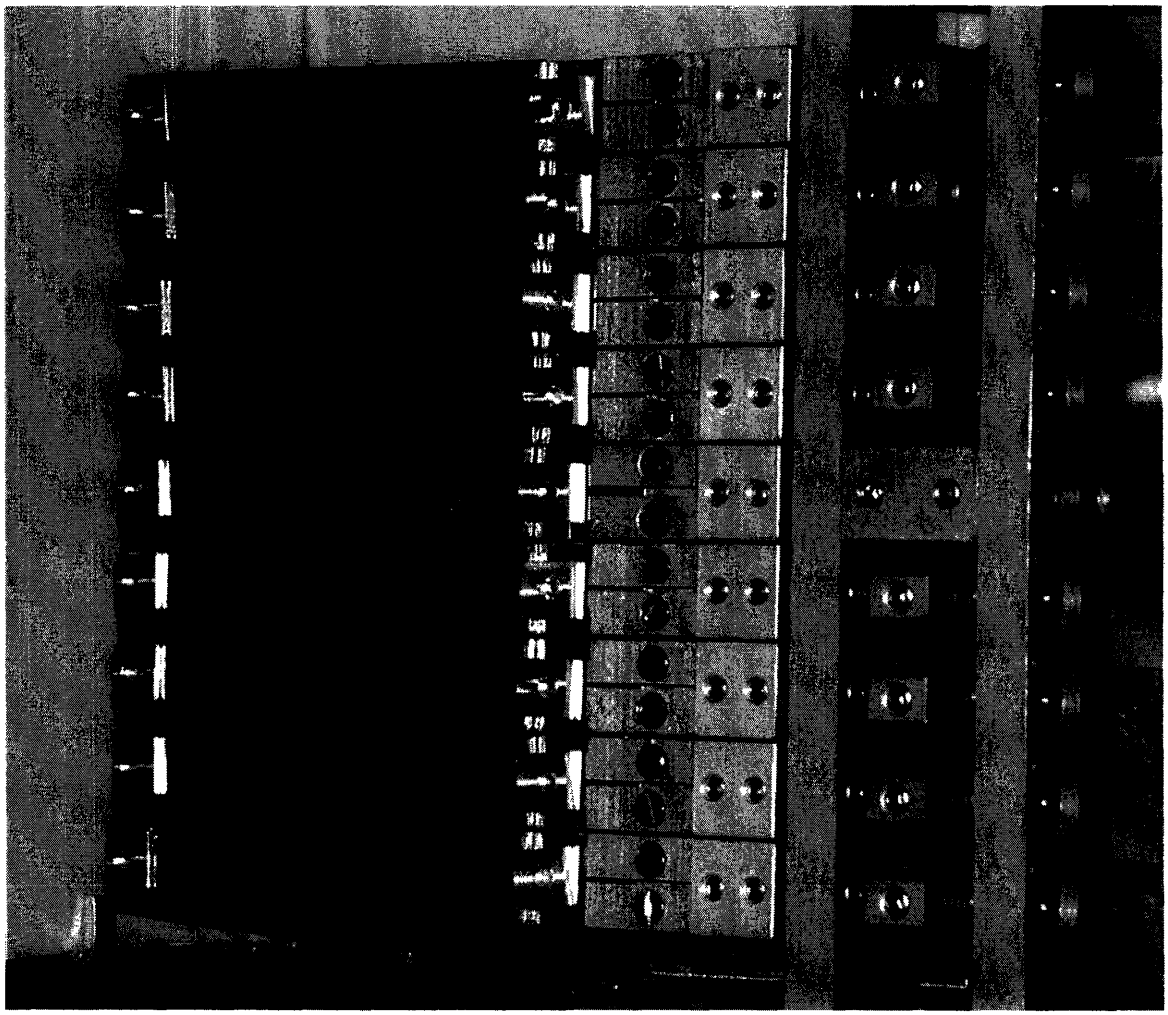

Figure 2-12: Photograph of the second monochromator. It consist of 9 PG blades

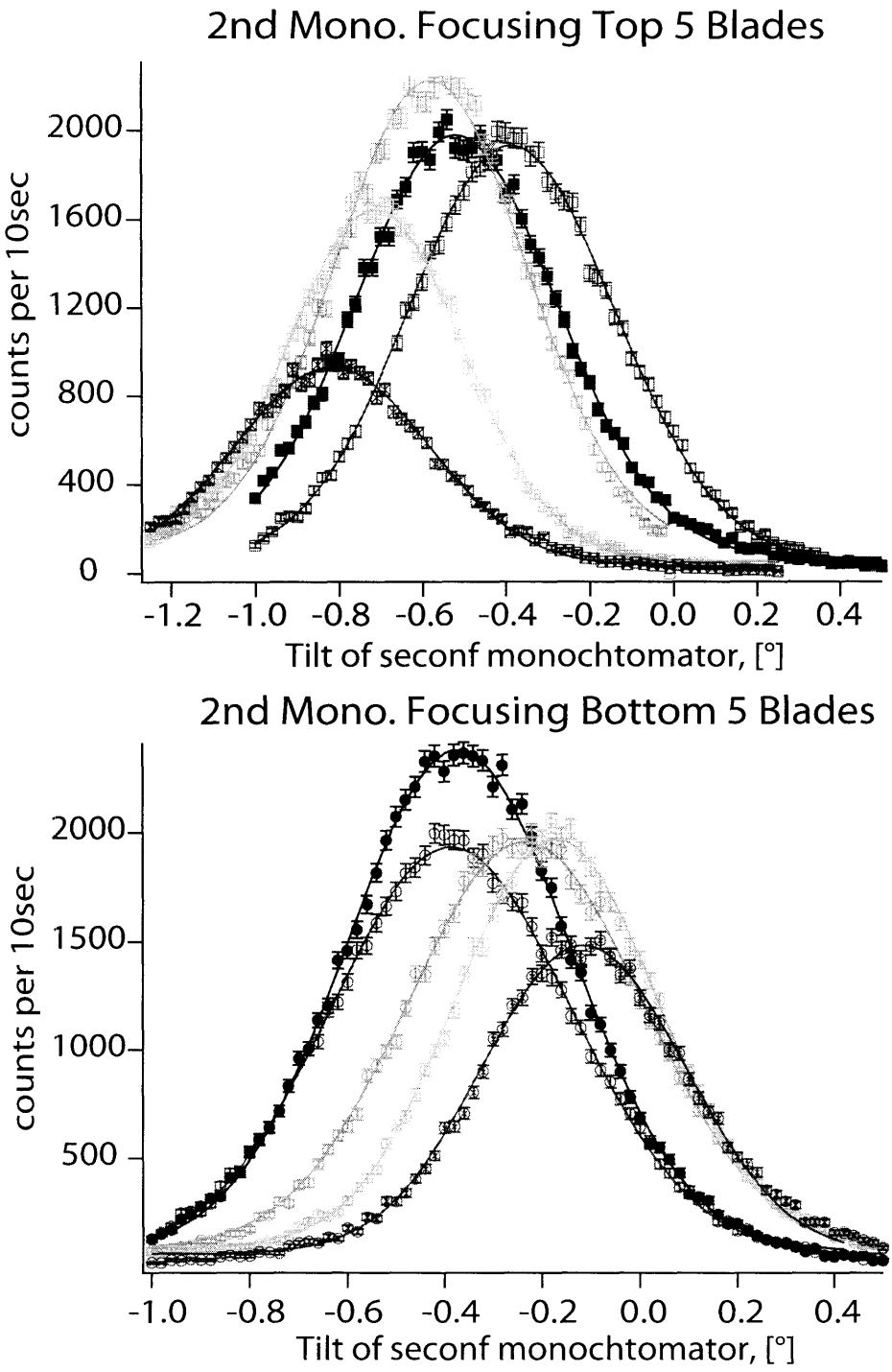

Figure 2-13: Tilt rocking curve of the 2^{nd} monochromator before adjusting.

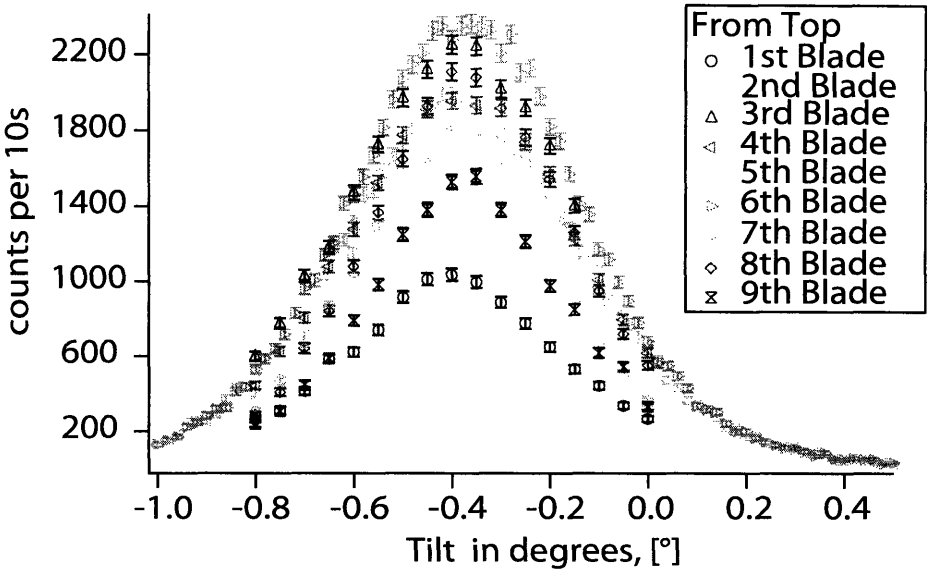

Figure 2-14: Tilt rocking curve of the 2^{nd} monochromator after adjusting the tilt of each blade.

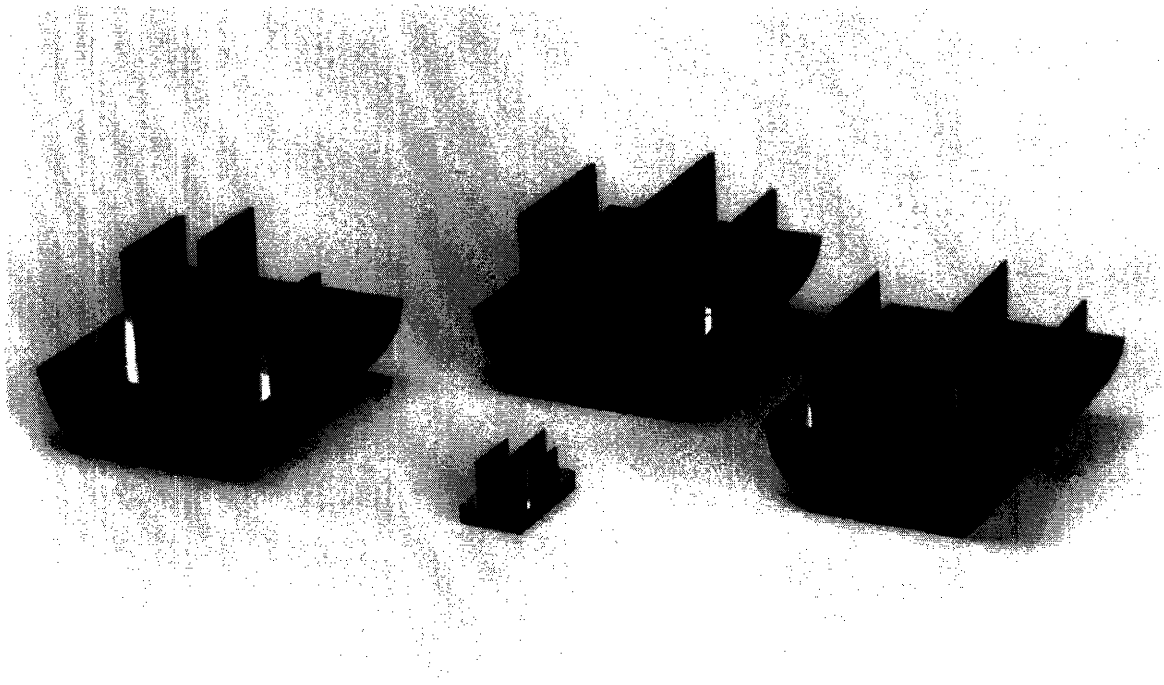

Figure 2-15: Picture of various Laue-Laue-Laue (LLL) perfect crystal interferometers available at NIST (courtesy of D.L. Jacobson).

different interferometer crystal positions. The position of the interferometer crystal was chosen to maximize the contrast.

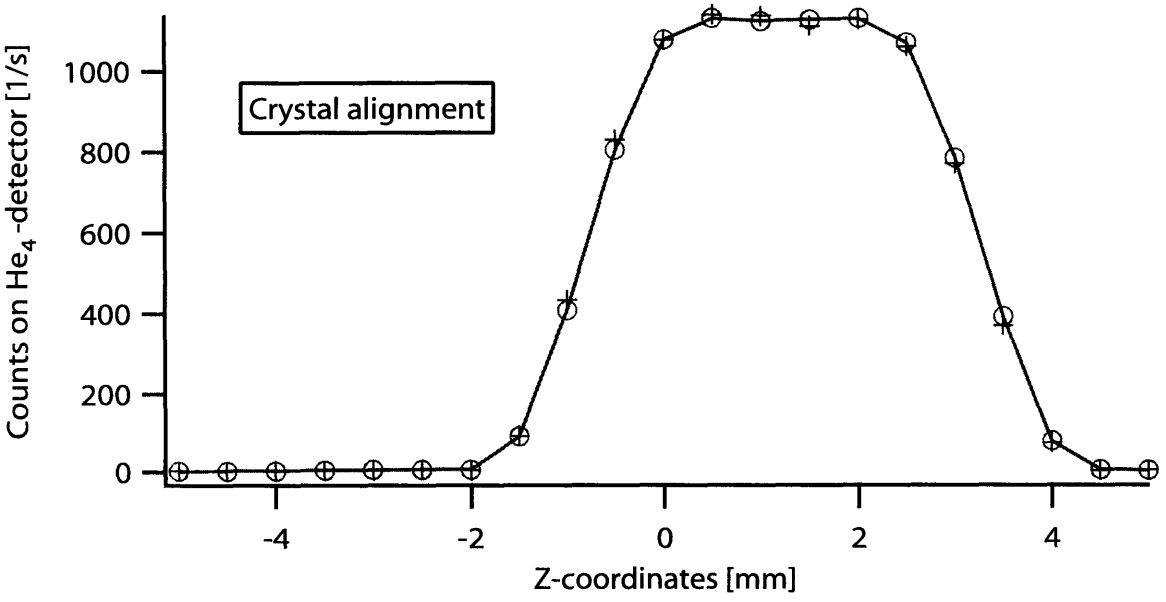

Figure 2-16: Vertical alignment of neutron interferometer crystal.

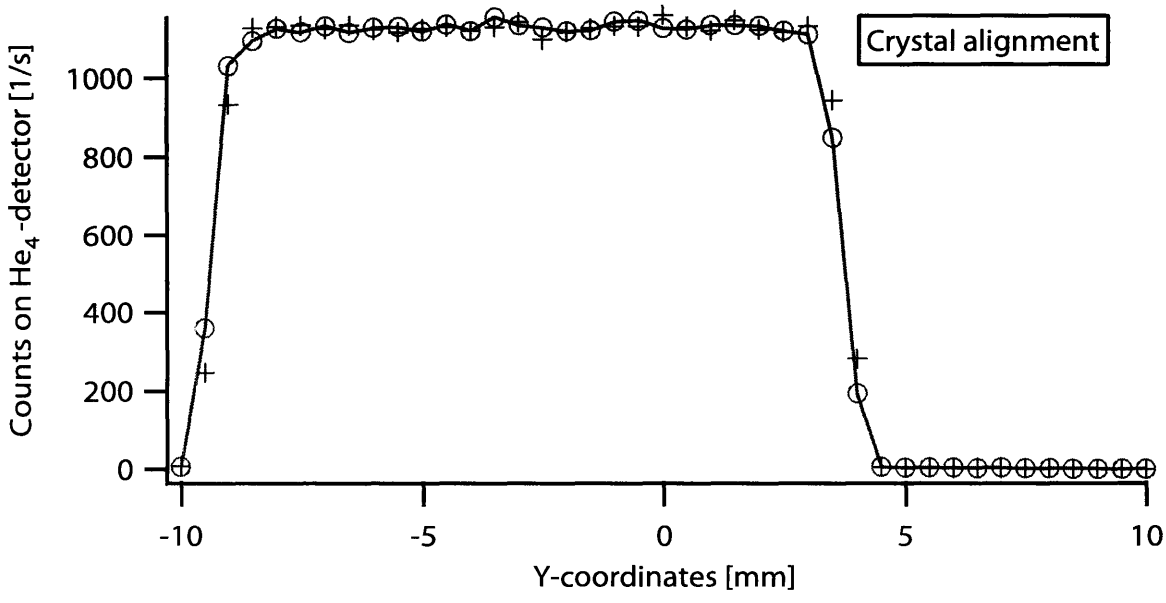

Figure 2-17: Horizontal alignment of Interferometer.

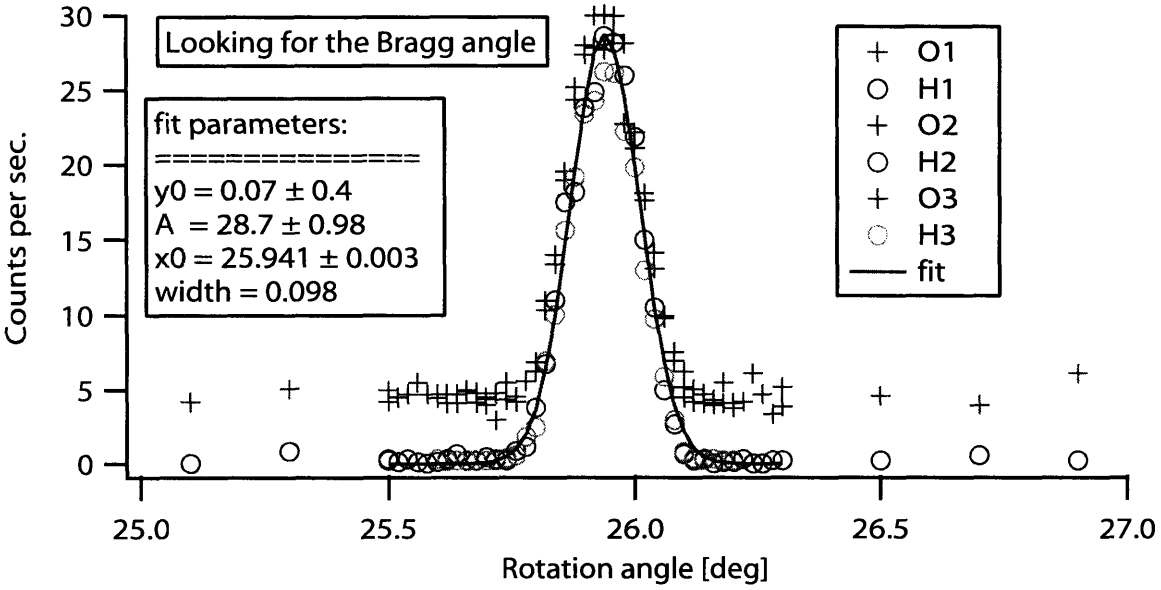

Figure 2-18: Rotation rocking curve of neutron interferometer crystal.

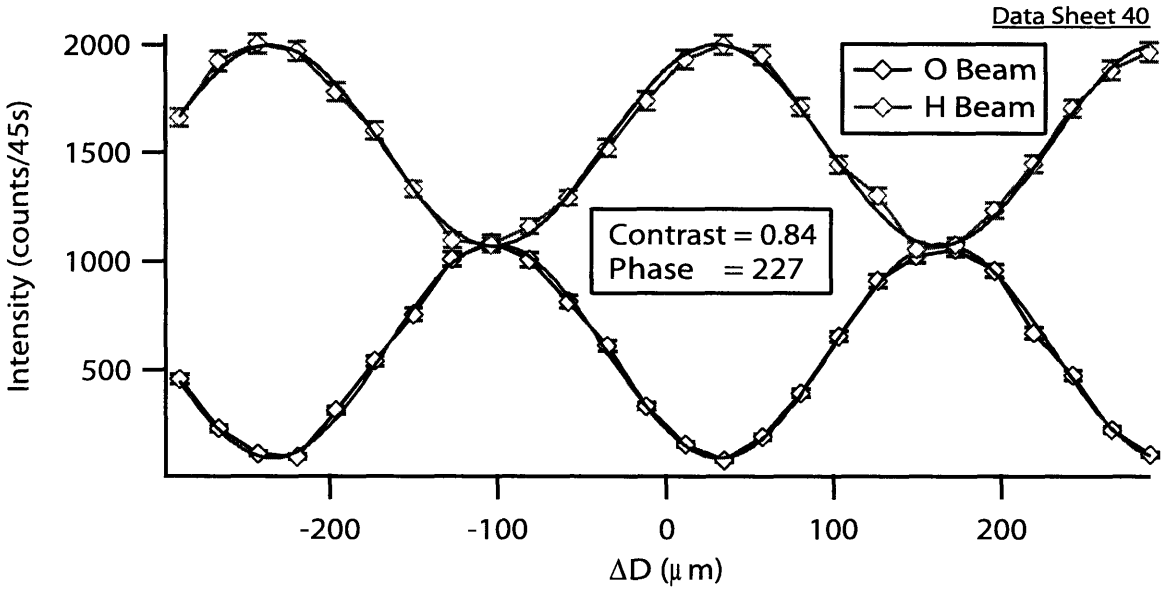

Figure 2-19: The best contrast scan with 2 mm×8 mm slit.

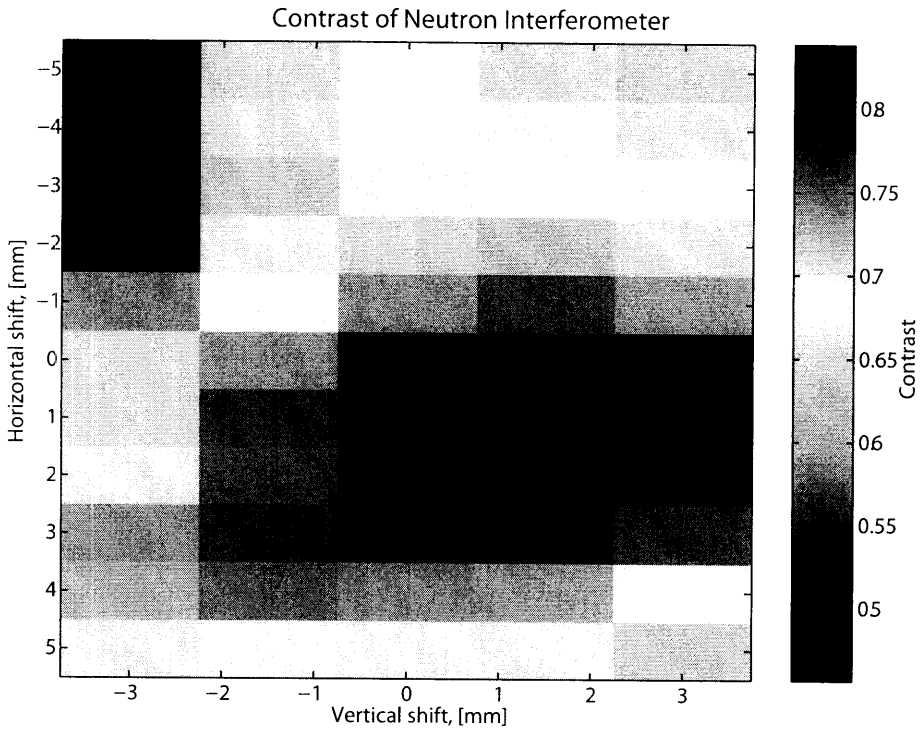

Figure 2-20: Contrast of the neutron interferometer with 2 mm×8 mm slit at different positions with respect to the neutron beam.

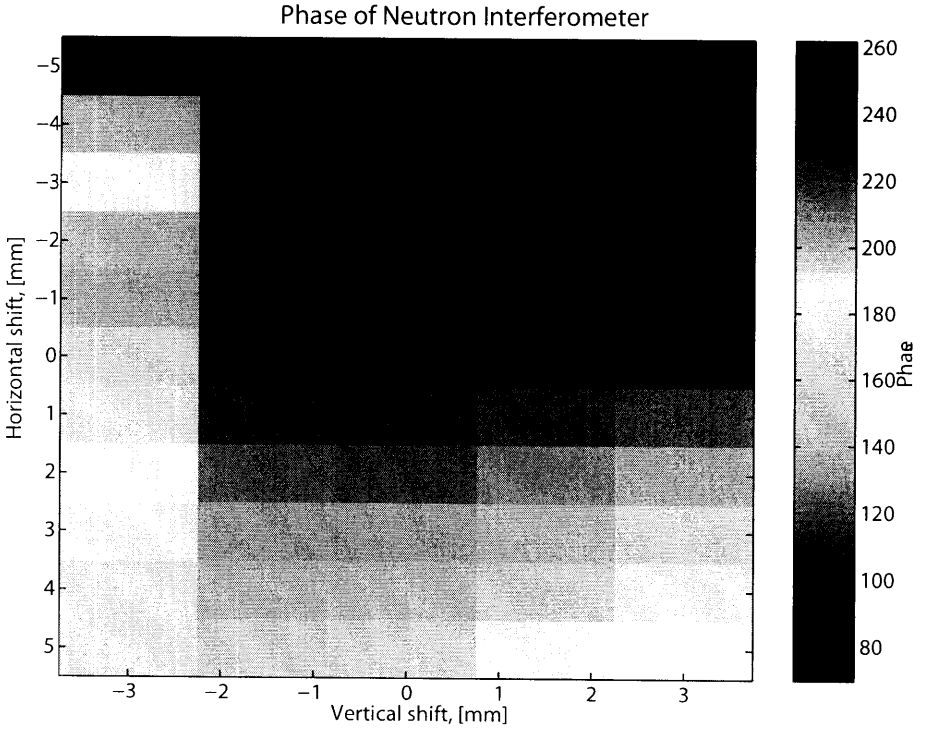

Figure 2-21: Phase changes of the neutron interferometer with $2mm \times 8mm$ slit at different positions with respect to the neutron beam.

Next, the single crystal neutron interferometer was aligned and we were ready to proceed with measurements.

2.3 Wavelength measurements

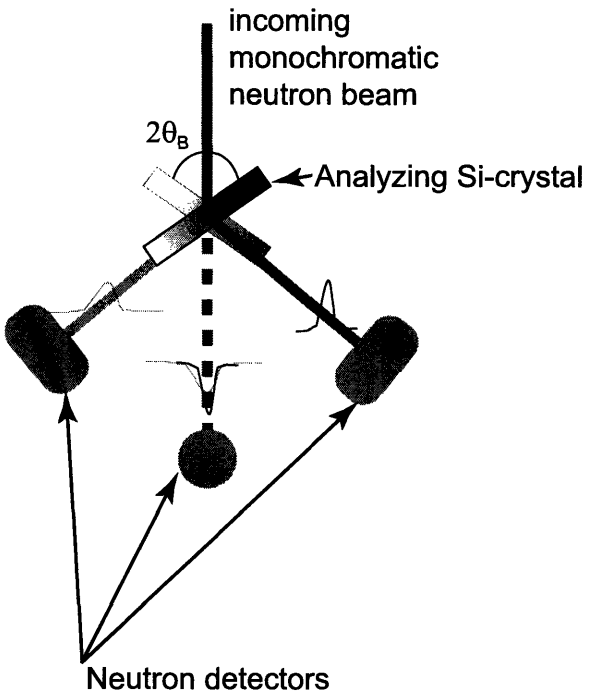

Figure 2-22: A schematic diagram for a wave-length measurement. Difference in the peak angles for parallel and anti-parallel scans gives us $2\theta_{Bragg}$.

The final piece of information we needed before we could start measuring was the neutron wavelength. This measurement verifies the alignment was correct.

Figure 2-22 shows a schematic diagram of the wave-length measurement setup. We used a pressed Si crystal to determine the wavelength of our neutron beam. The measurement was done by rotating the crystal through parallel and anti-parallel Bragg reflections and selecting the angles of the maximum (minimum) peak intensity on the ^{3}He integrated area detector placed in $\pm 2\theta_{Bragg}$ (direct) beam positions. Figure 2-23 shows typical parallel and anti-parallel rocking curves at a fixed tile angle. The difference in this two determined angles would be exactly $2\theta_{Bragg}$ if the axis of the Si crystal rotation was exactly perpendicular to the incoming neutron beam. That

was why we repeated the same measurements for different tilt angles of the analyzing crystal. Finding the Bragg angle, θ_{Bragg}, and using the Bragg's law

$$\lambda = 2d \sin \theta_{Bragg}, \tag{2.4}$$

we could determine the wavelength of the incoming neutrons.

Figure 2-24 shows a plot of the wavelength versus tilt angle of the analyzing crystal. The minimum on this plot corresponds to the correct tilt, thus the correct wavelength.

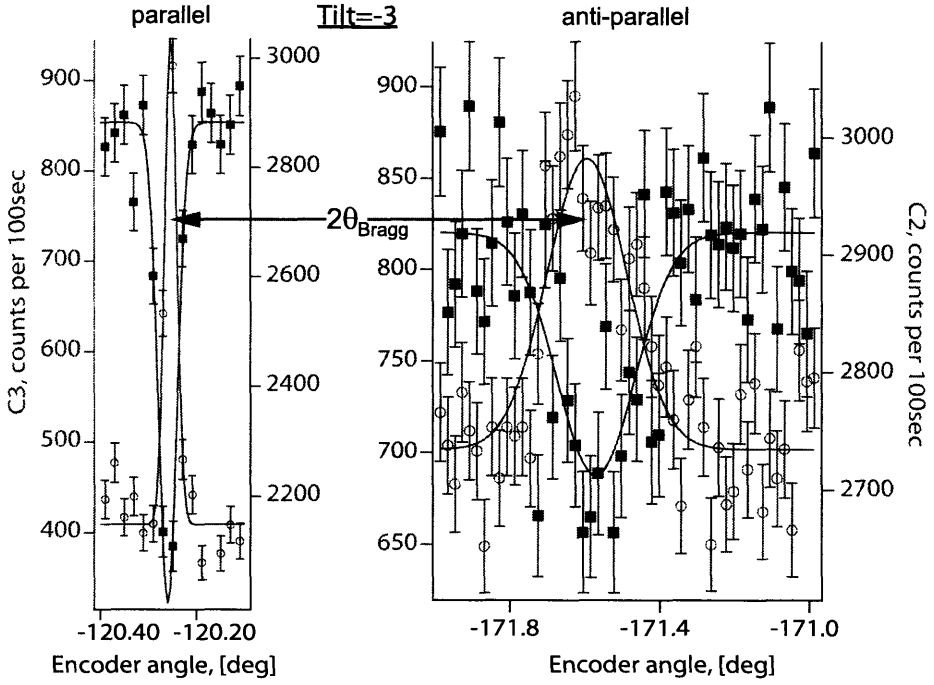

Figure 2-23: Typical set of rocking curves for the analyzer crystal at the fixed tilt angle (Tilt=-3°). The difference in the peak angles for parallel and anti-parallel scans gives us $2\theta_{Bragg}$.

We measured the wavelength of the neutrons in two different places. Figures 2-23 and 2-24 shows wavelength measurements in front of the interferometer and figure 2-25 shows wavelength measurements right after second blade of the neutron interferometer.

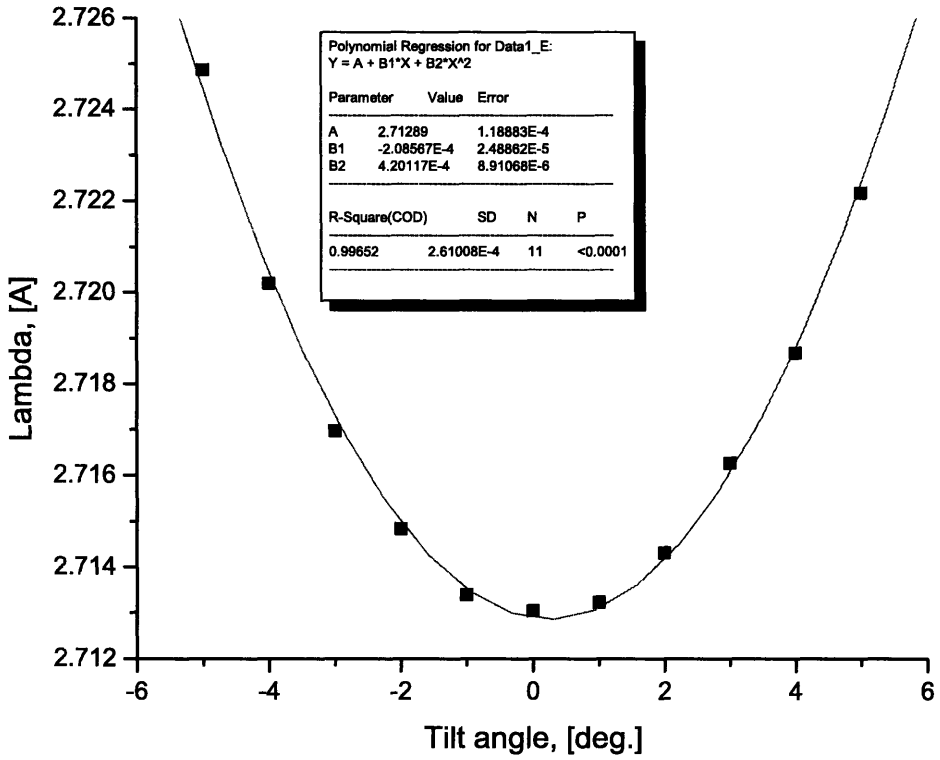

Figure 2-24: The wave length dependence on the tilt of the analyzer crystal. The minimum of this curve determines the proper tilt angle, and thus the wavelength. These measurements were taken in front of the neutron interferometer.

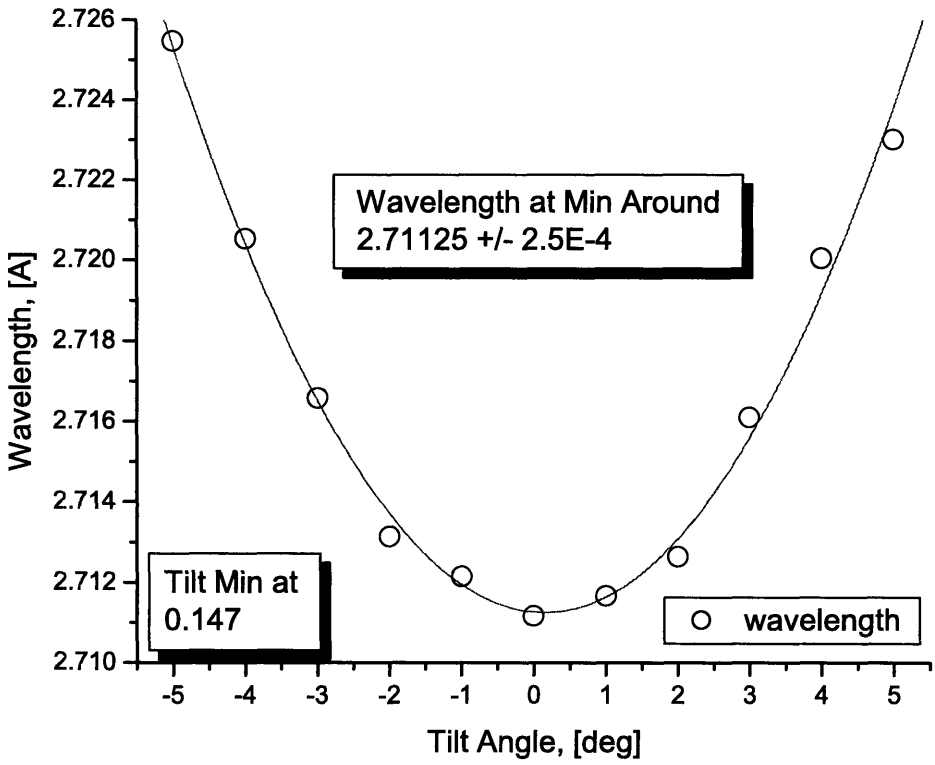

Figure 2-25: The wavelength dependence on the tilt of the analyzer crystal placed after the neutron interferometer. The minimum of this curve determines the proper tilt angle, and thus the wavelength.

Chapter 3

Reciprocal Space Neutron Imaging

3.1 Introduction

Here we introduce a Fourier based method for phase contrast neutron imaging, report its experimental implementation, show results for a 1-D test phantom, and outline the reconstruction methodology. This new approach makes use of neutron interferometry to achieve both phase contrast and to spatially code the phase of the neutron with a linear phase grating. The spatial information is recovered from the coherent interference of this phase grating and a spatial phase distribution due to the sample. By moving neutron imaging from real to reciprocal space (in analogy to Fourier magnetic resonance imaging [30]) we avoid the need for position sensitive detectors and improve the potential image resolution. The ultimate resolution will depend solely on the beam characteristics: intensity, momentum spread, and divergence.

3.2 Neutron Imaging

Neutron imaging [31, 32, 33] is complementary to other non-invasive imaging methods, such as X-ray imaging and Magnetic Resonance Imaging [34]. Neutrons are transparent to high Z-number materials, thus allowing tomographic study of properties in 3-D. Neutrons are scattered by light elements, primarily hydrogen atoms. Therefore one can, for example, study density fluctuation due to inhomogeneities in-

troduced by hydrogen in metals, density of polymeric overlayers, formation of water in hydrogen fuel cells and crystallography for structural biology. Another important advantage of neutron imaging is its sensitivity to magnetic domains, which allows the study phase tomography of the magnetic domain distribution in a sample. One of the primary challenges of neutron imaging is to achieve high spatial resolution while maintaining high contrast. This has not been achieved so far because of the typically low flux of a neutron beam and the poor resolution of available 2-D neutron detectors. The neutron interferometry technique may be used to develop high contrast imaging based on phase differences induced by a sample inside the interferometer [35]. However, real space neutron-interferometric imaging is spatially incoherent and still requires the use of position sensitive detectors to spatially resolve the imaged elements [31, 32, 33, 35, 36]. Here we show that a neutron interferometer can be used as a reciprocal space, spatially coherent imaging device to improve image resolution while maintaining high contrast. In these studies the detector integrates over the entire beam. The spatial distribution of the neutron scattering function for a sample placed in path I of the interferometer is created internally in the interferometer via comparison to a phase gradient placed in path II of the interferometer (Figure 3-1). This method does not require a 2-D detector and thus has the potential to significantly improve the spatial resolution compared to the current limit of tens of micrometers [37].

3.3 Reciprocal Space Neutron Imaging

Here we describe the additional step of imposing a linear phase ramp on the neutron wave-function to enable reciprocal space imaging. The imaging method is shown schematically in figure 3-1. Here a well-collimated and monochromatic neutron beam of finite spatial extent enters the perfect-crystal interferometer. At the first blade the neutrons are Bragg scattered and split into two paths. The neutron wave-function is $|path, \mathbf{p}\rangle$, where a neutron with momentum $\mathbf{p}$ can choose *path I* or *path II* (figure 3-1). The phase which the neutron accumulates over each path are experimentally

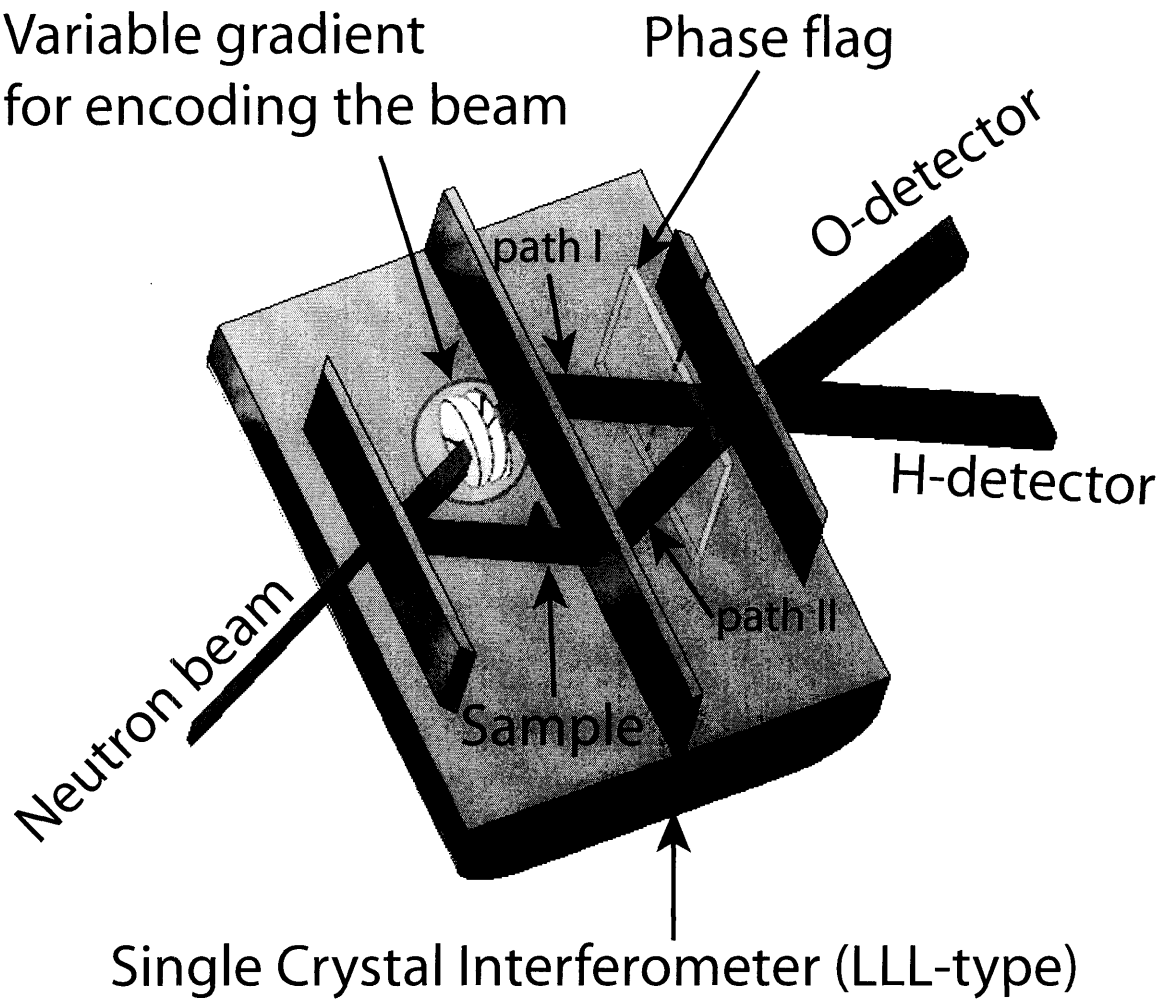

Figure 3-1: Schematic diagram of the imaging experiment at NIST. A neutron beam, coming from the left, is coherently divided via Bragg diffraction in the first blade of the neutron interferometer, into two beams. These beams travel along paths I and II. The phases which the neutron accumulates over each path are experimentally controlled by rotating the phase flag, which changes the optical path length due to the flag. After diffraction at the second blade, these beams are coherently recombined at the third blade and proceed to the O- or H- detector.

controlled via phase flag rotation (figure 3-1).

The sample is placed in *path II* and introduces a spatially dependent phase shift ($\phi_s(\mathbf{r})$) into the wave-function, $\Psi = e^{i\phi_1} C_1 \left| path\ I, \mathbf{p} \right\rangle + e^{i\phi_s(\mathbf{r})} e^{i\phi_2} C_2 \left| path\ II, \mathbf{p} \right\rangle$, where ϕ_1 and ϕ_2 are respectively the phases neutrons pick up by traveling through *path I* and *path II* without the sample. The coefficients C_1 and C_2 are parameters of the neutron interferometer which account for attenuation and scattering losses of the

neutron beam.

The sample-dependent phase shift ($\phi_s(\mathbf{r})$) forms the basis for phase contrast imaging [31, 32, 35, 36]. In previously reported work [38, 35] this phase shift would be converted into an observable variation in beam intensity when the two beams are recombined at the third blade of the interferometer. The O- and H-beams leaving the interferometer would then have a spatially dependent intensity that could be recorded with a position sensitive detector in the O-beam,

$$I_O(\mathbf{r}, \phi_0) = \frac{1}{2}\left(C_1^2 + C_2^2\right) + C_1 C_2 \cos\left(\phi_s(\mathbf{r}) + \phi_0\right), \tag{3.1}$$

where the coordinate $\mathbf{r}$ lies in a plane transverse to the beam, $\phi_s(\mathbf{r})$ is the sample phase function, and $\phi_0 = \phi_2 - \phi_1$.

To accomplish reciprocal space neutron imaging, we add a variable pitch wedge to the upper path (*path I*) of the interferometer (figure 3-1). This wedge ($\mathbf{k}$) introduces an additional position dependent phase ($\mathbf{k} \cdot \mathbf{r}$) into the neutron wave-function,

$$\Psi = e^{-i\mathbf{k}\cdot\mathbf{r}} e^{i\phi_1} C_1 \left|path\ I, \mathbf{p}\right\rangle + e^{i\phi_s(\mathbf{r})} e^{i\phi_2} C_2 \left|path\ II, \mathbf{p}\right\rangle. \tag{3.2}$$

This is conveniently rewritten in terms of the wave-number of the neutron phase, $\mathbf{k}$,

$$I_O(\mathbf{k}, \phi_0) = \int \left((C_1^2 + C_2^2)/2 + C_1 C_2 \cos\left(\mathbf{k} \cdot \mathbf{r} + \phi_s(\mathbf{r}) + \phi_0\right) \right) d\mathbf{r}. \tag{3.3}$$

Notice that with this reciprocal space measurement approach we do not use a position sensitive detector, instead a much more sensitive ^3He whole-beam integrating detector is used and the O- and H-beam intensities are recorded as a function of the wave-number, $\mathbf{k}$ (pitch of the wedge).

3.4 Experiment

Prior to describing the image reconstruction analysis we will describe the actual experimental implementation and our preliminary results.

3.4.1 Imaging Setup

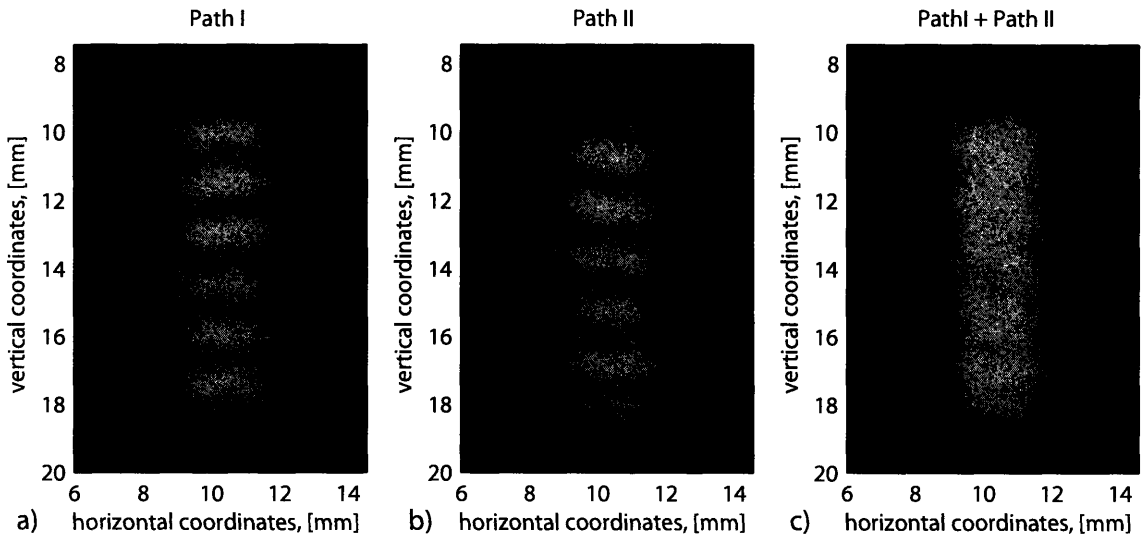

Figure 3-2: Phase image on the position sensitive detector placed in the O-beam. Here is the fused silica wedge with 3°-wedge angle is placed in path I a) or path II b). c) is the sum of path I and path II.

The measurements were made at the Neutron Interferometer and Optical Facility at the National Institute of Standarts and Technology [28]. It consists of a perfect Si-crystal neutron interferometer shown in figure 3-1 with high phase contrast (> 80%) and a long-term phase stability produced by temperature stabilization of the interferometer enclosure (< 5 mK). The existing interferometer was machined from a silicon single crystal ingot and operates on a cold neutron beam ($E = 11.1$ meV, $\lambda = 0.271$ nm, $\Delta\lambda/\lambda \leq 0.5\%$). A detailed description of the facility can be found in previous chapters and Ref. [39, 16].

3.4.2 Implementation of the Phase Gradient

The phase gradient was produced by a system of two identical fused silica wedges with a 6° wedge angle in the configuration as shown in figures 3-1 and 3-3. By arranging the two wedges in this stacked configuration and by counter rotating them, we impose a linear phase ramp along only the z-direction. Each wedge is positioned perpendicular to the beam and produces gradients: $\mathbf{k_{1,2}} = \mathbf{z}k_0 cos\alpha_{1,2} + \mathbf{y}k_0 sin\alpha_{1,2}$, where k_0 is the

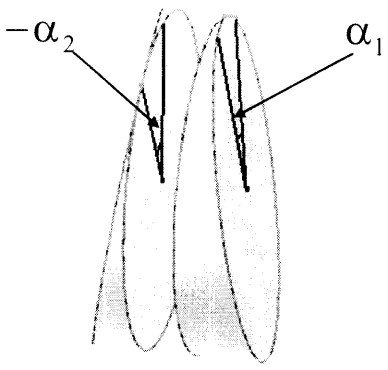

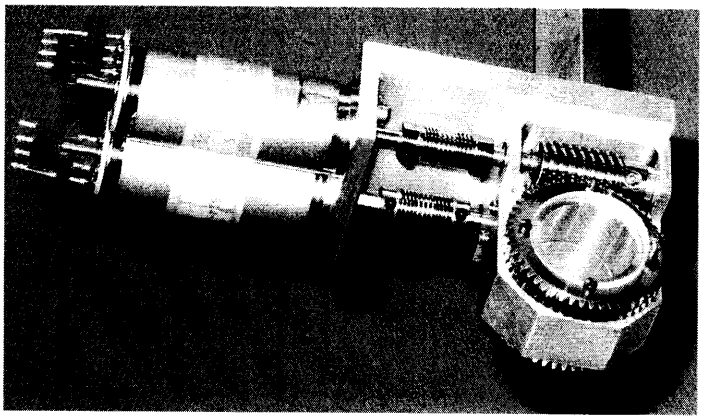

$$q \propto \theta \propto \theta_{max}\left[\cos(\alpha_1)+\cos(\alpha_2)\right]$$

$$\alpha_1 = -\alpha_2 = \alpha \longrightarrow q \propto 2\theta_{max}\cos(\alpha)$$

Figure 3-3: Each wedge is positioned perpendicular to the beam and produces gradients: $\mathbf{k_{1,2}} = \mathbf{z}k_0 cos\alpha_{1,2} + \mathbf{y}k_0 sin\alpha_{1,2}$, where k_0 is the maximal gradient which each wedge can produce in the vertical direction and α_1, α_2 are the angles of rotation of the wedge around the neutron beam path. To create only vertical gradients we counter-rotate these two wedges: $\mathbf{k_{tot}} = \mathbf{k_1} + \mathbf{k_2} = 2\mathbf{z}k_0 cos\alpha$ ($\alpha_1 = -\alpha_2 = \alpha$), so the realizable vertical gradients vary from $-2k_0$ to $2k_0$.

maximal gradient which each wedge can produce in the vertical direction and α_1, α_2 are the angles of rotation of the wedge around the neutron beam path. To create only vertical gradients we counter-rotate these two wedges: $\mathbf{k_{tot}} = \mathbf{k_1} + \mathbf{k_2} = 2\mathbf{z}k_0 cos\alpha$ ($\alpha_1 = -\alpha_2 = \alpha$), so the realizable vertical gradients vary from $-2k_0$ to $2k_0$.

For the two 6° wedges, the maximum phase gradient is $2 \cdot 10^4$ rad·m^{-1}. When the phase gradient is set to zero there is a spatially uniform length of 6.4 mm of fused silica which corresponds to a uniform phase offset of 11 rad. We verified that the phase gradient was properly created by recording the spatial variation of the contrast with a position sensitive detector in the absence of a sample. Figure 3-4 shows on the left the combination of two used wedges to create (next right) corresponding phase wedge, thus phase gradient and on the right is show image from position sensitive detector [29]. Here we show 3 different combination (from top to bottom) of the wedges' rotations and 3 different images for different phase gradients.

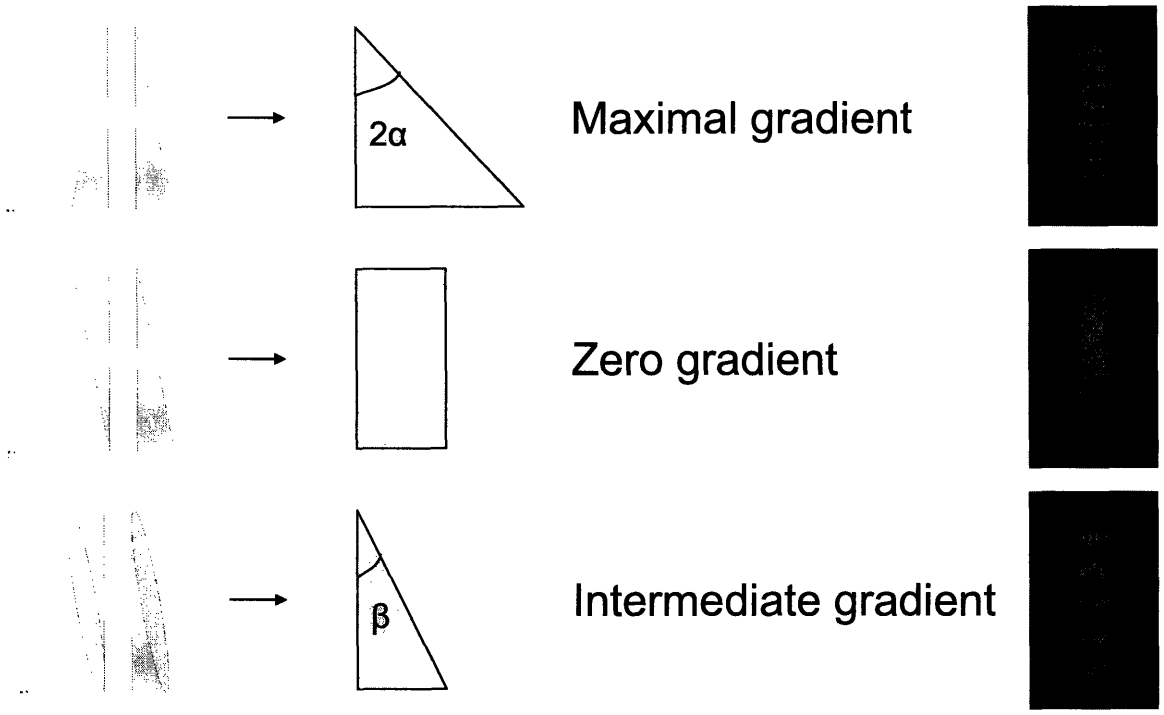

Figure 3-4: The figure shows the wedges used to create phase grating across the neutron beam and the corresponding images from a position sensitive detector [29]. Each wedge is positioned perpendicular to the beam.

In the experiments described below, the phase gradient was created by a fused silica wedge, placed in the path I of the neutron interferometer (Figure 3-1). Figure 3-2a) shows the image obtained by placing one of these wedges in the path I. Here the position sensitive detector is placed in the O-beam, the wedge is oriented to produce a vertical phase gradient and there is no sample. The initial beam is 8 mm tall and 2 mm wide. When the beam arrives at the detector it has an horizontal divergence, due to dynamical diffraction, and a small vertical divergence. The wedge produces a vertical periodic intensity modulation resulting from interference of path I and path II, and the modulation is then recorded by the position sensitive detector. From the period of the modulation we can extract the magnitude of the phase wave-number q. Intensity oscillations do not disappear when the wedge is moved from path I to path II (Figure 3-2b)). We check that coherence is not lost by refocusing the phase gradient by a second wedge (Figure 3-2c)).

3.4.3 Empty Interferometer Data

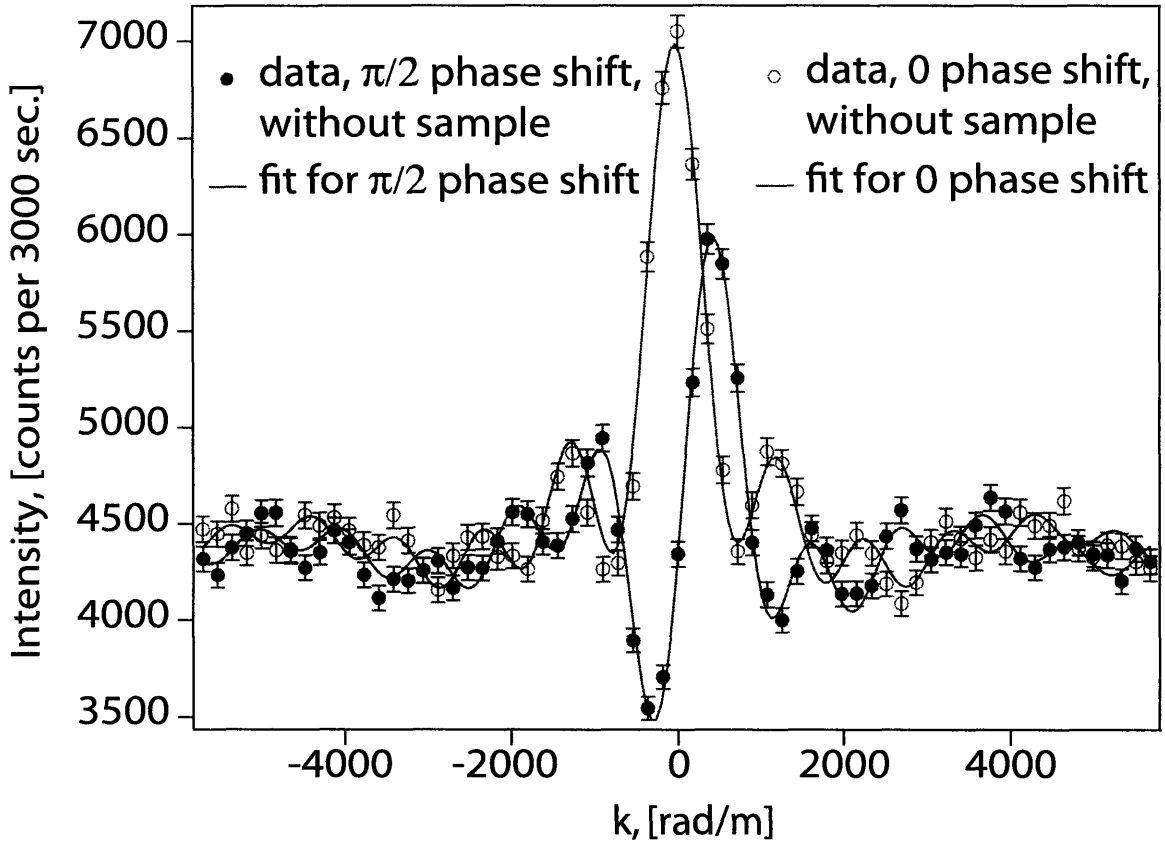

Figure 3-5: The spatial extent and uniformity of the beam influence the image quality. We characterize the beam by recording the O-detector intensity for the empty (no sample) interferometer. The intensity scan was recorded where the phase gradient was ramped by counter-rotating the fused silica wedges. Here open (red) circles and closed circles (blue) correspond to a $\pi/2$ phase difference. The lines are fits to the data assuming a uniform beam and the only fit-parameters are the height of the beam and the phase.

A further test of the experimental setup is shown in figure 3-5 where we report the k-dependence of the integrated contrast for the interferometer in the absence of a sample. The plot reports the integrated O-beam intensity for an effective phase difference of 0 and $\pi/2$ in the two paths. The variation in intensity results from the finite spatial extent of the beam and any intensity fluctuations across the beam. For this measurement we employed a well-collimated, rectangular beam (2 mm$\times$8 mm) which should ideally result in an integrated intensity proportional to a $1 + sinc$ function. The smooth curve is the best fit to a *sinc* function. The excellent quality of the

data shows the quality of the beam characteristics (profile, momentum spread and divergence). We fit the data to a $1 + sinc$ function assuming a uniform beam, the fit parameters were a height of 7.90 mm±0.05 mm, phase of -0.21 rad±0.09 rad for the data with "0" phase shift (red curve), and phase of 1.31 rad±0.12 rad for the data with "$\pi/2$" phase shift (blue curve).

3.4.4 Wedge as a Sample Data

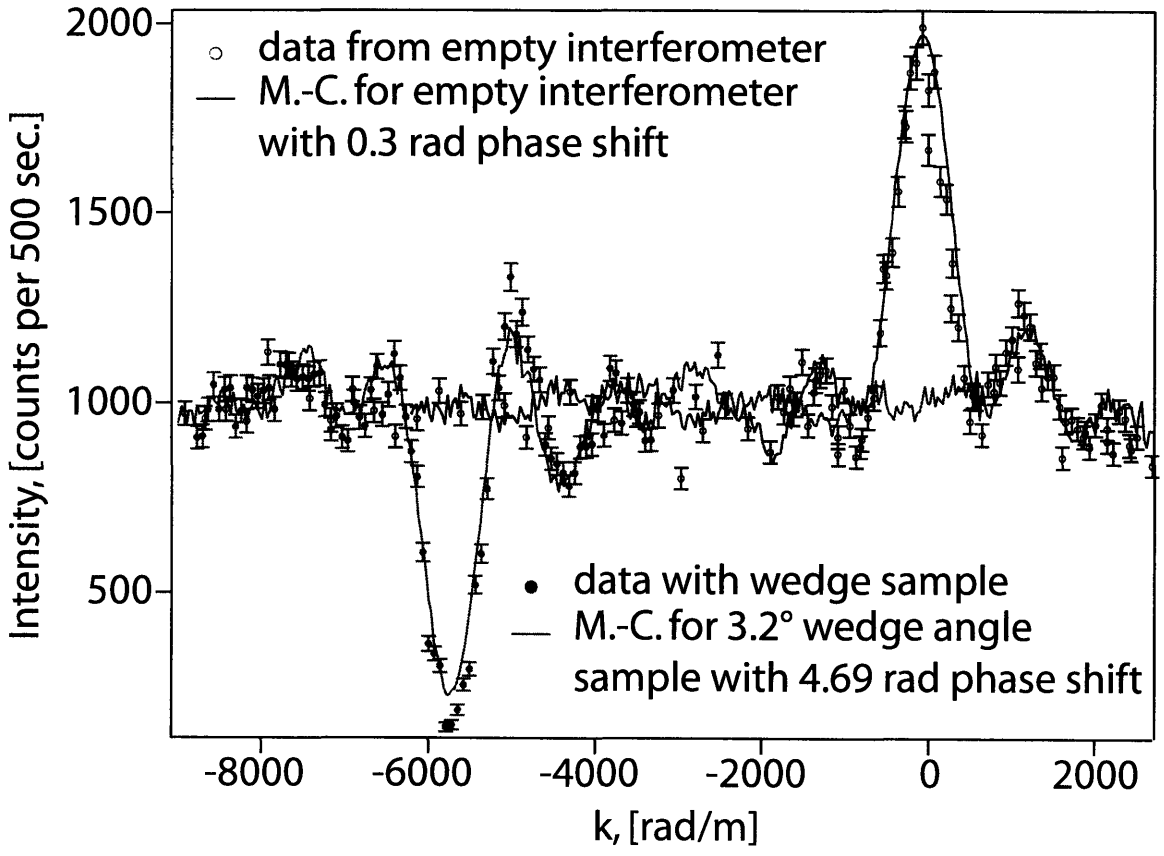

Figure 3-6: Measurement of a fused silica wedge-like sample. The figure represents the data and Monte-Carlo simulations with and without the wedge sample.

We explored two 1-D samples to demonstrate the methodology and to have data with which to implement the reconstruction algorithm: a wedge and a step sample. The wedge sample shows that the linear phase gradient can be refocused and has a very simple experimental signature (figure 3-6). Replacing the sample by a wedge has the result of offsetting the intensity of the empty interferometer scan by the 3°

wedge angle. The expected shift is (5200±200) rad·m^{-1}. The figure also shows a Monte-Carlo simulation of the uniformly divergent beam (the angle of the neutron momentum and the horizontal axis has a uniform distribution between -0.2° and +0.2°) with 3.2° wedge-sample. Since the wedge has a minimum nominal thickness of 6.4 mm, there is an additional phase shift of 4.69 rad (4.89 rad±0.17 rad measured). For the wedge sample experiment, we used a vertically focused neutron beam in order to increase the intensity on the position sensitive detector that has a 20% efficiency.

3.4.5 Step-like Sample Data

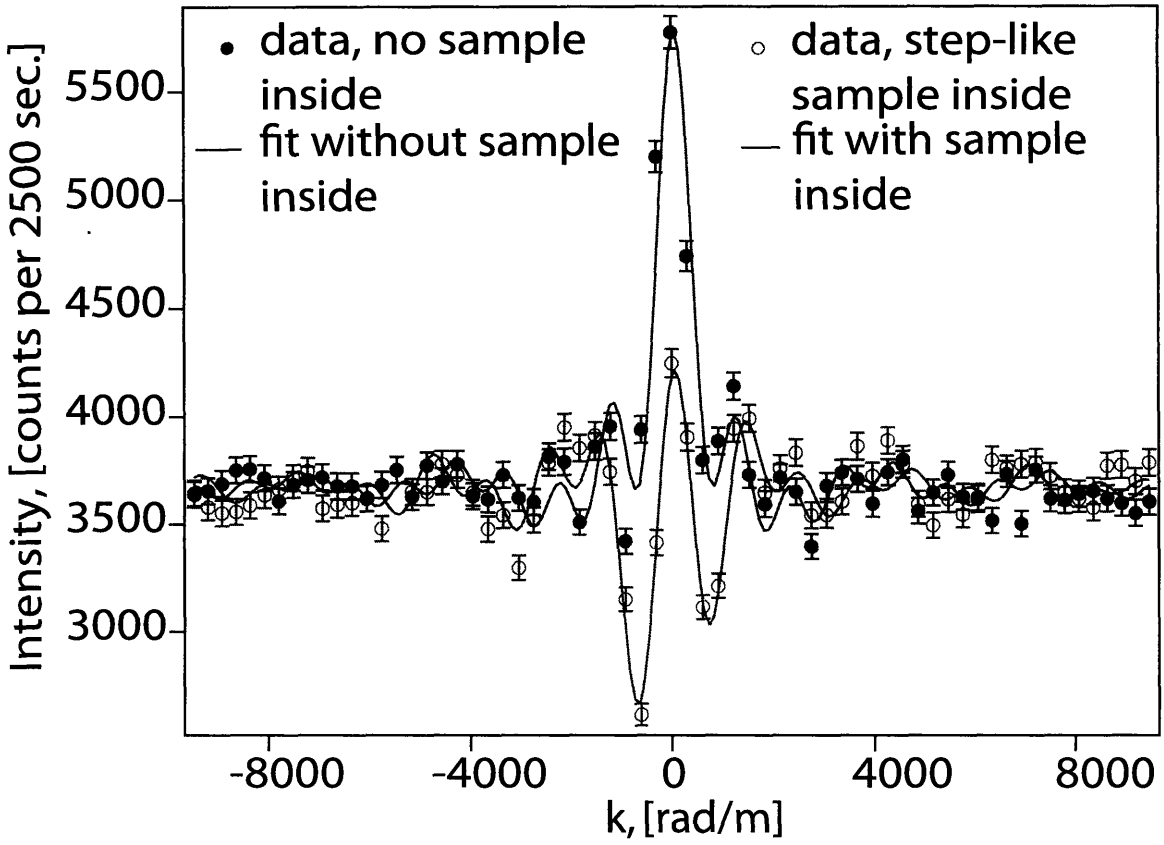

Figure 3-7: Step-like sample data. The sample is a thin (25 μm) fused silica slab which covers only part of the neutron beam and represents a step-like sample. This sample does not create phase variation along the beam bigger than π, which simplifies the reconstruction. Here we show raw data with the sample (open red circles) and data without the sample (filled blue circles).

Finally, we report in figures 3-7 and 3-8 the results from a step sample so that we

can observe the resolving power of the method. In this case the neutron beam is well collimated ($< 0.2°$ divergence). The sample is a 25 μm thick fused silica flat which partially covers the top of the beam.

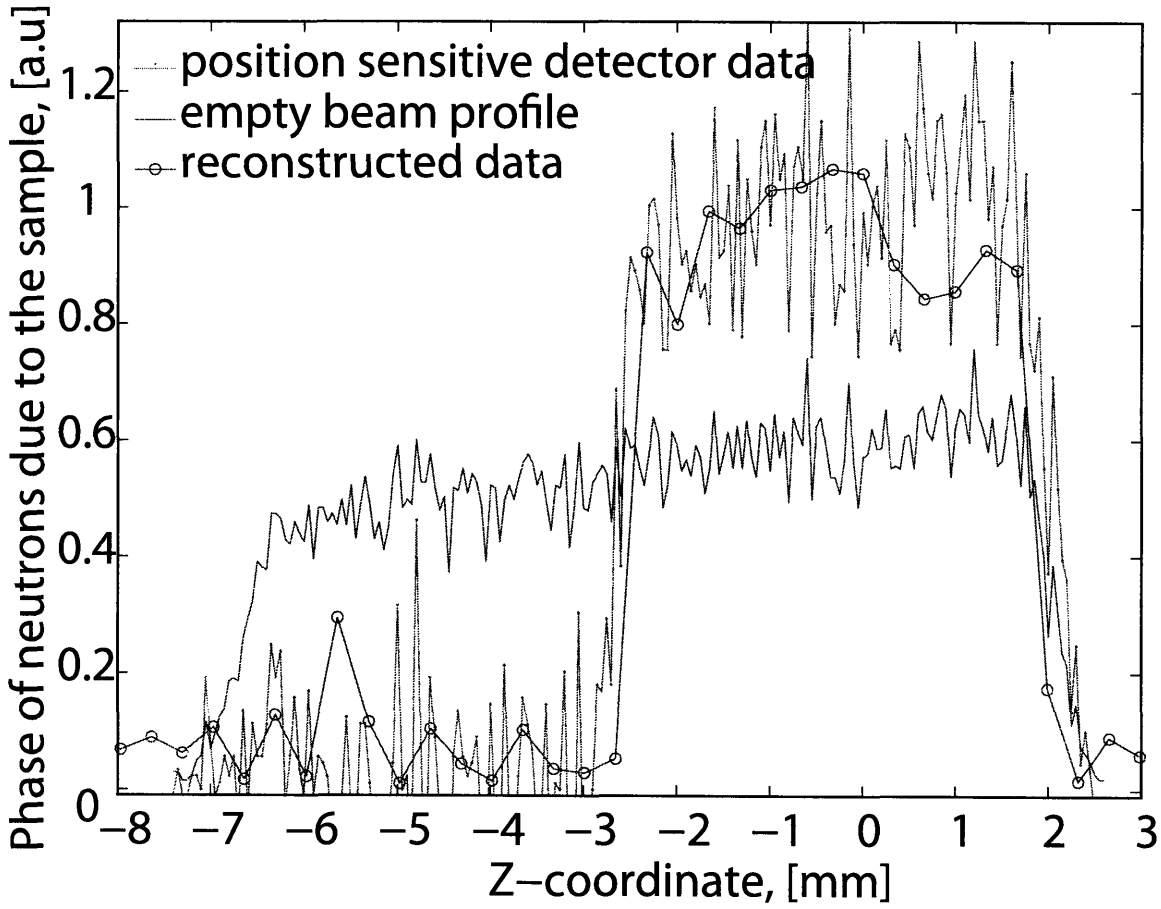

Figure 3-8: Step-like sample reconstructed images. Open blue circles represent a reconstructed image of the step-sample, the purple line is a 1-D image of the sample obtained using a position sensitive detector, and the green line is the the beam profile on the position sensitive detector without a sample.

Figure 3-7 shows the raw data (open red circles) as integrated intensity versus wave-number, **k**. We show data without the sample (filled blue circles) for comparison. The smooth lines are fits to the data assuming a uniform, non-divergent beam. Figure 3-8 shows the reconstructed 1-D image of the sample (open blue circles). We also show the 1-D images of the empty beam (green line) and the sample (purple line) measured separately with a position sensitive detector. Data from the different measurements are in very good agreement.

3.5 Reconstruction Method

Here we outline a simple reconstruction method. The intensity on the O-detector is described by equation 3.3, where we want to recover $\phi_s(\mathbf{r})$, the sample phase function. From a scan without the sample we can extract the parameters $A = (C_1^2 + C_2^2)/2$, $B = C_1 C_2$ and ϕ_0. Define $\tilde{\phi}(\mathbf{r}) = \phi_s(\mathbf{r}) + \phi_0$ and $\tilde{A} = \int A d\mathbf{r}$. In order to extract the Fourier components we need to measure values of intensity for $\mathbf{k}$ and $-\mathbf{k}$:

$$
\begin{aligned}
I_O(\mathbf{k}) - I_O(-\mathbf{k}) &= -2 \int B \sin(\mathbf{k}\cdot\mathbf{r}) \sin\tilde{\phi}(\mathbf{r}) d\mathbf{r} && (3.4)\\
I_O(\mathbf{k}) + I_O(-\mathbf{k}) &= 2(\tilde{A} + \int B \cos(\mathbf{k}\cdot\mathbf{r}) \cos\tilde{\phi}(\mathbf{r}) d\mathbf{r}). && (3.5)
\end{aligned}
$$

Setting ϕ_0 to 0 and $\pi/2$ and defining the intensity with a sample inside the beam as $I_{in}(\mathbf{q}, \phi_0)$, we get:

$$
\begin{aligned}
F_{sin}(\mathbf{k}) &= \frac{I_{in}(\mathbf{k},\pi/2) + I_{in}(-\mathbf{k},\pi/2) - 2\tilde{A}}{2B} + i\frac{I_{in}(-\mathbf{k},0) - I_{in}(\mathbf{k},0)}{2B}\\
F_{cos}(\mathbf{k}) &= \frac{I_{in}(\mathbf{k},0) + I_{in}(-\mathbf{k},0) - 2\tilde{A}}{2B} + i\frac{I_{in}(-\mathbf{k},\pi/2) - I_{in}(\mathbf{k},\pi/2)}{2B},
\end{aligned}
\qquad (3.6)
$$

$F_{sin}(\mathbf{k})$ and $F_{cos}(\mathbf{k})$ are the Fourier transforms of the $\sin(\phi_s(\mathbf{r}))$ and $\cos(\phi_s(\mathbf{r}))$ function, respectively:

$$
\begin{aligned}
F_{sin}(\mathbf{k}) &= FT(\sin(\phi_s(\mathbf{r})))\\
F_{cos}(\mathbf{k}) &= FT(\cos(\phi_s(\mathbf{r}))).
\end{aligned}
\qquad (3.7)
$$

Applying the inverse Fourier transforms to Equation (3.6) and then the inverse *sine* or *cosine* functions we obtain the sample phase function along the gradient direction:

$$
\begin{aligned}
\phi_s(\mathbf{r}) &= \sin^{-1}\left[IFT(F_{sin}(\mathbf{k}))\right]\\
\phi_s(\mathbf{r}) &= \cos^{-1}\left[IFT(F_{cos}(\mathbf{k}))\right].
\end{aligned}
\qquad (3.8)
$$

3.6 Conclusion and Analysis

From the Nyquist theorem, the image resolution depends on the maximum measured wave-number,

$$
|\Delta\mathbf{r}| = \frac{\pi}{|\mathbf{k}_{max}|}. \qquad (3.9)
$$

In order to have 1 μm resolution, we need to use a maximum gradient of the order 3.14×10^6 rad $\cdot m^{-1}$. This corresponds to the gradient in the phase produced by a fused silica wedge with an 88°-wedge angle. In our case, the maximum gradient ($2 \cdot 10^4$ rad$\cdot m^{-1}$) produced by two 6° wedges corresponds to 160 μm of spatial resolution.

2-D images can be produced by several methods. One such method is to rotate the sample around the neutron beam in incremental steps, repeating the experiment for each step and reconstructing the image by back projection. Another method is by adding a gradient perpendicular to the first one, whereby varying the gradients independently (achieved by rotation of the wedges) we collect 2-D Fourier coefficients. The image is thus obtained via a 2-D inverse Fourier transform.

Due to limited instrument time, this experiment is intended as a proof of principle. We did not plan to achieve or surpass current available resolution. We see that the method has the potential for high spatial resolution and is not limited by position sensitive detectors. Also, the proposed method works well with small and very thin samples that are difficult to study by radiographic techniques. Limitations here arise from the quality of the beam, the quality of the phase gradient, and neutron statistics (in order to resolve high **k**-values).

Chapter 4

Vertical Coherence Length

In this chapter we report the measurement of a 600 Å vertical coherence length for a single crystal neutron interferometer. The vertical coherence length describes the loss of the contrast as one path of the interferometer is shifted relative to the other in the vertical direction. We offset each path via a pair of prisms placed in the legs of the interferometer and measure the loss in contrast as the relative offset is increased. The measured coherence length is consistent with the experimental distribution of the incoming neutron beam momentum in the vertical direction. Finally, we demonstrate that the loss of contrast with the beam displacement in one leg of the interferometer can be recovered by introducing a corresponding displacement in the second leg of the interferometer. This reinforces the idea that the loss of the contrast is not due to interferometer imperfections but due to the vertical momentum spectrum of the incoming beam. As previously suggested by Rauch, the experimental technique for vertical coherence measurement could be used to characterize the spectrum of k_z such as in Fourier Spectroscopy or Reflectometry [40].

4.1 Introduction

The coherence length describes the spatial extent over which coherent information is preserved in interferometry [41]. In a neutron interferometer [16], the coherence length is a function of the quality of the single crystal, the momentum distribution

of the incoming neutron beam, and a variety of environmental contributions such as temperature gradients and vibrations. Generally three coherent lengths are identified [42]: the transverse coherence length, the vertical, and the longitudinal (see figure 4-1). Here we explore the vertical component in a system where the coherence length is primarily limited by the incoming beam characteristics. Heisenberg's uncertainty relation defines the coherence length $l_c \equiv \delta r = 1/(2\delta k)$ which is longer for smaller uncertainties in δk. To understand this effect, we study the contrast associated with a wave-packet composed of an incident distribution of plane waves corresponding to the distribution of neutron momentum in the vertical direction. The measurement of the coherent length is a direct measurement of the spatial extent of this wave-packet.

In previous measurements of the coherence function [42] in the low coherence regime, the coherence was partially recovered by postselection methods. For our measurement we do not postselect. The coherence (l_c) is revealed by a simple projective measurement. An interferometer with a long coherence length opens up the possibilities of using interferometer for quantum information processing and provides a new approach to extend coherent scattering to the μm length scale.

4.2 Theory

Neutron interferometry is a practical example of macroscopic quantum coherence [43]. A schematic picture of the coherence length experiment is shown in figure 4-1. We will describe the experiment via the neutron wave-function over the Mach-Zehnder interferometer. At the first blade, the neutrons are split by Bragg scattering into two paths. In the absence of the prisms, the neutron wave-function is spanned by *path I* and *path II* (figure 4-1)

$$\Psi = e^{i\phi_1} C_1 \left| path\ I \right\rangle + e^{i\phi_2} C_2 \left| path\ II \right\rangle , \tag{4.1}$$

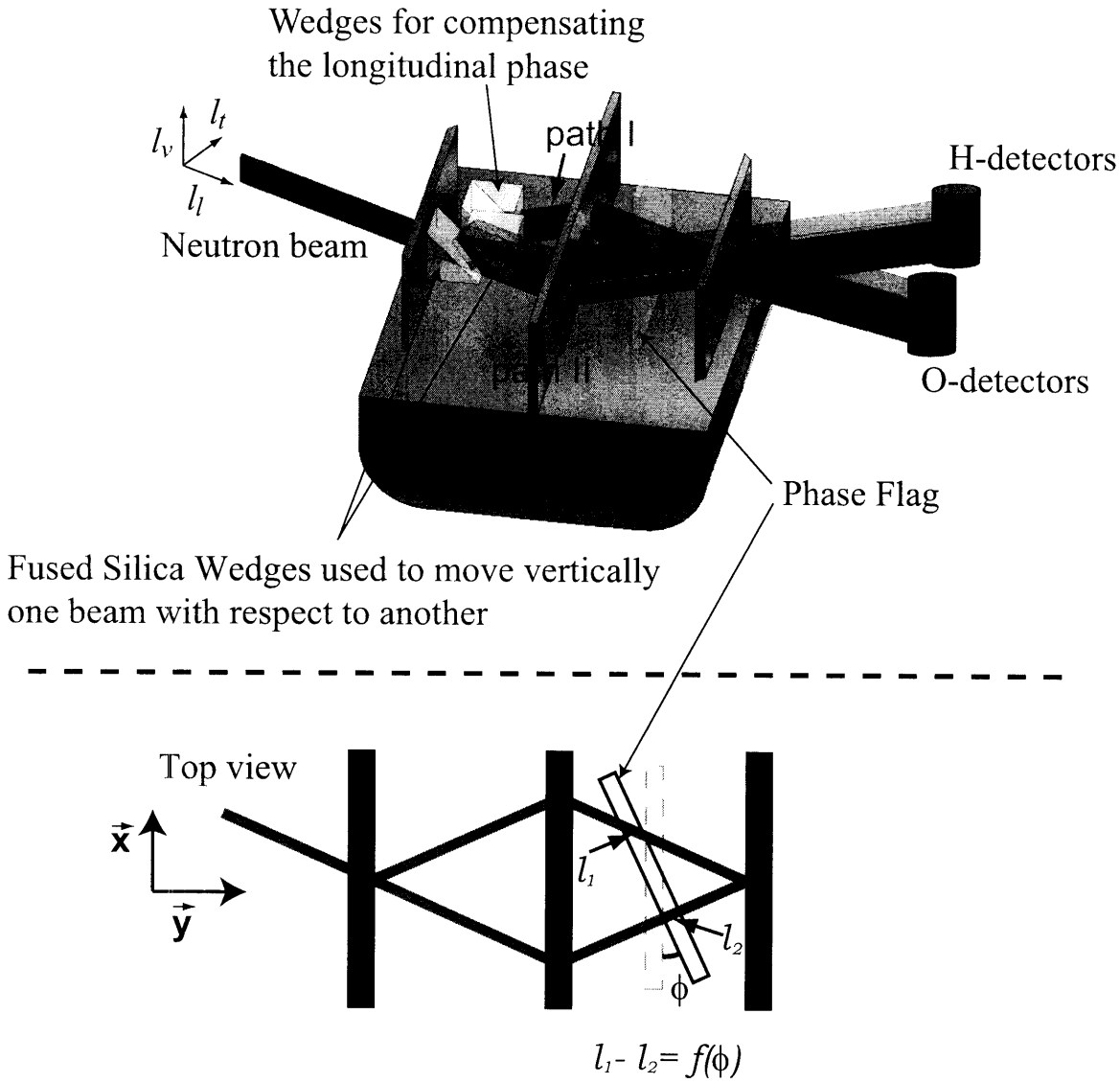

Figure 4-1: A schematic diagram of the coherence length experiment. A neutron beam, entering at left, is coherently divided into two paths (paths I and II) via Bragg diffraction on the first blade of the neutron interferometer. The phases which neutron accumulates over each path are experimentally controlled by rotating the phase flag. Notice that the path lengths (l_1 and l_2) due to the phase flag (in the path I and path II) will depend on the angle (ϕ) of the phase flag rotation, thus the phase difference ($\phi_0 = \phi_1 - \phi_2$) between path I and path II. In one of the paths we install two 45° prisms, which form a cube at 0 separation. By separating the prisms we shift the neutron beams in path I and II vertically with respect to each other. We observe a loss in contrast with displacement, which we measure with the help of a phase shifter (shown on the figure) and neutron detectors, behind interferometer.

where φ_1 and ϕ_2 are the phases accumulated over *path I* and *path II* in the absence of the prisms. The coefficients C_1 and C_2 are parameters of the neutron in-

terferometer that account for the attenuation and scattering losses of the neutron beam. Thus the signal I_O at the O-detector is proportional to the phase difference $\phi_0 = (\phi_1 - \phi_2)$ that neutrons accumulate over *path I* and *path II* ($I_O \propto ((C_1^2 + C_2^2)/2 + C_1 C_2 \cos\phi_0)$ [16]). The phase sensitivity arises from the interference of the two paths. The phases which the neutron accumulates over each path is experimentally controlled via phase flag rotation. The difference between optical path lengths $(l_1 - l_2)$ of the neutron inside the phase flag depends on the phase flag rotation angle (figure 4-1 - top view).

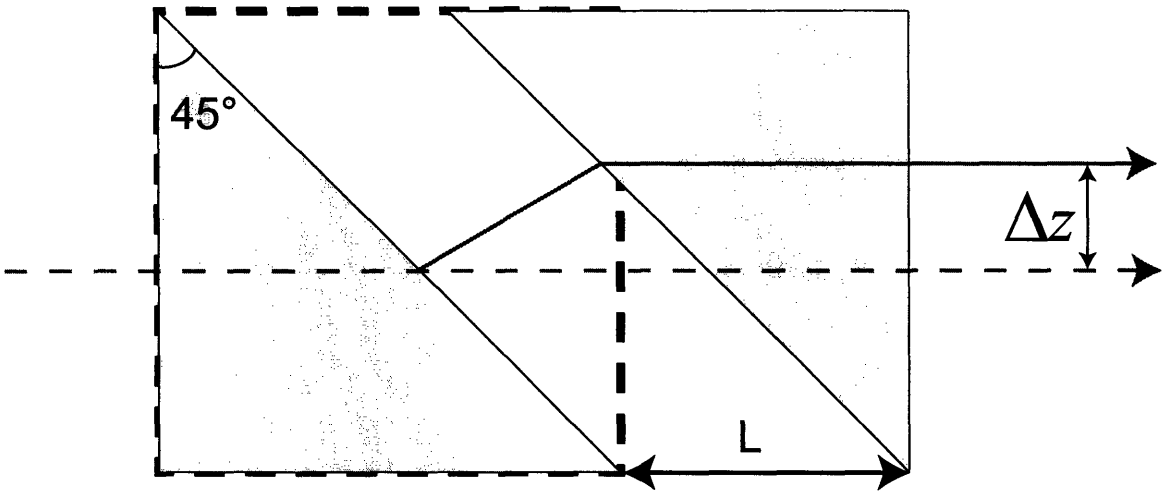

Figure 4-2: A schematic diagram of the neutron paths through the prisms for $k_z = 0$. The neutron beam enters from the left and, depending on the separation between the prisms, is shifted vertically. If the separation of the prisms (L) is equal to zero, then the neutron beam passing through the prisms is going through without any vertical offset (dashed blue line). If the separation (L) is non-zero, then the neutron beam is refracted and is not horizontal due to the index of refraction change on the exit of the first prism. The second prism refracts the neutron beam back in the horizontal position (straight red line). The beam offset (Δz) due to the set of prisms is directly proportional to the prism separation (L): $\Delta z = L(1 - n)$, where n is the index of refraction of the prisms.

A pair of fused silica (90° angle, 15 mm side size) prisms forming a cube is placed in each path of the interferometer. As the prisms in one path are separated, the neutron beam in that path is shifted vertically in a well-controlled fashion by a distance Δ**z** (see figure 4-2). The beam offset (Δz) due to the set of prisms is directly proportional to the prisms separation (L): $\Delta z = L(1 - n)$, where n is the index of refraction of

the prisms. In addition to being displaced, a phase shift is introduced into the wave-function. This phase turns out to be quite small and its effects are not observed in our measurements (the full derivation and small angle approximation are outlined in the appendix A), so we will suppress it in the description that follows; however, our simulations do include it. If $k_z = 0$, the coherence length we would measure would be a function of the interferometer. However for our experiments the coherence length is limited by the spread in k_z. Therefor we calculate the contrast for $k_z \neq 0$.

The vertical shift in the prisms can be seen by the index of refraction of the neutron

$$n = \frac{K_{inside}}{k_0} \approx 1 - \lambda^2 \frac{N b_c}{2\pi} \approx 1 - \Delta n, \tag{4.2}$$

where b_c is the coherent scattering length, N is the atomic density, K_{inside} is the wave vector of neutron inside the prisms, and k_0 is the wave vector of the incident neutron. We have ignored the reactive cross-section. The vertical beam shift due to the sets of prisms is

$$\Delta \mathbf{z} = \Delta z_m (1 + \tan\gamma_1) - L \tan\gamma, \tag{4.3}$$

where $\Delta z_m = L \cos 45^\circ \sin\gamma_2 / \sin(45^\circ - \gamma_2) = L \tan\gamma_2 / (1 + \tan\gamma_2)$ is the vertical shift of the neutron beam in between the prisms in *path II* (see figure 4-3). Using a small angle approximation, the path separation is $\Delta \mathbf{z} = L\Delta n(1 - 2\gamma)$. Since $\tan\gamma = k_z/k$ and $\tan\gamma_1 \approx k_z/(nk)$, we can rewrite $\Delta \mathbf{z}$ for small angles as

$$\Delta \mathbf{z} = L\Delta n(1 - 2\frac{k_z}{k}). \tag{4.4}$$

Thus even for $k_z \neq 0$ in the first approximation the $\Delta z = L\Delta n = L(1 - n)$.

Let's consider a neutron as a plane wave with a wave-vector $\mathbf{k}$. If this vector $\mathbf{k}$ is not perpendicular to the vertical coordinate of the interferometer, then upon passing through the prisms, the vertical shift of the neutron beam will produce an additional phase shift of $\mathbf{k}\Delta\mathbf{l} = \mathbf{k}\left(\Delta\mathbf{z}\frac{\mathbf{k}}{|\mathbf{k}|}\right)\frac{\mathbf{k}}{|\mathbf{k}|} = \mathbf{k}\Delta\mathbf{z} = \mathrm{k_z}\Delta\mathrm{z}$ (this is easy to see in figure 4-3 where at the edge of the prism the phases for the two beams are the same. In this case, a non-zero k_z will produce a phase shift.).

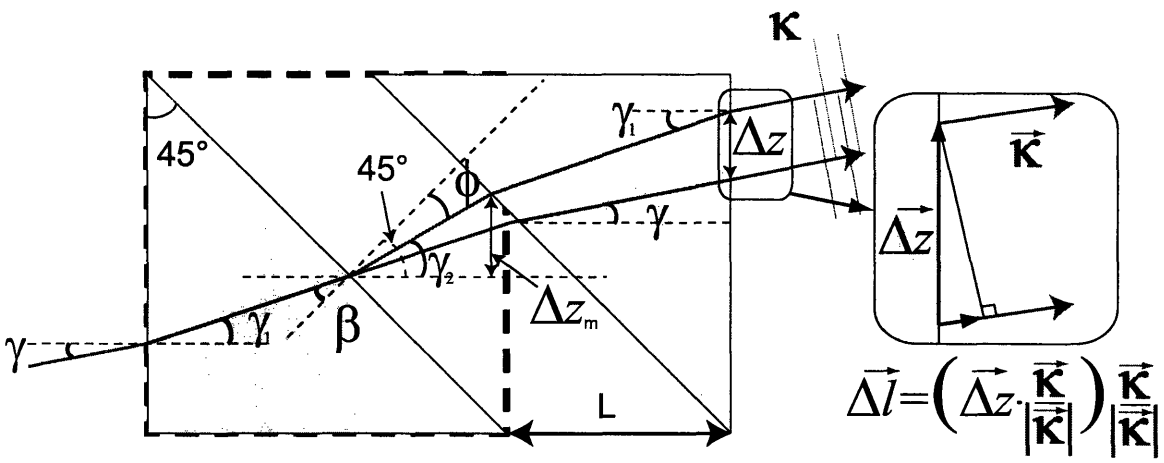

Figure 4-3: A schematic diagram of the neutron paths through the prisms. The neutron beam enters from the left and, depending on the separation between the prisms, is shifted vertically. The angles shown on the figure correspond to the calculations for path separation and phase shifts of the neutron described in the text.

Following the operator description introduced in Section 1.3 of Chapter 1, we can write the actions of interferometer, phase flag and prisms in an operator form. As before, we label the states according to the sign of k_x, the neutron momentum in the **x** direction. The incoming neutron is therefore in the $|+\rangle$ state. In order to keep track of neutron beam offsets in the future (after the prisms), we label the states $|+\rangle$ and $|-\rangle$ by beam offset (0 or Δz) due to the prisms. The wave-function of the incoming neutron could be written in terms of the beam offset Δz, i.e. $|+\rangle_0$ or $|+\rangle_{\Delta z}$. Then the incoming neutron state (which is analogous to the previous one) is

$$|\Psi_{in}\rangle = 1 \cdot |+\rangle_0 + 0 \cdot |-\rangle_0 + 0 \cdot |+\rangle_{\Delta z} + 0 \cdot |-\rangle_{\Delta z} = \begin{pmatrix} 1 \\ 0 \\ 0 \\ 0 \end{pmatrix}. \tag{4.5}$$

Let's note that to first order in the incoming angle γ, the effect of the prism on the beam is simply to shift it vertically by $\Delta z = L\Delta n$. If $|\psi\rangle$ and $|\psi'\rangle$ are wave functions of the neutron respectively before and after the prism, the quantum operation $\hat{O}_{\Delta z}$

performed by it is defined by

$$\langle z\,|\psi'\rangle = \left\langle z\left|\hat{O}_{\Delta z}\right|\psi\right\rangle = \langle z-\Delta z\,|\psi\rangle$$

. Since the prism is present only in path "−", the beams are transformed according to

$$\begin{cases} |+\rangle \longrightarrow |+\rangle \\ |-\rangle \longrightarrow \hat{O}_{\Delta z}\,|-\rangle \end{cases}$$

Formally, we can write the effect of the prism on these particular beams as a matrix acting on the space spanned by the states $\{|+\rangle = |+\rangle_0, |-\rangle = |-\rangle_0, \hat{O}_{\Delta z}\,|+\rangle = |+\rangle_{\Delta z}, \hat{O}_{\Delta z}\,|-\rangle = |-\rangle_{\Delta z}\}$:

$$\hat{O}_{\Delta z} = \begin{pmatrix} 1 & 0 & 0 & 0 \\ 0 & 0 & 0 & 0 \\ 0 & 0 & 0 & 0 \\ 0 & 1 & 0 & 0 \end{pmatrix}. \tag{4.6}$$

This matrix is not unitary, but it is still a valid description of the prism's action as far as the input states $|+\rangle$ and $|-\rangle$ are concerned and is sufficient for bookkeeping purposes.

The blade operator in the Δz representation is

$$\hat{O}_B = \begin{pmatrix} t & -r^* & 0 & 0 \\ r & t^* & 0 & 0 \\ 0 & 0 & t & -r^* \\ 0 & 0 & r & t^* \end{pmatrix}, \tag{4.7}$$

and the phase shifter operator is

$$\hat{\Phi} = \begin{pmatrix} e^{\imath\phi_0} & 0 & 0 & 0 \\ 0 & 1 & 0 & 0 \\ 0 & 0 & e^{\imath\phi_0} & 0 \\ 0 & 0 & 0 & 1 \end{pmatrix}. \tag{4.8}$$

Due to the vertical shift Δz and vertical momentum of the neutron k_z, the neutron on the third blade will account a phase difference, which for different paths is $k_z \Delta z$

$$\hat{\Phi}_{\Delta z} = \begin{pmatrix} 1 & 0 & 0 & 0 \\ 0 & 1 & 0 & 0 \\ 0 & 0 & e^{\imath k_z \Delta z} & 0 \\ 0 & 0 & 0 & e^{\imath k_z \Delta z} \end{pmatrix}. \tag{4.9}$$

The operator for the central blade is more complex. If for the moment we neglect the loss of transmitted neutrons, then we can approximate the action as that of a mirror. An approach to include the non-unitary dynamics of the second blade operator is to represent its action by means of a superoperator. The corresponding quantum operator must be convex-linear and completely positive, as well as trace non-increasing. Note that even though the action of the second blade is not trace-preserving, we still fulfill the above condition. We will represent the superoperator \$ as a Kraus sum (see chapter 1). The Kraus operators (up to a global phase) are then:

$$\{\mathcal{K}_j\} = \left\{ \begin{pmatrix} 0 & 0 & 0 & 0 \\ 0 & 0 & 0 & 0 \\ 0 & 0 & 0 & 0 \\ 0 & 0 & 0 & 0 \end{pmatrix}, \begin{pmatrix} 0 & -r^* & 0 & 0 \\ r & 0 & 0 & 0 \\ 0 & 0 & 0 & -r^* \\ 0 & 0 & r & 0 \end{pmatrix} \right\}. \tag{4.10}$$

That one of the Kraus operators is zero naturally corresponds to a loss of neutron, that the other is propotional to a perfect mirror completes the description.

Then if we have an incoming density operator (using 4.5) as

$$\rho_{in} = |\Psi_{in}\rangle\langle\Psi_{in}| = \begin{pmatrix} 1 & 0 & 0 & 0 \\ 0 & 0 & 0 & 0 \\ 0 & 0 & 0 & 0 \\ 0 & 0 & 0 & 0 \end{pmatrix}, \tag{4.11}$$

the output of the interferometer is

$$\rho_{out} = \sum_j \hat{O}_{B_3}\hat{\Phi}_{\Delta z}\hat{\Phi}\mathcal{K}_j\hat{O}_{\Delta z}\hat{O}_{B_1}\rho_{in}\hat{O}^\dagger_{B_1}\hat{O}^\dagger_{\Delta z}\mathcal{K}^\dagger_j\hat{\Phi}^\dagger\hat{\Phi}^\dagger_{\Delta z}\hat{O}^\dagger_{B_3}. \tag{4.12}$$

Substituting all expressions, we have for ρ_{out}:

$$\begin{pmatrix} |tr^2|^2 & -tr^*|tr|^2 & |tr^2|^2 e^{-\imath(k_z\Delta z+\phi_0)} & tr^*|r|^4 e^{-\imath(k_z\Delta z+\phi_0)} \\ -rt^*|rt|^2 & |rt^2|^2 & -rt^*|rt|^2 e^{-\imath(k_z\Delta z+\phi_0)} & -|tr^2|^2 e^{-\imath(k_z\Delta z+\phi_0)} \\ |tr^2|^2 e^{\imath(k_z\Delta z+\phi_0)} & -tr^*|tr|^2 e^{\imath(k_z\Delta z+\phi_0)} & |tr^2|^2 & tr^*|r|^4 \\ rt^*|r|^4 e^{\imath(k_z\Delta z+\phi_0)} & -|tr^2|^2 e^{\imath(k_z\Delta z+\phi_0)} & rt^*|r|^4 & |r|^6 \end{pmatrix}. \tag{4.13}$$

Our measurement is the projection on the state $\{|+\rangle_0 + |+\rangle_{\Delta z}\}$, which we can write as a measurement operator for the O-detector:

$$\hat{O}_O = \{|+\rangle_0 + |+\rangle_{\Delta z}\}\{{}_0\langle +| + {}_{\Delta z}\langle +|\} = \begin{pmatrix} 1 & 0 & 1 & 0 \\ 0 & 0 & 0 & 0 \\ 1 & 0 & 1 & 0 \\ 0 & 0 & 0 & 0 \end{pmatrix}. \tag{4.14}$$

and the intensity on the O-detector is

$$I_O = Tr(\hat{O}_O\rho_{out}) = 2|r^2t|^2\left(1+\cos\left(\phi_0 + k_z\Delta z\right)\right). \tag{4.15}$$

We can look on the same problem with another prospective and extract a new wave-function (or density matrix) for the O-beam detector. Here we consider now only beam in O-detector direction and will take in mind, that the beam in H-detector direction is removed by beam-blocker. Let's rearrange elements of the outgoing density matrix (eq. 4.13) so the block-diagonal matrices represent O and H beams and off-diagonal matrices correspond to interference between this beams. In the rearranged

basis $\{|+\rangle_0, |+\rangle_{\Delta z}, |-\rangle_0, |-\rangle_{\Delta z}\}$ the density matrix ρ'_{out} is

$$\left(\begin{array}{cc|cc} |tr^2|^2 & |tr^2|^2 e^{-\imath(k_z\Delta z+\phi_0)} & -tr^*|tr|^2 & tr^*|r|^4 e^{-\imath(k_z\Delta z+\phi_0)} \\ |tr^2|^2 e^{\imath(k_z\Delta z+\phi_0)} & |tr^2|^2 & -tr^*|tr|^2 e^{\imath(k_z\Delta z+\phi_0)} & tr^*|r|^4 \\ \hline -rt^*|rt|^2 & -rt^*|rt|^2 e^{-\imath(k_z\Delta z+\phi_0)} & |rt^2|^2 & -|tr^2|^2 e^{-\imath(k_z\Delta z+\phi_0)} \\ rt^*|r|^4 e^{\imath(k_z\Delta z+\phi_0)} & rt^*|r|^4 & -|tr^2|^2 e^{\imath(k_z\Delta z+\phi_0)} & |r|^6 \end{array}\right). \tag{4.16}$$

When we perform a measurement of the H-beam (or block the beam with beam-blocker) we loose all information in the density matrix related to the H component and interference between the H and O beams. In this case, either we perform a measurements on the H-beam or remove it by beam-blocker, the elements of the density matrix set to zero outside of the first sub-diagonal

$$\rho_O = \left(\begin{array}{cc|cc} |tr^2|^2 & |tr^2|^2 e^{-\imath(k_z\Delta z+\phi_0)} & 0 & 0 \\ |tr^2|^2 e^{\imath(k_z\Delta z+\phi_0)} & |tr^2|^2 & 0 & 0 \\ \hline 0 & 0 & 0 & 0 \\ 0 & 0 & 0 & 0 \end{array}\right). \tag{4.17}$$

Notice that removing the H-beam corresponds to a loss of neutrons. In fact for some phase setting all the neutrons can be lost. So we will extract the upper sub-diagonal to keep the information about those neutrons in upper path and scale this by the number of neutrons that remain.

Due to the removal H-beam and knowledge that sum intensity of O and H beam should stay constant, we can insert normalization $2|r^2t|^2\left(1+\cos\left(\phi_0+k_z\Delta z\right)\right)$ by hand. Re-normalized density matrix is

$$\rho'_O = 2|r^2t|^4\left(1+\cos\left(\phi_0+k_z\Delta z\right)\right)\begin{pmatrix} 1 & e^{-\imath(k_z\Delta z+\phi_0)} \\ e^{\imath(k_z\Delta z+\phi_0)} & 1 \end{pmatrix}. \tag{4.18}$$

In this case the measurements operator is

$$\hat{O}_M = |+\rangle_0 \langle +|_0 + |+\rangle_{\Delta z} \langle +|_{\Delta z} = \begin{pmatrix} 1 & 0 \\ 0 & 1 \end{pmatrix}. \tag{4.19}$$

Thus intensity on the O-detector is

$$I_O(\phi_0) = Tr(\hat{O}_M \rho'_O) = 2|r^2 t|^4 \left(1 + \cos\left(\phi_0 + k_z \Delta z\right)\right), \tag{4.20}$$

For an incoherent sum of plane waves, the intensity on the detector is,

$$I_O(\phi_0) = \int \rho(k_z) Tr(\hat{O}_O \rho_{out}) dk_z = \int \rho(k_z) 2|r^2 t|^2 \left(1 + \cos\left(\phi_0 + k_z \Delta z\right)\right) dk_z, \tag{4.21}$$

where $\rho(k_z)$ is the neutron vertical momentum probability distribution. The contrast is contained in the second term of the integral and the loss of contrast is a result of averaging over a momentum distribution.

4.3 Experiment

The measurements were made at the Neutron Interferometer and Optical Facility (NIOF) at the National Institute of Standards and Technology [28]. It consists of a perfect Si-crystal neutron interferometer shown in figure 4-1 with high phase contrast ($> 80\%$). The existing interferometer was machined from a silicon single crystal ingot and operates on a cold neutron beam ($E = 11.1$ meV, $\lambda = 0.271$ nm). A detailed description of the facility can be found in Ref. [39, 16].

Special care needs to be taken to observe a coherence length approaches μm scales. We need high phase stability and high intensity to observe a large enough signal-to-noise ratio on the phase stability time scale. The phase stability can be influenced by environmental noise such as vibrations, acoustics, and temperature fluctuations. The NIOF at NIST is very well isolated from environmental noise [28]. In order to increase the phase stability over long periods of time, special care was taken to con-

trol the temperature and to remove any temperature gradients in the interferometer enclosure. We installed two PT-100 calibrated thermometers at a different locations of enclosure (one of them in close vicinity of the neutron interferometer) and set of heaters. Using the PID temperature controller, we were able to maintain the temperature of the enclosure stable with ± 5 mK precision. This dramatically improved the phase stability of our system.

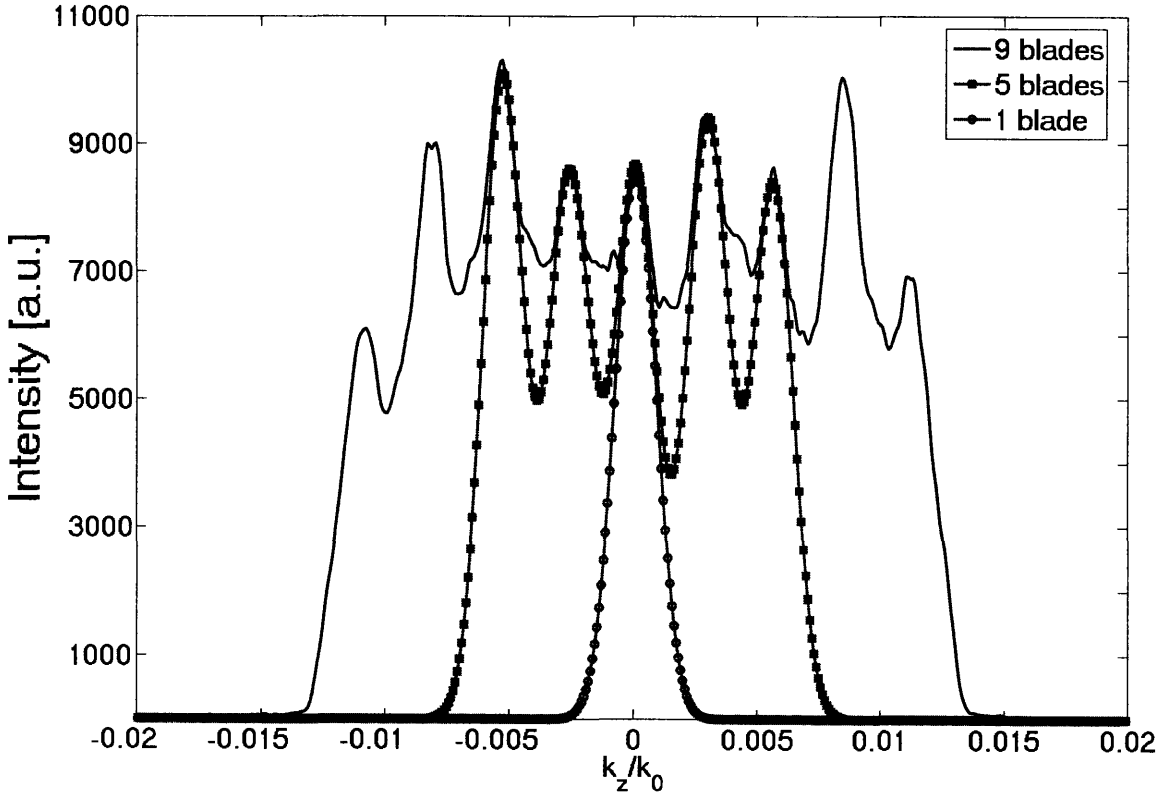

Figure 4-4: The vertical momentum distribution for the incoming neutron beam. The 2^{nd} monochromator consists of 9 focusing blades in order to increase the intensity. The solid curves in figure 4-5 were calculated from the distributions shown here. The 9-blade result was measured and the 5 and 1 blade distributions are just a simple model consisting of displaced Gaussians.

In order to increase the intensity, we used the second monochromator as a focusing device. This monochromator consists of 9 pyrolytic graphite (PG) blades. Each blade was independently adjusted to focus the neutron beam vertically on the first blade of the interferometer. While focusing the beam, we attempted to keep the beam profile uniform in intensity. The focused beam provides a much higher intensity and

reduces the measurement time. As expected, the focused beam (bigger δk_z vertical momentum spread) produced a smaller coherent length ($l_v \propto 1/\delta k_z$).

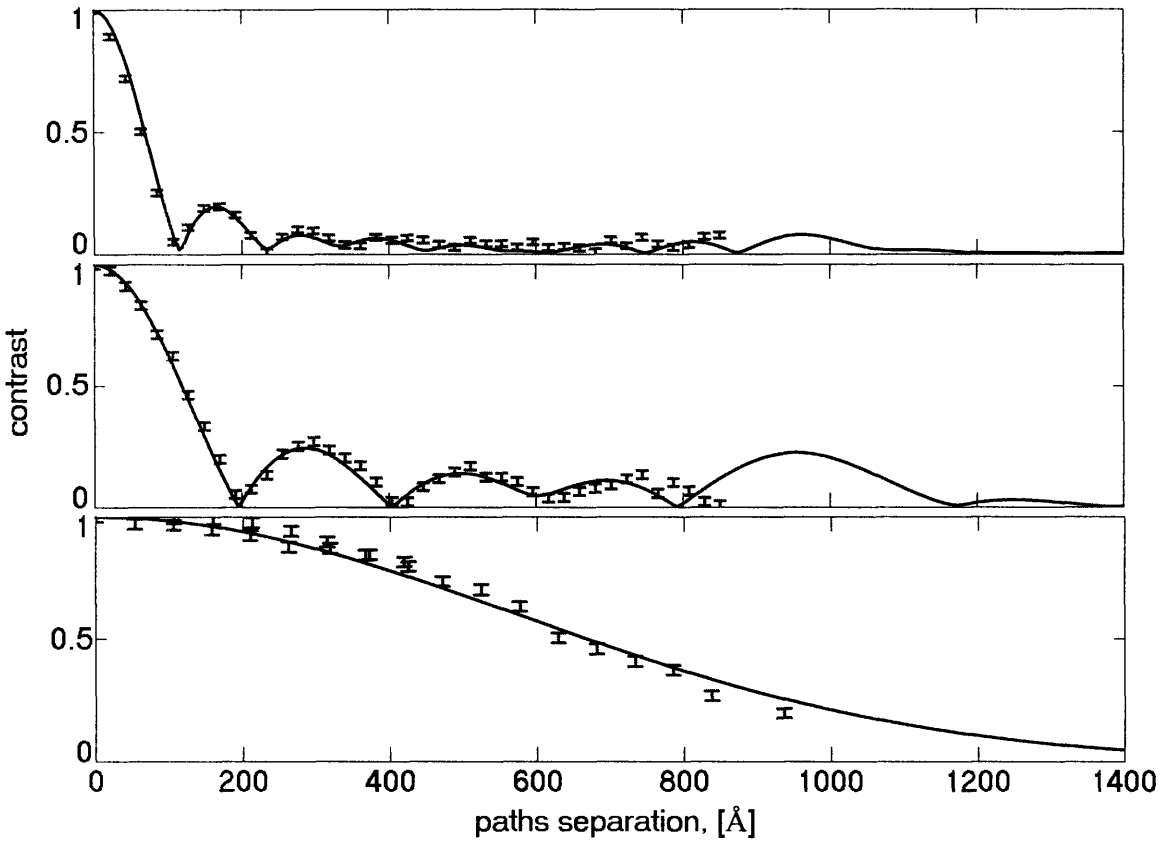

Figure 4-5: Contrast plots for three different vertical beam divergences. In each subplot data are shown with closed circles. The lines are contrast curves derived as a sum of plane waves using the vertical momentum distribution (k_z) shown in figure 4-4. The beam profiles data is very closely described by sum of plane waves with measured and approximated vertical beam distributions.

Figure 4-4 shows the distribution of the vertical momentum for the incoming beam. The beam break consists of a pyrolytic graphite monochromator followed by a set of 9 PG crystals that focus the beam ($\lambda_n = 2.71$ Å) in the vertical direction at the input of the interferometer. A measured distribution corresponds to a sum of nine distributions that are offset from each other by the mean momentum from the individual graphite blades of the focusing monochromator. A detailed description of the vertical momentum distribution measurement is outlined in appendix B.

In figure 4-5 we report series of measurements of the contrast for the all 9 blades, for the central 5 blades, and for the central-most blade. As expected, the contrast

length increases as we narrow the momentum distribution of the incoming neutron beam. Notice that in the narrowest case, the contrast remains up to 1000 Å in the vertical separation of the paths. Here we also show, with straight lines, the contrast curves obtained by approximating the wave-function of the neutrons as a plane wave and integrating over the vertical momentum distribution. In these simulations we used the vertical momentum distributions shown in figure 4-4. It is clearly seen that the plane wave simulation approximates the measured contrast behavior well.

To convince ourselves that the observed loss of contrast is not due to single crystal interferometer irregularities, we recover the contrast by shifting the path of the neutron beam in path II in the same direction as in path I (figure 4-6). We see that the two curves are the same (within experimental errors), simply shifted relative to each other by 4 mm. Thus the loss of the contrast is not due to interferometer imperfections, but due to the vertical momentum spectrum of the incoming beam.

4.4 Conclusion

We have measured the vertical coherence function of a single crystal neutron interferometer via path separation and for different vertical beam distributions. We extended this measurement to 1000 Å. In one of the beam configurations (the single blade monochromator), we observed a coherence length of about 1000 Å.

In addition, we want to mention that the output neutron state (coherent superposition of the state with the same but shifted vertically state) which was created with use of the separated prisms, can provide a basis for new experiments.

Thus, a single crystal neutron interferometer with a long coherence length provides new opportunities for experiments such as Fourier Spectroscopy [40] (proposed experimental setup is shown on figure 4-7) and coherence scattering over scales that are not easily accessible by other approaches.

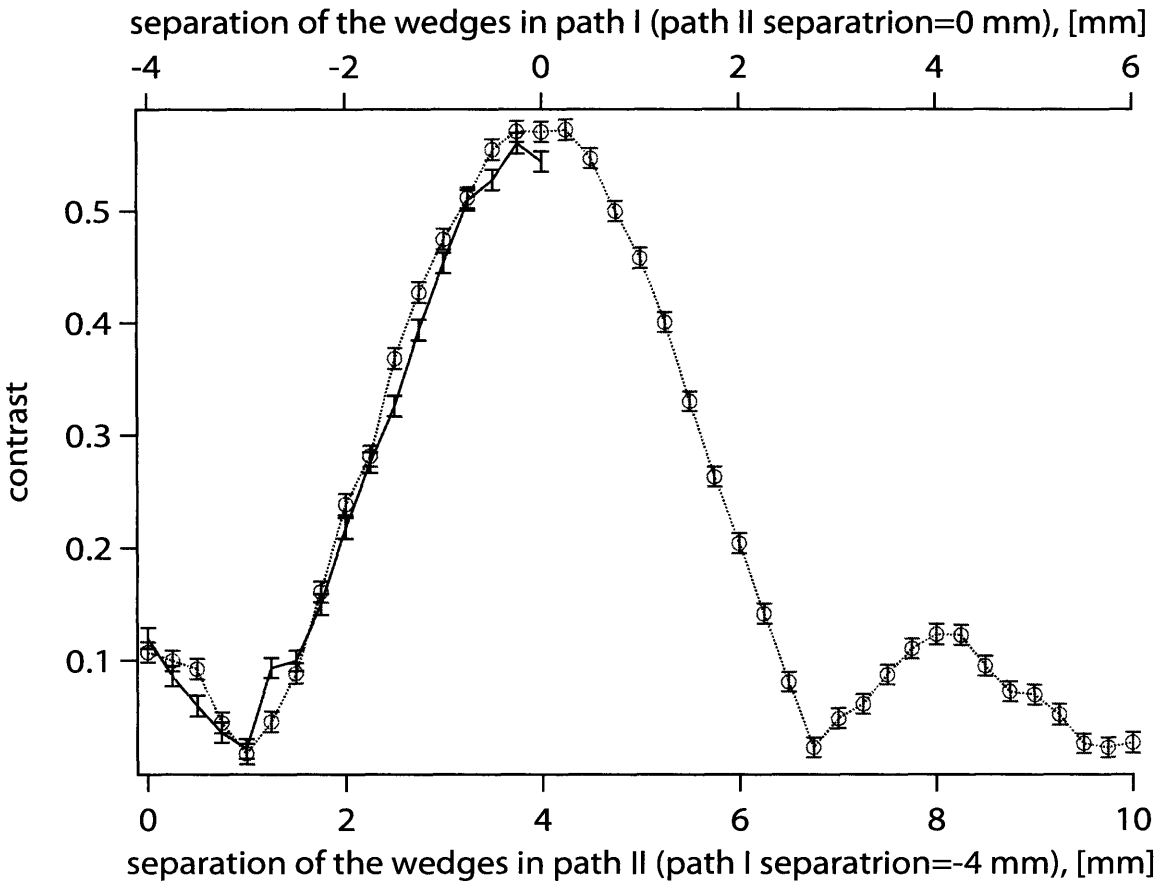

Figure 4-6: A contrast plot for two cases. The solid line is the contrast measured when the prism separation in path II is 0 mm, and the dashed line is the contrast measured when the prism separation in path I is set to 4 mm. We see that the two curves are the same (within experimental errors) simply shifted relative to each other by 4 mm. This shows that indeed the loss of the contrast can be recovered and is not due to imperfections in the interferometer.

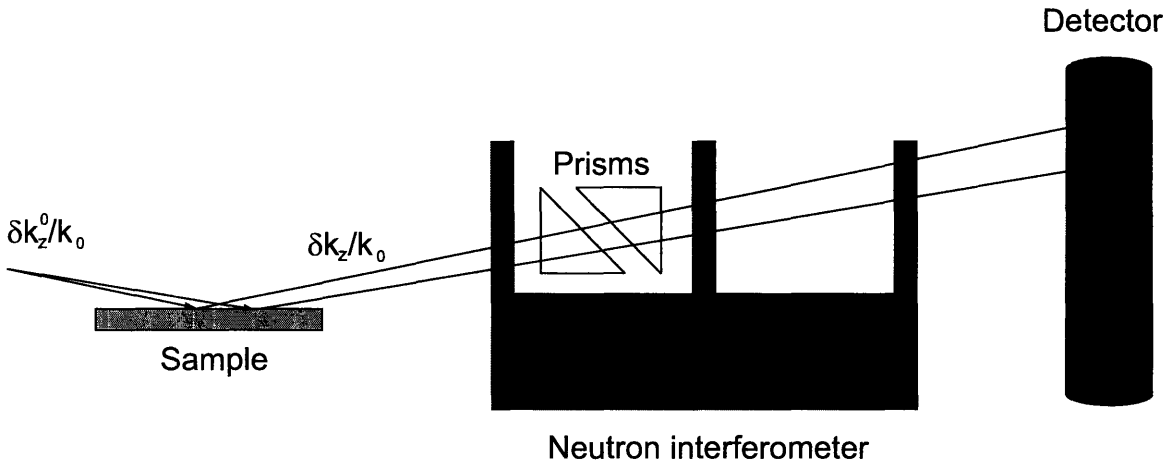

Figure 4-7: Proposed Fourier spectroscopy experiment [40]. The sample will modify k_z spectrum input of the interferometer. Both spectra (with or without the sample) are then measured using a coherence length measurement setup. The contrast of the of the interferometer versus Δz is proportional to the Fourier spectrum of the neutron vertical momentum distribution.

Chapter 5

New Interferometer Design insensitive to the Low Frequency Vibrations

5.1 Introduction

Single crystal neutron interferometers are extremely sensitive to environmental noise, including vibrations. Sensitivity is a result of 1) many wavelengths combined in interferometer, 2) slow velocities of neutrons, 3) long measurements times. Most neutron interferometers require vibration isolation, which is usually a big and massive system (especially for low frequency vibrations). Here we propose a new geometry of neutron interferometer design, which will be less sensitive to slow vibrations. Not only will this design improve the interferometer contrast but it will also make it easier to adopt the use of it in many systems.

5.2 Interferometer Schematic

Figure 5-1 **A**) shows a schematic diagram of a 3-blade (LLL-type) neutron interferometer. The neutron beam coming from the left is coherently split into two paths by the first blade via Bragg scattering. After being reflected by the second blade, these two paths are recombined at the third blade. The resultant interference is observed at the O or H detectors. Note that we align the y coordinate parallel to the Bragg

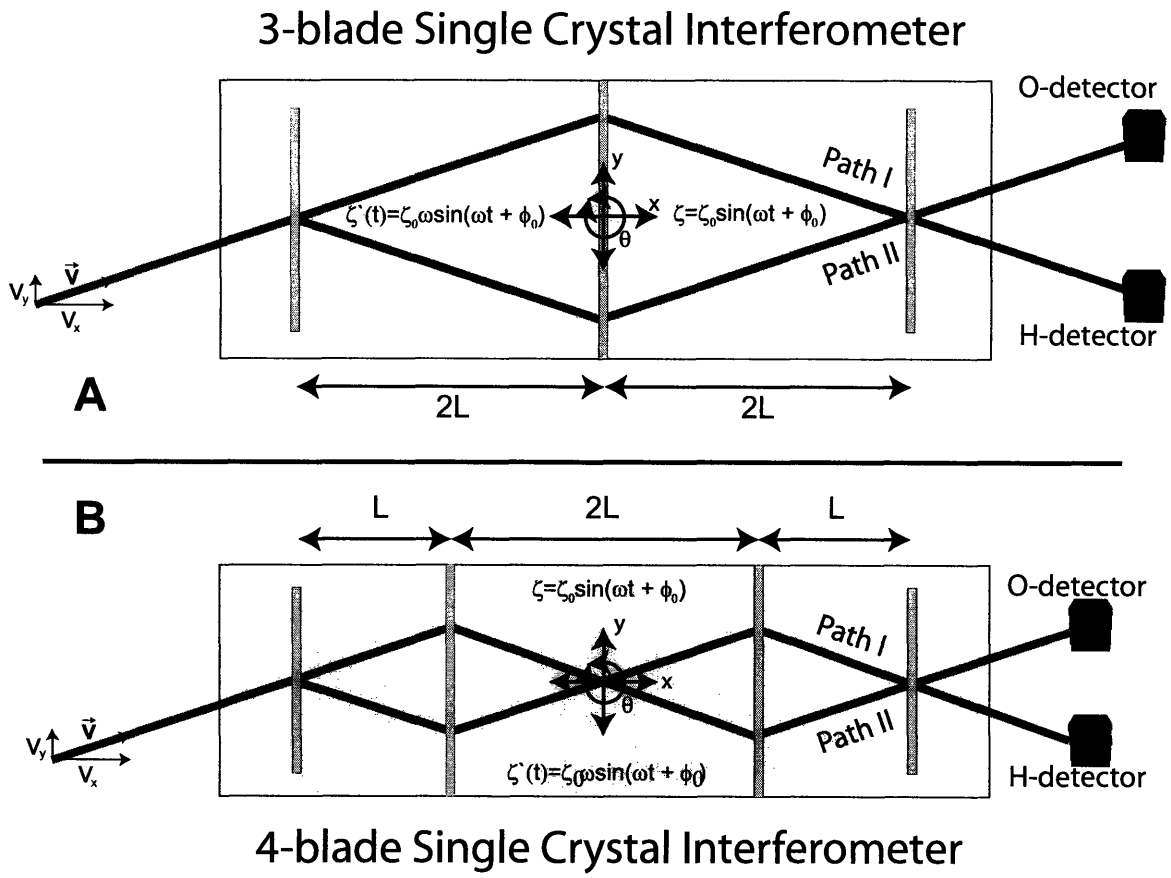

Figure 5-1: **A**: A schematic diagram of the 3-blade neutron interferometer. A neutron beam (with neutron velocity $\vec{v}$) comes from the left, is split by the first blade, is diffracted on the second blade, and recombines at the third. After passing through the interferometer, the beam is captured by the O and H detectors. We model vibrations as oscillations of/around the center of mass of the interferometer, as $\zeta(t) = \zeta_0 \sin(\omega t + \varphi)$, where ζ could be y - transverse vibrations, x - longitudinal, and θ - rotation. In order to compare oscillations between 3 and 4 blades devices, the distance between the blades is set equal to $2L$. **B**: A schematic diagram of the proposed interferometer with 4 blades. Instead of one diffracting blade here we have two, which reverses neutron paths in order to compensate for vibrations. We use the same vibration modes with the same amplitudes as in case of 3-blade interferometer.

planes and the x coordinate is perpendicular to the Bragg planes.

We consider vibrations as sinusoidal oscillations around the center of mass of the single crystal which we write as

$$\zeta(t) = \zeta_0 \sin(\omega t + \varphi). \tag{5.1}$$

As ζ we could use any coordinates x, y, z, or any angles (such as θ - rotation around z axis). In order to motivate the discussion we adopt a simple model for the neutron/blade interaction. The interaction is that of bouncing of the small particle (neutron) from a moving heavy wall (the blade) if the particle reflected. When the particle is transmitted there is no interaction (figure 5-2). We use conservation of momentum and energy to calculate the neutron's change of velocity after bouncing. We require a small enough amplitude and low enough oscillation frequency that the modified momentum of the neutron still satisfies Bragg's conditions, and that the scattered amplitude does not change significantly[1]. Vibrations modify the neutron velocities and change the path length of the neutron inside the interferometer.

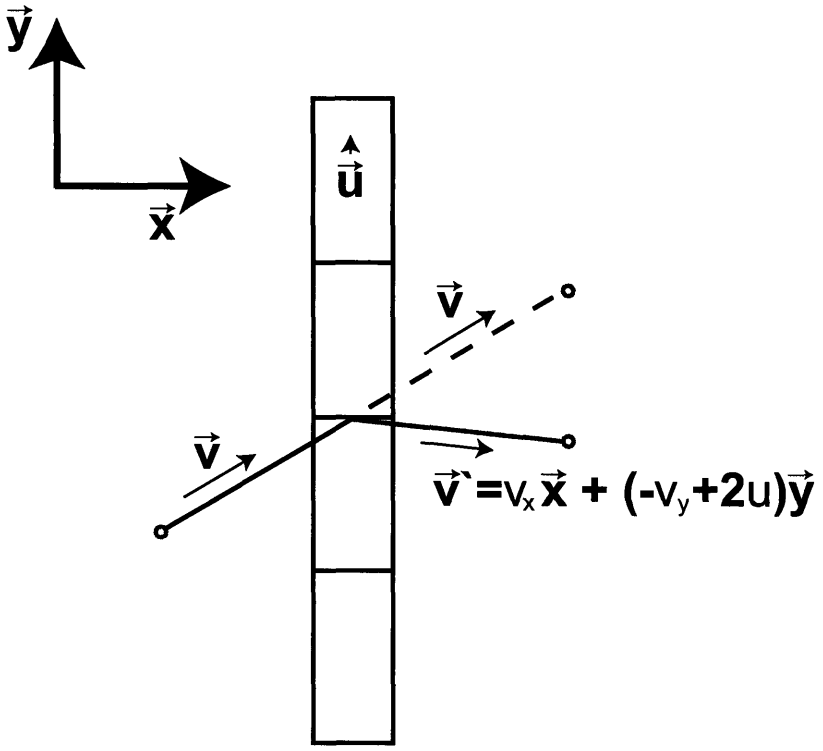

Figure 5-2: A schematic diagram of the neutron scattering from the blade. Due to the crystal movement, the reflected neutron will change its momentum. For the transmitted case, the momentum remains unaltered.

Using these approximations, it is clear that vibrations along every axis except the

[1]i.e. all angles are inside crystal acceptance angle, the Darwin width, that is defined as the value at which the reflected intensity as a function of the off-Bragg angle falls to half its maximum value and which is calculated from dynamical diffraction theory as $\Delta\theta_{Darwin} = \frac{4\pi F_G}{k^2 V_{cell} \sin(2\theta_{Bragg})} < 1$ arcsec, where F_G is Bravais lattice structure factor and V_{cell} is the volume of the unit cell.

z coordinate will reduce the interferometer contrast. The z-component of neutron velocity and the paths lengths are independent of crystal vibration along the z axis.

Considering vibrations along the y axis and looking back to figure 5-1, there is a loss in the contrast because the variation in neutron momentum results in the 2 paths being displaced from each other at the last blade. The loss in contrast is from the asymmetry of the paths with respect to the vibrations. The 4-blade interferometer makes the 2 paths symmetric and preserves the contrast. It is revealing to view the recovery of contrast as an example of the quantum error correction. Consider the 5-blade interferometer setup shown in figure 5-3.

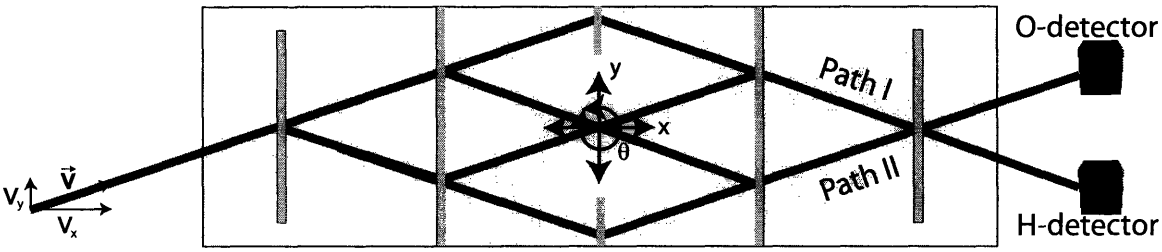

Figure 5-3: The outer two have the same sensitivity to vibrations as does the3-blade interferometer and the inner two paths are insensitive to vibrations

Here we see that there are four paths: the outer two have the same sensitivity to vibrations as the 3-blade interferometer, and the inner two paths are insensitive to vibrations.

5.3 Vibrations along the y axis

We first consider vibrations along the y axis. The measure of the quality of the interferometer is it's contrast, so we plot the contrast versus the frequency of oscillations.

In order to compare results for the 3 and 4 blade interferometers, we take interferometers with similar path lengths: therefore we choose the length between the blades of the 3-blade interferometer to be $2L$.

5.3.1 3-blade interferometer

Assume that the neutron hit the 1^{st} blade of interferometer at the time $t = 0$. We rewrite equation 5.1 for vibrations along y axis where ϕ is a random phase between the arriving neutron and the vibrating blade.

$$y(t) = y_0 \sin(\omega t + \varphi). \tag{5.2}$$

The velocity of the interferometer at the time t is

$$u_y(t) = \frac{dy(t)}{dt} = y_0\omega \cos(\omega t + \varphi). \tag{5.3}$$

At time $t = 0$, the velocity of the interferometer along the y-coordinate is $u_y(0) = y_0\omega \cos\varphi$, where φ is random. Conservation of momentum and energy at the moment $t = 0$ implies that the velocity of the transmitted neutron do not change, while the reflected neutron is $\vec{v}_{refl}(0+) = v_x\hat{\mathbf{x}} - (v_y - 2u_y(0))\hat{\mathbf{y}}$.

The phase difference for the neutron between path I and path II is

$$\Delta\Phi = \Phi(path\ II) - \Phi(path\ I) = \frac{1}{\hbar}\int_{path\ II} \mathbf{p}d\mathbf{s} - \frac{1}{\hbar}\int_{path\ I} \mathbf{p}d\mathbf{s}, \tag{5.4}$$

where $\mathbf{p}$ is momentum of the neutron and $\mathbf{s}$ is the path-length vector along which the neutron is moving.

For the neutron to travel between the first 2 blades takes time a $t = 2L/v_x = 2\tau$. Conservation at the second blade and our single model shows that the phase acquired by the neutron traveling between the first and the second blade in the path I is

$$\Phi(path\ I : 1 \rightarrow 2) = \frac{m_n}{\hbar} v\sqrt{(2L)^2 + (v_y 2\tau)^2} = \frac{m_n}{\hbar} v^2 2\tau \tag{5.5}$$

and in path II is

$$\Phi(path\ II : 1 \rightarrow 2) = \frac{m_n}{\hbar}\sqrt{v_x^2 + (v_y - 2u_y(0))^2}\sqrt{(2L)^2 + ((v_y - 2u_y(0))2\tau)^2}, \tag{5.6}$$

where m_n is the mass of the neutron.

Following the neutron between the second and the third blades we have

$$\Phi(path\ I : 2 \rightarrow 3) = \frac{m_n}{\hbar}\sqrt{v_x^2 + (v_y - 2u_y(2\tau))^2}\sqrt{(2L)^2 + ((v_y - 2u_y(2\tau))2\tau)^2}, \quad (5.7)$$

$$\Phi(path\ II : 2 \rightarrow 3) = \frac{m_n}{\hbar}\sqrt{v_x^2 + (v_y - 2u_y(0) + 2u_y(2\tau))^2} \times \sqrt{(2L)^2 + ((-v_y + 2u_y(0) - 2u_y(2\tau))2\tau)^2}. \quad (5.8)$$

The contrast depends on the total phase difference between the paths equation 5.4 is the sum of equations 5.6 and 5.8 minus equations 5.5 and 5.7:

$$\Delta\Phi(\varphi) = \Phi(path\ II : 1 \rightarrow 2) + \Phi(path\ II : 2 \rightarrow 3) - (\Phi(path\ I : 1 \rightarrow 2) + \Phi(path\ I : 2 \rightarrow 3)). \quad (5.9)$$

Notice that under these assumption the two paths cross the third blade at the same spot and the travel time along these paths will remain 4τ. So, the loss in contrast seen in the presence of vibration is not due to the finite coherence length of the interferometer but rather is due to the extra phase shifts introduced by the vibrations.

Substituting in 5.9 expressions 5.5 - 5.8 we find

$$\Delta\Phi(\varphi) = 16\frac{m_n}{\hbar}\tau\,(v_y - u_y(0))\,(u_y(2\tau) - u_y(0)). \quad (5.10)$$

If we assume that $u_y(t)$ is slowly varying on the scale of 2τ (or $\omega\tau \ll 1$) we can approximate expression $(u_y(2\tau) - u_y(0))$ as a derivative of $u_y(t)$

$$\Delta\Phi(\varphi) = 16\frac{m_n}{\hbar}\tau^2\,(v_y - u_y(0))\,2\left.\frac{du_y(t)}{dt}\right|_{t=\tau}. \quad (5.11)$$

The intensity at the O-detector is

$$I_O(\phi) = 1 + \cos\left(\Delta\Phi(\varphi) + \phi\right) \quad (5.12)$$

and depends on the random phase φ of vibration. We average this intensity over the random phase:

$$\overline{I_O(\phi)} = \int_0^{2\pi} (1 + \cos(\Delta\Phi(\varphi) + \phi))\, d\varphi \tag{5.13}$$

The contrast C is usually defined as

$$C = \frac{\max\{\overline{I(\phi)}\} - \min\{\overline{I(\phi)}\}}{\max\{\overline{I(\phi)}\} + \min\{\overline{I(\phi)}\}}. \tag{5.14}$$

In figure 5-4, the dependance of the contrast C_y on the frequency of vibrations along the y-axis for the 3-blade interferometer is shown as a straight thin blue line. The contrast was calculated for $L = 5$ cm, a neutron velocity of $v = 2000$ m/s, and vibration amplitudes of $y_0 = 0.1$ μm. Here we observe that the contrast starts to decrease near 100 Hz.

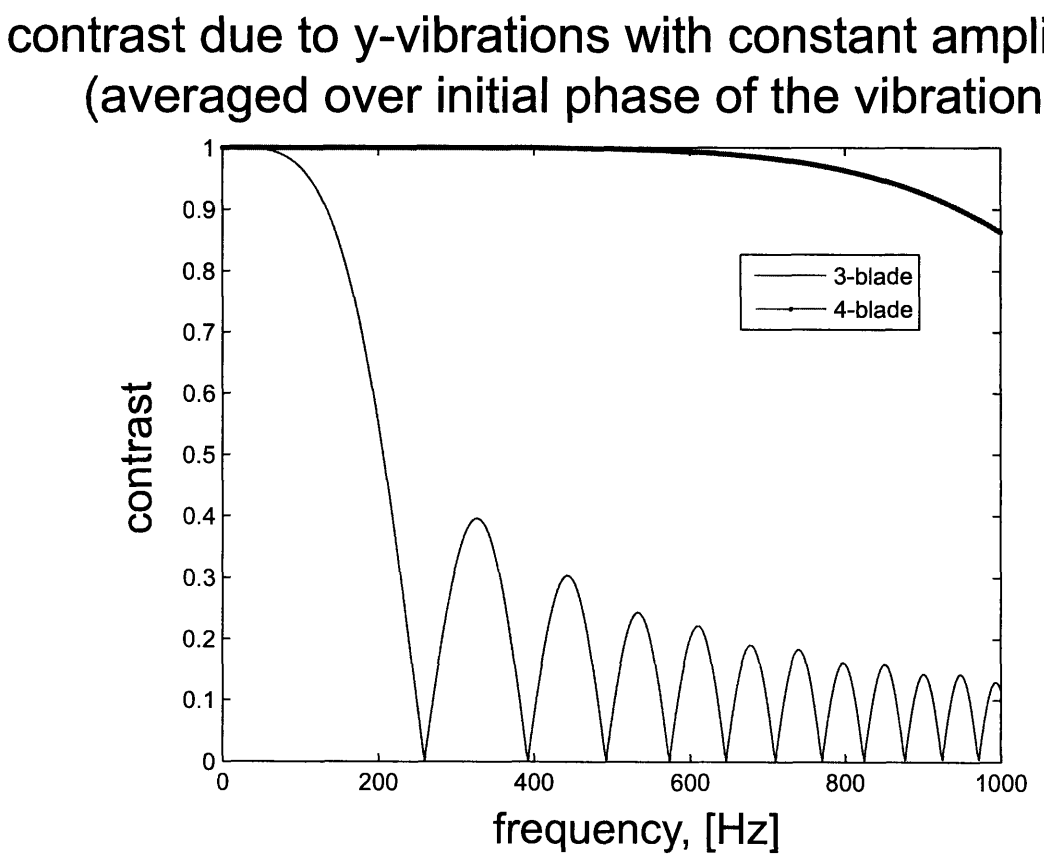

Figure 5-4: Contrast due to vibrations along the y-axis.

We repeat the calculation to see how these vibrations (along y axis) will affect the

new proposed device.

5.3.2 4-blade interferometer

As in the previous case (3-blade interferometer), we derive experiment for the phases the neutron acquires while traveling along the two interferometer paths. Here, the time for the neutron to travel between the first two blades is $\tau = L/v_x$.

Between the first blade and the second, the phases are identical to the 3-blade interferometer except $2L$ changes to L:

$$\Phi(path\ I : 1 \rightarrow 2) = \frac{m_n}{\hbar} v \sqrt{L^2 + (v_y \tau)^2}, \tag{5.15}$$

$$\Phi(path\ II : 1 \rightarrow 2) = \frac{m_n}{\hbar} \sqrt{v_x^2 + (v_y - 2u_y(0))^2} \sqrt{L^2 + ((v_y - 2u_y(0))\tau)^2}, \tag{5.16}$$

For the neutron traveling between the second and the third blades,

$$\Phi(path\ I : 2 \rightarrow 3) = \frac{m_n}{\hbar} \sqrt{v_x^2 + (v_y - 2u_y(\tau))^2} \sqrt{(2L)^2 + ((v_y - 2u_y(\tau))\tau)^2}, \tag{5.17}$$

$$\begin{aligned} \Phi(path\ II : 2 \rightarrow 3) = \frac{m_n}{\hbar} &\sqrt{v_x^2 + (v_y - 2u_y(0) + 2u_y(\tau))^2} \times \\ &\sqrt{(2L)^2 + ((-v_y + 2u_y(0) - 2u_y(\tau))\tau)^2}. \end{aligned} \tag{5.18}$$

Finally, for the paths between the third and the fourth blades:

$$\begin{aligned} \Phi(path\ I : 3 \rightarrow 4) = \frac{m_n}{\hbar} &\sqrt{v_x^2 + (-v_y + 2u_y(0) - 2u_y(\tau) + 2u_y(3\tau))^2} \\ &\sqrt{L^2 + ((-v_y + 2u_y(0) - 2u_y(\tau) + 2u_y(3\tau))\tau)^2}, \end{aligned} \tag{5.19}$$

$$\begin{aligned} \Phi(path\ II : 3 \rightarrow 4) = \frac{m_n}{\hbar} &\sqrt{v_x^2 + (v_y - 2u_y(\tau) + 2u_y(3\tau))^2} \times \\ &\sqrt{L^2 + ((v_y - 2u_y(\tau) + 2u_y(3\tau))\tau)^2}. \end{aligned} \tag{5.20}$$

Overall the phase difference between path II and path I is

$$\Delta\Phi(\varphi) = \Phi(path\ II : 1 \rightarrow 2) + \Phi(path\ II : 2 \rightarrow 3) + \Phi(path\ II : 3 \rightarrow 4) - \left(\Phi(path\ I : 1 \rightarrow 2) + \Phi(path\ I : 2 \rightarrow 3) + \Phi(path\ I : 3 \rightarrow 4)\right), \quad (5.21)$$

or

$$\Delta\Phi(\varphi) = 8\frac{m_n}{\hbar}\tau\left(u_y(0) - v_y\right)\left(2u_y(0) - 3u_y(\tau) + u_y(3\tau)\right). \quad (5.22)$$

Again as for the case of 3-blade interferometer we assume that the function $u_y(t)$ is slowly varying on the scale of τ (or $\omega\tau \ll 1$) and we rewrite the phase change in terms of a derivative

$$\begin{aligned}\Delta\Phi(\varphi) &= 16\frac{m_n}{\hbar}\tau^2\left(v_y - u_y(0)\right)\left[\left.\frac{du_y(t)}{dt}\right|_{t=\frac{\tau}{2}} - \left.\frac{du_y(t)}{dt}\right|_{t=2\tau}\right] = \\ &16\frac{m_n}{\hbar}\tau^3\left(v_y - u_y(0)\right)\frac{3}{2}\left.\frac{du_y^2(t)}{d^2t}\right|_{t=\frac{5\tau}{4}}. \end{aligned} \quad (5.23)$$

Notice that the linear term drops out. The contrast comparison we make is the O-beam of the 3-blades interferometer to the H-beam of the 4-blade interferometer. In both cases the neutrons arrive at the detector after exactly 2 reflections. The intensity at the H-detecto is

$$I_H(\phi) = 1 + \cos\left(\Delta\Phi(\varphi) + \phi\right) \quad (5.24)$$

and depends on the random phase φ of vibration. Again we average the intensity over this random phase:

$$\overline{I_H(\phi)} = \int_0^{2\pi}\left(1 + \cos\left(\Delta\Phi(\varphi) + \phi\right)\right)d\varphi. \quad (5.25)$$

Now we can obtain the contrast using equation 5.14. In figure 5-4 we plot the frequency dependance of the contrast for the 4-blade interferometer. Also again notice that *paths I* and *II* cross the fourth blade at the same spot. From figure 5-4 we

clearly see that the 4-blade interferometer is predicted to be much less sensitive for y-vibrations. Let's now consider vibrations along the x-axis.

5.4 Vibrations along the x axis

In case of vibrations along the x axis the momentum of the neutron is not modified (see figure 5-2). However the paths length changes depending on the phase φ of the oscillations at $t = 0$.

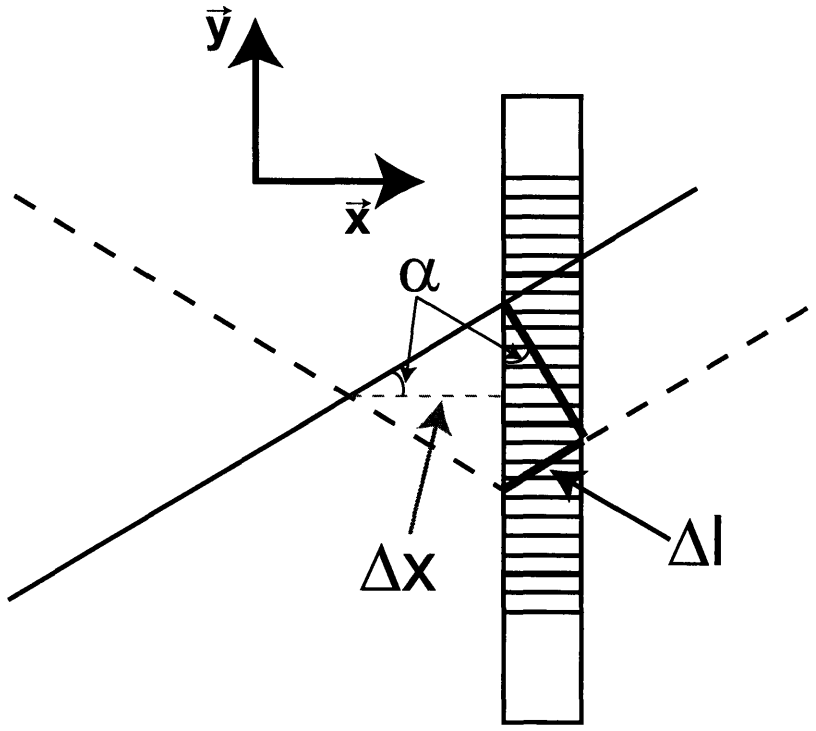

Figure 5-5: A schematic diagram of the neutron arriving to the third blade. Due to the crystal movement, the paths of the neutron will not recombined at the ideal point but at Δx away from the third blade.

The vibrations along the x-axis are

$$x(t) = x_0 \sin(\omega t + \varphi). \tag{5.26}$$

In this case the phase shift is due to the paths crossing at a point displaced from ideal as shown in figure 5-5. Once we find Δx for each interferometer, then $\Delta l =$

$2 * \Delta x \tan\alpha \sin\alpha$ and the phase difference is

$$\Delta\Phi(\varphi) = \frac{m_n}{\hbar} v \Delta l. \tag{5.27}$$

For the 3-blade interferometer, we have $\tau = L/v_x$ and

$$\Delta x \approx x(4\tau) - 2x(2\tau) + x(0), \tag{5.28}$$

where we neglect distance $x(2\tau) - x(0)$ ($< 1\mu$m) in comparison with L (> 1cm). For the 4-blade interferometer

$$\Delta x = x(4\tau) - 4x(\tau) + 3x(0). \tag{5.29}$$

Using these Δx we can get $\Delta\Phi$, substitute these $\Delta\Phi$ to find intensities, and average intensity over different φ to obtain the contrasts.

Figure 5-6 shows the contrast dependance on the frequency of vibrations along the x-axis, where the blue straight line shows the 3-blade dependance and the thick green line represents the 4-blade interferometer. In this case the vibrations are limited by coherence length of $\frac{1}{\Delta k_z}$.

5.5 Rotation around the z axis

This effect is expected to be most limiting since the neutron interferometer has such a small acceptance angle. In the case of rotational vibrations, we rewrite the oscillation in terms of the angle θ around the z-axis

$$\theta(t) = \theta_0 \sin(\omega t + \varphi). \tag{5.30}$$

For small angles, rotational vibrations can be considered as translational vibrations, i.e. $\Delta r = r * \theta$, where r is the distance from the blade to the center of rotation.

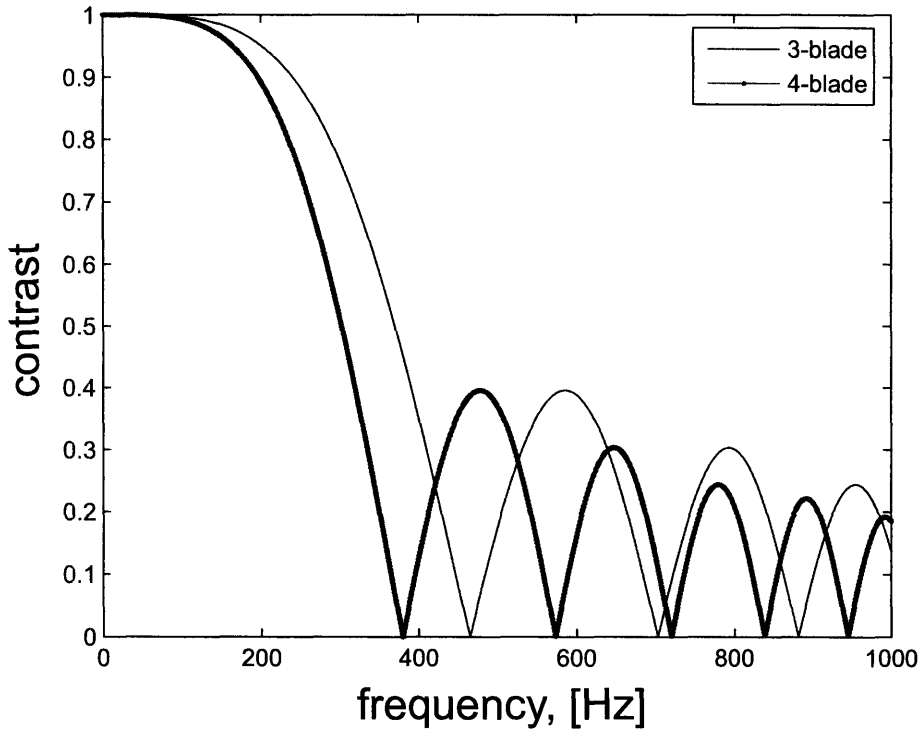

Figure 5-6: Contrast due to vibrations along the x-axis.

5.5.1 3-blade interferometer

In the 3-blade interferometer, the center of rotation is also the center of mass and the center of the middle blade. For the point (see figure 5-1 **A**)) where the neutron path crosses the blades, the rotational vibrations can be modeled as vibration along the y-axis for the first and last blade and along the x-axis for the path crossing the middle blade. In this case, the interaction with the middle blade does not change the velocity of the neutron. At the first blade we have a change in the momentum of the reflected beam and no change for transmitted

$$\vec{v}_{path\ I}(t = 0+) = v_x\hat{\mathbf{x}} + v_y\hat{\mathbf{y}}, \tag{5.31}$$

$$\vec{v}_{path\ II}(t = 0+) = v_x\hat{\mathbf{x}} + (-v_y + 2u1_y(0))\hat{\mathbf{y}}, \tag{5.32}$$

where $u1_y(t) = 2L\theta_0 \sin(\omega t + \varphi)$ velocity of the first blade in the $\hat{\mathbf{y}}$ direction.

The phase difference between the two paths is

$$\Delta\Phi(\varphi) = \Phi(path\ II) - \Phi(path\ I) = \frac{m_n}{\hbar}\left[|\vec{v}_{path\ I}|^2 - |\vec{v}_{path\ II}|^2\right] 4\tau = \frac{m_n}{\hbar}\left[(v_x^2 + v_y^2 - 4u1_y(0)v_y + (2u1_y(0))^2 - v_x^2 - v_y^2\right] 4\tau = 8\frac{m_n}{\hbar} L\theta_0\omega \sin\varphi\,[2L\theta_0\omega \sin\varphi - v_y]\,4\tau, \quad (5.33)$$

where $\tau = L/v_x$.

Substituting this difference in phase into equation 5.12 for the O-beam intensity and averaging, we find the frequency dependance of the contrast equation 5.14. In figure 5-7 this contrast for the 3-blade system is shown as a blue straight line. As an amplitude of vibrations θ_0 we used 1 μrad.

Let's see what happens in the 4-blade system.

5.5.2 4-blade interferometer

In the 4-blade interferometer the center of rotation and the center of mass coincide between the blades. For points (see figure 5-1 **B**)) where the neutron path crosses the blades, the rotational vibrations are modeled as vibrations along the y axis. As in the 3-blade case the v_x component of the neutron velocity does not change. The velocities are modified as, Path I:

$$v_y(I: 1 \to 2) = v_y, \quad (5.34)$$

$$v_y(I: 2 \to 3) = -v_y + 2\sqrt{L^2 + (v_y\tau)^2}\,\theta_0\omega \cos(\omega\tau + \varphi), \quad (5.35)$$

$$v_y(I: 3 \to 4) = v_y - 2\sqrt{L^2 + (v_y\tau)^2}\,\theta_0\omega\left[\cos(\omega\tau + \varphi) + \cos(\omega 3\tau + \varphi)\right], \quad (5.36)$$

where $\tau = L/v_x$ and the sign of the last cosine term is positive because the oscillations of the 2^{nd} and the 3^{rd} blades have π phase shift difference.

Path II:

$$v_y(II: 1 \to 2) = v_y + 2\theta_0\omega 2L\cos\phi, \quad (5.37)$$

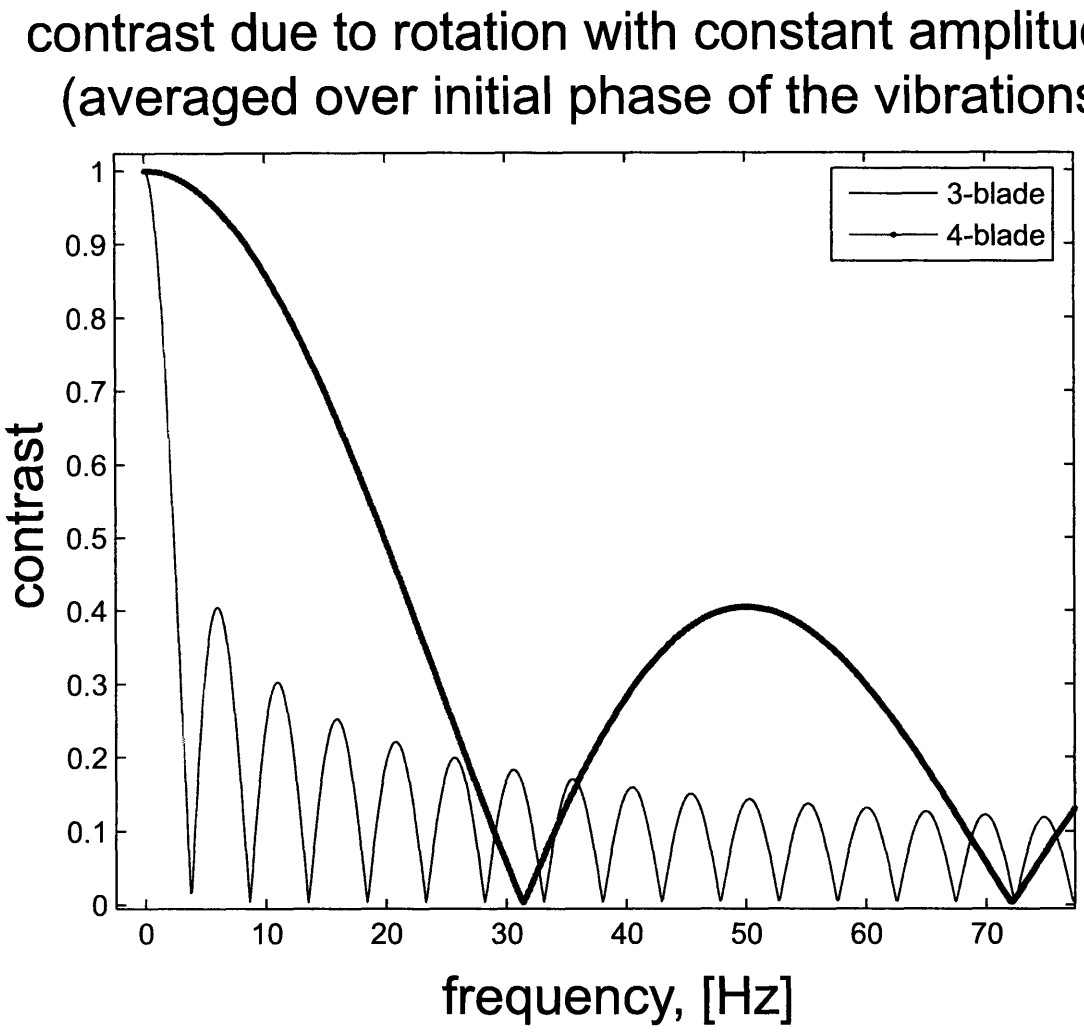

Figure 5-7: Contrast due to rotational vibrations θ around z-axis and the center of mass.

$$v_y(II:2\rightarrow 3) = -v_y(II:1\rightarrow 2)+2\sqrt{L^2+(v_y\tau)^2}\theta_0\omega\cos(\omega\tau+\varphi), \quad (5.38)$$

$$v_y(II:3\rightarrow 4) = -v_y(II:2\rightarrow 3)-2\sqrt{L^2+(v_y\tau)^2}\theta_0\omega\cos(\omega 3\tau+\varphi). \quad (5.39)$$

The phases along each path are

Path I:

$$\Phi(I:1\rightarrow 2) = \frac{m_n}{\hbar}v^2\tau, \quad (5.40)$$

$$\Phi(I:2\rightarrow 3) = \frac{m_n}{\hbar}(v_x^2+v_y(I:2\rightarrow 3)^2)2\tau, \quad (5.41)$$

$$\Phi(I:2\rightarrow 3) = \frac{m_n}{\hbar}(v_x^2+v_y(I:3\rightarrow 4)^2)\tau. \quad (5.42)$$

Path II:

$$\Phi(II:1\rightarrow 2) = \frac{m_n}{\hbar}(v_x^2+v_y(II:1\rightarrow 2)^2)\tau, \quad (5.43)$$

$$\Phi(II:2\rightarrow 3) = \frac{m_n}{\hbar}(v_x^2+v_y(II:2\rightarrow 3)^2)2\tau, \quad (5.44)$$

$$\Phi(II:2\rightarrow 3) = \frac{m_n}{\hbar}(v_x^2+v_y(II:3\rightarrow 4)^2)\tau. \quad (5.45)$$

The phase difference is

$$\Delta\Phi(\varphi) = \Phi(II:1\rightarrow 2)+\Phi(II:2\rightarrow 3)+\Phi(II:3\rightarrow 4)- \\ (\Phi(I:1\rightarrow 2)+\Phi(I:2\rightarrow 3)+\Phi(I:3\rightarrow 4)). \quad (5.46)$$

As before, we can find the I_H intensity at the H-detector, average it over the random phase φ, and extract the contrast. This contrast dependance on the frequency of rotational vibrations is plotted as a thick green line in figure 5-7. We see that for these rotations the 4-blade interferometer design is significantly more robust then is the 3-blade.

5.6 Conclusion

Vibrations we use in our simulations (with amplitude 10^{-7}m in translation) produce change in the incident angle of the neutron much less then the acceptance angle of the crystal ($\ll 5\times 10^{-6}$rad) and of the similar order for 50Hz frequency range as measured in ref. [28]. In order to exceed the acceptance angle the amplitude of vibrations should be bigger then 50μm.

Let's note that the small angle vibrations around the x-axis will be similar to the translational vibrations along the y-axis, and the small angle vibrations around y will be similar to the translational vibrations along x. As we mentioned before, the vibrations along the z-axis do not influence the contrast.

All together results of vibration consideration bring us to the new experimental geometry for the neutron interferometer.

Chapter 6

Future Prospectives for Neutron Interferometry.

Here we have shown (Chapter 5) a new design geometry for neutron interferometry that is less sensitive to vibrations. Given such a design we can now redesign the entire neutron interferometer setup to remove the need for the extreme multi-stage vibration isolation system and perhaps even extend the temperature stability. Such a new design would allow greater access to neutron interferometry and permit the use of neutron interferometer for new applications and fundamental experimental studies. In particular, since the new design would be much more compact, it could be moved closer to the beam break and thus have greater neutron intensities. Increasing the neutron flux will increase the signal-to-noise ratio which allows for trade-offs to narrow the momentum distribution (or to have a better collimated beam). One result of such a trade-off is to increase the neutron coherence length, particularly in the vertical direction. An additional advantage of moving the interferometer closer to the beam break would be to reduce neutron losses and better maintain the monochromator-selected neutron momentum distribution due to the decreased scattering in the shorter beam paths.

Expanding the coherence length of the interferometer permits material study over length-scales that are not easily accessible by other approaches. Such experiments include Fourier Spectroscopy and Reflectometry [40] (proposed experimental setup

is shown on figure 4-7). These experiments use the unique properties of a neutron interferometer, where the contrast function due to the vertical path separation inside the interferometer is the coherence function and proportional to the Fourier transform of the vertical momentum distribution of the accepted neutron beam. For example, a sample placed in front of the interferometer will modify the neutron momentum distribution. When compared to the neutron momentum distribution without the sample, the change in momentum is easily measured. This method does not require complicated models in order to extract reflectivity curves.

In this thesis we introduced a complete and systematic description of the neutron wave-function (density matrix) inside the neutron interferometer. Modeling this system thoroughly provides new insights to new implementations and applications of the neutron interferometer. One of such examples which we believe will lead is a reciprocal space neutron imaging described in Chapter 3. Here we introduce spatial coherence on the beam profile, encode the neutron beam with a phase gradient, compare the encoded beam with the beam modified by a sample by interference, and measure the Fourier components of the spatial phase distribution due to the sample by result of interference. This new technique does not require the use of a position sensitive neutron detector. This method has the potential to improve the spatial resolution of existing imaging methods.

As a result of the coherent scattering length experiment we discovered that the interferometer output neutron beam can be prepared as a coherent superposition of two beams with the same momentum properties but separated in a well controlled manner. Using this coherent neutron beam as the input state for a second interferometer we can develop new methods to measure the auto-correlation function of a sample placed in one path of the second interferometer. The separation control device would be replicated in the second path of the second interferometer permitting the difference in the phase over the displaced beam to be coherently measured. In this case the measured contrast will be proportional to the auto-correlation function of the sample scattering function. This way we can move neutron scattering experiments up to μm length-scales which are not easily accessible today.

Appendix A

Calculation of the phase and the vertical displacement of the neutron beam due to the prisms

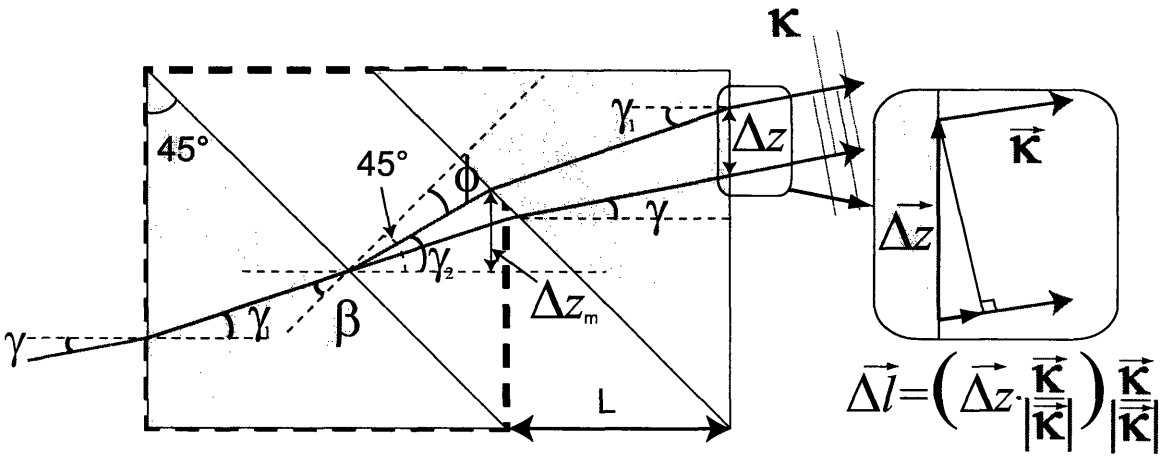

Figure A-1: A schematic diagram of the neutron paths through the prisms. The neutron beam enters from the left and depending on the separation between the prisms is shifted vertically. The angles shown on the figure corresponds to the calculations for path separation and phase shifts of the neutron described in the text.

Let's calculate related phase shifts and vertical displacements. We are going to consider two sets of prisms one set in each neutron interferometer path. Both sets in the connected state (when the distance between prisms is equal to zero) form a cube.

The index of refraction of the prisms is n and is very close to zero. Let's define it as

$$n = 1 - \Delta n. \tag{A.1}$$

From the figure A-1 and the fact that the base of the prisms has a right angle we have

$$45^\circ = \gamma_2 + \phi, \tag{A.2}$$

$$45^\circ + 90^\circ - \gamma_1 + 90^\circ - \beta = 180^\circ \Rightarrow \beta = 45^\circ - \gamma_1. \tag{A.3}$$

Snell's law for our prisms

$$\sin\gamma = n\sin\gamma_1, \tag{A.4}$$

$$n\sin(45^\circ - \gamma_1) = \sin(45^\circ - \gamma_2) \tag{A.5}$$

Using this we can easily find Δz_m (see figure A-1), the vertical displacement of the beam in between prisms due to separation L

$$\Delta z_m = L\frac{\cos 45^\circ}{\cos\phi}\sin\gamma_2 = L\frac{\tan\gamma_2}{1+\tan\gamma_2}. \tag{A.6}$$

Than Δz total vertical displacement due to the both sets of the prisms is

$$\Delta z = \Delta z_2 - \Delta z_1 = (\Delta z_m + (d + \Delta z_m)\tan\gamma_1) - (d\tan\gamma_1 + L\tan\gamma),$$

$$\Delta z = \Delta z_m(1+\tan\gamma_1) - L\tan\gamma, \tag{A.7}$$

where d is height of the prism, Δz_1 and Δz_2 are the displacement of the beam in path I and path II.

And the phase shift due to the both sets of prisms is

$$\Delta\Phi = \Phi_2 - \Phi_1 = \left(k_0 n\frac{d+\Delta z_m}{\cos\gamma_1} + k_0 L\frac{\cos 45^\circ}{\cos\phi}\right) - \left(k_0 n\frac{d}{\cos\gamma_1} + k_0\frac{L}{\cos\gamma}\right) \tag{A.8}$$

where k_0 is the incident momentum of the neutron, Φ_1 and $|Phi_2$ are phases due to

set of prisms in path I or path II correspondingly.

We can simplify equation (A.8)

$$\Delta\Phi = k_0 n \frac{\Delta z_m}{\cos\gamma_1} + k_0 L \left(\frac{\cos 45^\circ}{\cos(45^\circ - \gamma_2)} - \frac{1}{\cos\gamma} \right). \tag{A.9}$$

We can simplify the results considering small angle approximation. The angles that we have in our system are smaller than 0.5° is a few 10^{-3} rad. Also neutrons are weakly interacting with media and index or refraction is very close to 1 ($\Delta n = 1 - n$ is 10^{-5} - 10^{-6} order of magnitude).

Using the Taylor expansion for equations (A.5) to the second order for γ, the first order for Δn and $\Delta n\gamma$

$$\gamma(1 + \Delta n) = \gamma_1, \tag{A.10}$$

$$\begin{aligned} n(\sin 45^\circ \cos\gamma_1 - \sin\gamma_1 \cos 45^\circ) &= \sin 45^\circ \cos\gamma_2 - \sin\gamma_2 \cos 45^\circ, \\ (1 - \Delta n)(1 - \gamma_1^2/2 - \gamma_1) &= 1 - \gamma_2^2/2 - \gamma_2. \end{aligned} \tag{A.11}$$

Substituting (A.10) into (A.11) and using method of consequent approximations we have

$$\begin{aligned} \gamma_2 &= \gamma + \Delta n - \Delta n\gamma, \\ \gamma_2^2 &= \gamma^2 + 2\Delta n\gamma. \end{aligned} \tag{A.12}$$

In the next step let's find Δz_m. Using equation (A.6) we have

$$\Delta z_m = L\gamma_2(1 - \gamma_2 + \gamma_2^2/2) = L(\gamma_2 - \gamma_2^2). \tag{A.13}$$

Now applying (A.13) we get

$$\Delta z_m = L(\gamma + \Delta n - 3\Delta n\gamma - \gamma^2). \tag{A.14}$$

Using this equation A.14 and equation A.7 we can find a approximate result for

the displacement of the beam Δz in the different paths of interferometer due to the prisms.

$$\begin{aligned} \Delta z &= L\left[(1+\gamma+\gamma\Delta n)(\gamma+\Delta n-3\Delta n\gamma-\gamma^2)-\gamma\right], \\ \Delta z &= L\Delta n(1-2\gamma). \end{aligned} \tag{A.15}$$

In order to calculate the phase difference due to the prisms $\Delta\Phi$ for simplicity let's split equation (A.9) into two parts:

$$\Delta\Phi = A + B, \tag{A.16}$$

where

$$A = k_0 n \frac{\Delta z_m}{\cos\gamma_1}, \tag{A.17}$$

$$B = k_0 L\left(\frac{\cos 45^\circ}{\cos(45^\circ-\gamma_2)} - \frac{1}{\cos\gamma}\right). \tag{A.18}$$

Substituting values for Δz_m, n, γ_1, and γ_2 we find

$$\frac{A}{k_0 L} = (1-\Delta n)(1+\gamma_1^2/2)(\gamma+\Delta n-3\Delta n\gamma-\gamma^2), \tag{A.19}$$

$$\frac{B}{k_0 L} = \frac{1/\sqrt{2}}{1/\sqrt{2}\cos\gamma_2 + 1/\sqrt{2}\sin\gamma_2} - \frac{1}{1-\gamma^2}. \tag{A.20}$$

After all substitution and simplification we have

$$\frac{A}{k_0 L} = (\gamma+\Delta n-4\Delta n\gamma-\gamma^2)(1+\gamma^2/2) = \gamma+\Delta n-4\Delta n\gamma-\gamma^2, \tag{A.21}$$

$$\frac{B}{k_0 L} = 3/2\gamma_2^2 - \gamma_2 - \gamma^2/2 = \gamma^2 + 4\Delta n\gamma - \gamma - \Delta n. \tag{A.22}$$

Finally for the phase shift we have

$$\Delta\Phi = A + B = 0. \tag{A.23}$$

Appendix B

Measurements of the Vertical Momentum Distribution

All neutron beams naturally have divergence, thus momentum spread (distribution). Here we describe how we measured vertical momentum distribution in our system.

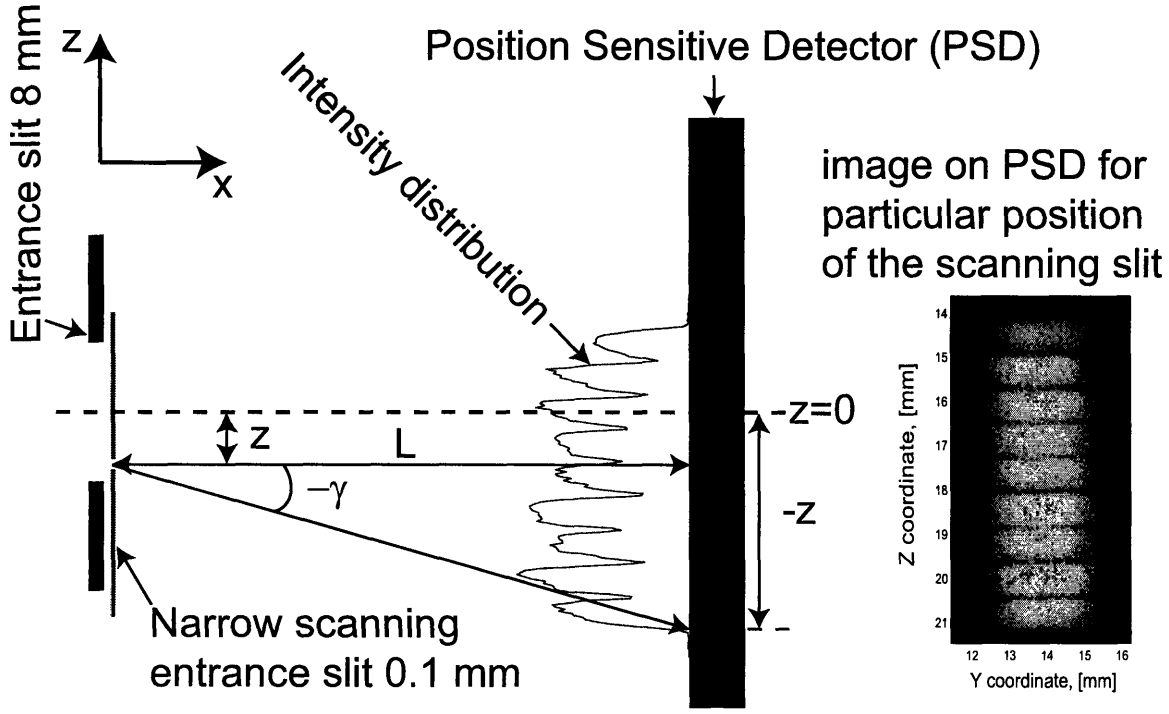

Figure B-1: A schematic diagram of the measurements of neutron vertical momentum distribution.

FigureB-1 reports the schematic diagram for measurements of the vertical mo-

mentum distribution. It consists of entrance 8 mm slit on the left, followed by narrow 100 μm scanning slit, and at some distance L, by a position sensitive detector (PSD) [29]. The narrow scanning slit could be moved vertically and at each position of this slit we record the intensity distribution due to the neutron beam on the PSD. One of such images is shown at the far right of the figure. In the image we clearly see nine humps (or wide peaks). This is due to our second focusing monochromator, which consists of nine pyrolytic graphite blades. The images obtained are converted to the vertical intensity distribution.

Knowing the position of the scanning slit ζ and the vertical intensity distribution of the neutrons we can derive distribution of the neutron angles γ with respect to the horizontal axis. From the figure we can see that

$$\gamma = \tan^{-1}\left[\frac{z-\zeta}{L}\right]. \tag{B.1}$$

Thus from vertical distribution of intensity we get angular distribution $I(\zeta,\gamma)$ for each position of the scanning slit ζ.

Measuring the angular distribution of the neutrons for each position ζ of the scanning slit and integrating over all the positions of the scanning slit (from z_{top}=-4 mm to z_{bottom}=4 mm , of the entrance slit) we will get the overall angular distribution:

$$I(\gamma) = \int_{z_{bottom}}^{z_{top}} I(\zeta,\gamma)d\zeta. \tag{B.2}$$

The angular distribution is very easy to convert to the vertical momentum distribution k_z:

$$k_z = k\sin\gamma, \tag{B.3}$$

where k is the length of the wave-vector of the neutron.

Bibliography

[1] J. Chadwick. Possible existence of a neutron. *Nature*, 129:312, 1932.

[2] W. M. Elsasser. *C. R. Acad. Sci. Paris*, 202:1029, 1936.

[3] H. V. Halban and P. Preiswerk. *C. R. Acad. Sci. Paris*, 203:73, 1936.

[4] D. D. Mitchell and P. N. Powers. *Phys. Rev.*, 50:486, 1936.

[5] H. Maier-Leibnitz and T. Springer. Ein interferometer für langsame neutronen. *Z. Physik*, 167:386, 1962.

[6] F. J. Landkammer. Beugungsversuche mit langsamen neutronen. *Z. Physik*, 189:113, 1966.

[7] F. Mezei. Neutron spin echo: A new concept in polarized thermal neutron techniques. *Z. Physik*, 255:146–160, 1972.

[8] H. Rauch, W. Treimer, and U. Bonse. Test of a single crystal neutron interferometer. *Phys. Lett. A*, 47:369–371, 1974.

[9] W. Bauspiess, U. Bonse, H. Rauch, and W. Treimer. Test measurements with a perfect crystal neutron interferometer. *Z. Physik*, 271:177–182, 1974.

[10] U. Bonse and M. Hart. An x-ray interferometer. *Applied Physics Letters*, 6(8):155–156, 1965.

[11] U. Bonse and H. Rauch. *Neutron Interferometry.* Oxford University Press, 1979.

[12] S. Kikuta, I. Ishikawa, K Kohra, and S. Hoshinor. Studies on dynamical diffraction phenomena of neutrons using properties of wave fan. *J. Phys. Soc. Japan*, 39:471–478, 1975.

[13] A. Zeilinger, C. G. Shull, J. Arthur, and M. A. Horne. Bragg-case neutron interferometry. *Phys. Rev. A*, 28(1):487–489, Jul 1983.

[14] A. I. Ioffe, V. S. Zabiyakin, and G. M. Drabkin. Test of a diffraction grating neutron interferometer. *Phys. Lett.*, 111:373–375, 1985.

[15] H. Funahashi, T. Ebisawa, T. Haseyama, M. Hino, A. Masaike, Y. Otake, T. Tabaru, and S. Tasaki. Interferometer for cold neutrons using multilayer mirrors. *Phys. Rev. A*, 54(1):649–651, Jul 1996.

[16] H. Rauch and S. A. Werner. *Neutron Interferometry.* Oxford University Press, 2000.

[17] V. F. Sears. *Neutron Optics.* Oxford University Press, 1989.

[18] H. Rauch, A. Zeilinger, G. Badurek, A. Wilfing, W. Bauspiess, and U. Bonse. Verification of coherent spinor rotation of fermions. *Phys. Lett. A*, 54:425–427, 1975.

[19] R. Colella, A. W. Overhauser, and S. A. Werner. Observation of gravitationally induced quantum interference. *Phys. Rev. Lett.*, 34(23):1472–1474, Jun 1975.

[20] S. A. Werner, J. L. Staudenmann, and R. Colella. Effect of earth's rotation on the quantum mechanical phase of the neutron. *Phys. Rev. Lett.*, 42(17):1103–1106, Apr 1979.

[21] A. Cimmino, G. I. Opat, A. G. Klein, H. Kaiser, S. A. Werner, M. Arif, and R. Clothier. Observation of the topological aharonov-casher phase shift by neutron interferometry. *Phys. Rev. Lett.*, 63(4):380–383, Jul 1989.

[22] B. E. Allman, A. Cimmino, A. G. Klein, G. I. Opat, H. Kaiser, and S. A. Werner. Scalar aharonov-bohm experiment with neutrons. *Phys. Rev. Lett.*, 68(16):2409–2412, Apr 1992.

[23] G. Badurek, H. Rauch, and D. Tuppinger. Neutron interferometric double-resonance experiment. *Phys. Rev. A*, 34(4):2600–2608, Oct 1986.

[24] A. G. Klein, G. I. Opat, A. Cimmino, A. Zeilinger, W. Treimer, and R. Gähler. Neutron propagation in moving matter: The fizeau experiment with massive particles. *Phys. Rev. Lett.*, 46(24):1551–1554, Jun 1981.

[25] A. G. Wagh, V. C. Rakhecha, J. Summhammer, G. Badurek, H. Weinfurter, B. E. Allman, H. Kaiser, K. Hamacher, D. L. Jacobson, and S. A. Werner. Experimental separation of geometric and dynamical phases using neutron interferometry. *Phys. Rev. Lett.*, 78(5):755–759, Feb 1997.

[26] R. L. Cappelletti, C. J. Ginka, R. A. Lindstrom, J. W. Lynn, H. A. Prask, E. Prince, J. J. Rush, J. M. Rowe, S. K. Satija, B. H. Toby, A. Tsai, and T. J. Udovic. Material research with neutrons at nist. *Journal of Reaserch of the National Institute of Standarts and Technology*, 106(1):187–230, 2001.

[27] R. E. Williams and J. M. Rowe. Developments in neutron beam devices and an advanced cold source fot the nist research reactor. *Physica B*, 311:117–122, 2002.

[28] M. Arif, D. E. Brown, G. L. Greene, R. Clothier, and K. Littrell. Multistage position-stabilized vibration isolation system for neutron interferometry. *Proc. SPIE Int. Soc. Opt. Eng.*, 20-26:2264, 1994.

[29] M. Dietze, J. Felber, K. Raum, and C. Rausch. Intensified ccds as position sensitive neutron detectors. *Nucl. Instr. and Meth. A*, 377:320–324, 1996.

[30] A. Kumar, D. Welti, and R. R. Ernst. *J. Magn. Resonance*, 18:69–83, 1975.

[31] G. Badurek, R. J. Buchelt, and H. Leeb. *Physica B*, 276-278:588–589, 2000.

[32] P. Lukas, B. Alefeld, A. Ioffe, P. Mikula, and M. Vrana. *J. Phys. D: Appl. Phys.*, 28:A88–A91, 1995.

[33] H. Pleinert, E. Lehmann, and S. Körner. *Nucl. Instr. and Meth. A*, 399:382, 1997.

[34] A. G. Marshall and F. R. Verdun. *Fourier Transforms in NMR, Optical, and Mass Spectrometry.* ELSEVIER, 1989.

[35] M. Zawisky, U. Bonse, F. Dubus, Z. Hradil, and J. Rehacek. *Europhys. Lett.*, 68:337–343, 2004.

[36] M. Schlenker, W. Bauspiess, W. Graeff, U. Bonse, and H. Rauch. *J. Magn. Magn. Materials*, 15-18:1507, 1980.

[37] Del Mar Ventures, San Diego, CA 92130.

[38] D. L. Jacobson, M. Arif, L. Bergmann, and A. Ioffe. *Proc. SPIE*, 3767:328, 1999.

[39] K. Schoen, D. L. Jacobson, M. Arif, P. R. Huffman, T. C. Black, W. M. Snow, S. K. Lamoreaux, H. Kaiser, and S. A. Werner. *Phys. Rev. C*, 67:044005, 2003.

[40] H. Rauch. Towards interferometric Fourier spectroscopy. *Physica B Condensed Matter*, 213:830–832, February 1995.

[41] L. Mandel and E. Wolf. *Optical Coherence and Quantum Optics.* Cambridge University Press, 1995.

[42] H. Rauch, H. Wölwitsch, H. Kaiser, R. Clothier, and S. A. Werner. Measurement and characterization of the three-dimensional coherence function in neutron interferometry. *Phys. Rev. A*, 53(2):902–908, Feb 1996.

[43] Chapter 4, *Coherence properties* in [16].